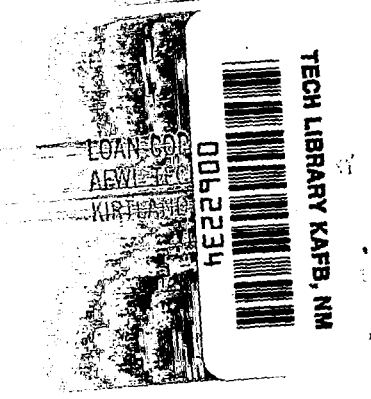

NASA Contractor Report 3503

The Investigation of a Variable Camber Blade Lift Control for Helicopter Rotor Systems

Alfred O. Awani

GRANT NCC-292
JANUARY 1982

NASA

NASA Contractor Report 3503

The Investigation of a Variable Camber Blade Lift Control for Helicopter Rotor Systems

Alfred O. Awani
University of Kansas Center for Research, Inc.
Lawrence, Kansas

Prepared for
Ames Research Center
under Grant NCC-292

National Aeronautics
and Space Administration

**Scientific and Technical
Information Branch**

1982

FOREWORD

The idea for this concept was initiated by Mr. Robert H. Stroub of NASA-Ames Research Center. The research and development work upon which it is based was made possible by a National Aeronautics and Space Administration research Grant NCC-292 to the University of Kansas Center for Research, Incorporated.

The author would like to acknowledge the following persons for their help and cooperation during the preparation of this report: Mr. Henry (Tex) Jones of AVRADCOM Research and Technology Laboratories for his valuable help in making the prescribed wake hover computer program operational; Dr. I. Chopra of Stanford University for his useful discussions; and to the following persons of NASA-Ames Research Center: Mr. Raymond Hicks for providing the airfoil analysis program H.; Dr. Lawrence Olson for providing the Ames multi-element airfoil computer code; Dr. Wayne Johnson for his technical knowledge and valuable suggestions; Sandra G. Williams for typing and organizing the text; and especially to Mr. Robert H. Stroub for his overall advice and guidance. The author would also like to express his gratitude to Mr. David Hickey, Mr. James Biggers, Mr. Jerry Kirk, Dr. Gary Chapman and the other personnel of NASA-Ames Research Center for their unfailing cooperation.

TABLE OF CONTENTS

PAGE

LIST OF SYMBOLS

Symbol	Definition	Usual Dimension
AR	Aspect ratio	
b	Number of blades	
b_b	Span of balance	ft
b_f	Span of flap	ft
B_{1_s}	Longitudinal Cyclic Coefficient	
c	Airfoil section chord	ft
C	Blade chord	ft
$\bar{c}$	Root-mean square chord of wing over span of flap	ft
c_b	Balance section chord; distance from flap hinge line to leading-edge of exposed-overhang balance or to a point midway between the points of attachment of the flexible seal of a sealed internal balance	ft
$\bar{c}_b$	Root-mean square balance chord over the span	ft
c_{b_1}	Contour balance section chord for plain-overhang balance; distance from hinge to point of tangency of balance leading-edge arc and airfoil contour (see fig. 5.2)	ft
$\bar{c}_{b_1}$	Root-mean square contour balance chord over the span	ft

Symbol	Definition	Usual Dimension
c_{b_p}	Balance-plate chord for internally balance flaps, distance from flap hinge line to leading edge of balance plate	ft ft
c_d	Drag coefficient	
c_f	Flap chord	ft
$\overline{c}_f$	Root-mean-square flap chord over the span	ft
C_h	Hinge Moment Coefficient = $\frac{\text{Hinge Moment}}{qC_f^2}$	
$C_{h_\alpha} = \frac{\partial C_h}{\partial \alpha}$	Variation of hinge moment coefficient with angle of attack	deg^{-1} rad^{-1}
$C_{h_\delta} = \frac{\partial C_h}{\partial \delta}$	Variation of hinge moment coefficient with control surface deflection	deg^{-1} rad^{-1}
C_{h_t}	Tab hinge moment coefficient	
C_l	Section lift coeffecient	
C_L	Lift coefficient of rotor	
C_{l_b}	Basic lift due to camber	
$C_{l_\alpha} = \frac{\partial C_l}{\partial \alpha}$	Variation of section lift coefficient with angle of attack	deg^{-1} rad^{-1}
$C_{l_\delta} = \frac{\partial C_l}{\partial \delta}$	Variation of sectional lift coefficient with control surface deflection	deg^{-1} rad^{-1}

Symbol	Definition	Usual Dimension
$C_{l_{max}}$	Maximum lift coefficient	
C_{l_1}	Additional lift coefficient at a section caused by an angle of attack change over rotor blade (wing)	
$C_{l_{1_\alpha}}$	Average value of the lift-curve slope over the span of the control surface	
$\frac{C_{L_R}}{\sigma}$	Rotor lift coefficient in wind-axes system, $\frac{\text{Lift}}{\rho S(\Omega R)^2}$	
C_m	Pitching Moment coefficient, $\frac{M}{qSc}$	
C_p	Pressure coefficient, $\frac{P-P_o}{q}$	
$\frac{C_p}{\sigma}$	Rotor power coefficient, $\frac{(\text{torque})(\Omega)}{\rho S(\Omega)R)^3}$	
$\frac{C_{x_R}}{\sigma}$	Rotor propulsive-force coefficient in wind-axes system, $-\frac{\text{drag}}{\rho S(\Omega R)^2}$	
C_t	Tab chord	ft
$\frac{C_T}{\sigma}$	Rotor thrust coefficient (shaft-axes lift coefficient)	
c_w	Airfoil section with tab coefficient	
d	Distance from hinge-axis to midpoint of upper-surface width	ft
D	Drag	lbs
E_e	Effective edge velocity correcton factor	

Symbol	Definition	Dimension
$(1-E)_c$	contour of the flap when undeflected meets the upper and lower surfaces of the airfoil at x = (E ÷ E')	
$E_c = f$	Flap chord	ft
F_1, F_2, F'_2		
F_3, F_4, F_5, F_6	Correlation factors	
g	Gap between leading-edge of undeflected balance plate and forward wall of balance chamber of internally balance flap expressed as a fraction of the balance-plate chord c_{b_p}	
HP	Horsepower	
K_1	Ratio between angular deflection of control and flap deflection with spring tab fixed	
L	Lift	lbs
L_1	Vertical line clearance required for seal to develop moment for the flap arrangement	
M	Mach number; also with subscripts, 0,A,B of figure 5.2, area moment of exposed-overhang-balance profile about hinge axis	
M_B	Moment of the balance	lb-ft
M_{CRIT}	Critical Mach number	

Symbol	Definition	Usual Dimension
M_{DD_O}	Zero-lift drag divergence Mach number	
$M_{(1)(270)}$	Rotor blade tip Mach number at 270° azimuth position	
m_s	Seal moment ratio for internally balanced flap; ratio of balancing moment of flexible seal to balancing moment of thin-plate overhang	
M_s	Seal-Moment or incremental hinge moment resulting from seal of unit span	
n	Distance measured normal to streamline	ft
P	Static pressure at a point on the airfoil	lb/sq. ft
P_o	Static pressure in the free air stream	lb/sq. ft
P_R	Resultant pressure coefficient	lb/sq. ft
q	Dynamic pressure of the free air stream	lb/sq. ft
Q	Rotor torque	ft-lbs
RN	Reynolds number; also with subscripts, 0,A,B of figure 5.2, nose radius of exposed-overhang balance	
R	Rotor radius	ft

Symbol	Definition	Usual Dimension
$r/R = x$	Blade radial station, ie ratio of blade element radius to rotor blade radius	
s	Width of flexible seal of internally balanced flap expressed as a fraction of the balance plate chord c_{b_p} ; and also similar symbol is used to measure distance along a streamline	
S	Reference areas [(number of blade) x (blade chord) x (rotor radius)]	
t	Airfoil section thickness at flap hinge line	ft
$T = \Delta pr$	Tensile force per unit span	lb/ft
$\overline{t}$	Root-mean square of airfoil section thickness at flap hinge line over span of tab	ft
V	Free stream velocity	ft/sec or knots
X	Chordwise coordinate	ft
(x,y)	Physical plane of zero incidence, with an Argand plane	
Y_1	Distance from plane of symmetry to inboard end of tab	ft
Y_2	Distance from plane of symmetry to outboard end of tab	ft
Z_∞	Physical plane for an absolute incidence of α	

Subscripts	Definition	Usual Dimension
α, δf	As suffixes to denote values at absolute incidence of α and flap deflection δf	
∞	As suffice to denote values at an infinite distance from the airfoil	
*	Meaning airfoil surface	
Greek Symbol		
α	Angle of attack	deg or rad
α'	Incidence of the front part of the airfoil measured from the $\delta_f = 0$ chord line	deg or rad
α_c	Angle of attack of control axis (swash plate) relative to tunnel centerline, positive tilted aft	deg
α_i	Ideal angle of attack	deg or rad
α_{L_o}	Angle-Of-Zero lift	deg or rad
α_s	Angle of rotor shaft from vertical, positive shaft tilted aft; also used for stalling angle	deg or rad
$\alpha_\delta = \frac{\partial \alpha}{\partial \delta}$	Flap effectiveness parameter; effective change in section angle of attack per unit change in flap deflection or lift effectiveness of the control surface	
ϕ	Inflow angle of attack	deg

Greek Symbol	Definition	Usual Dimension
θ	Blade section pitch angle measured from the line of no lift of the airfoil section to the plane of the rotor disk	deg
θ_1	Twist	deg
θ_c	Cyclic pitch	deg
$\theta_{.75}$	Collective pitch at 0.75R	deg
(ϕ, ψ)	Plane of velocity equipotentials (ϕ = constant), and streamlines (ψ = Constant) for zero circulation (α = 0)	deg
δ	Control surface angle	deg
δ_f	Flap deflection, measured positively from a downward movement of the flap	deg
δ_{cr}	Critical flap deflection; that is deflection at which plain-overhang balance is no longer effective in reducing slope of hinge-moment curve	deg
δ_b	Deflection of balance plate of internally balanced flap	deg
ψ	Rotor blade azimuth angle measured from downwind position in direction of rotation	deg
ν	Induced inflow velocity at rotors also used for ratio of specific heats	ft/sec

Greek Symbol	Definition	Usual Dimension
λ_i	Mean induced velocity including ground effect and rotor/rotor interference	ft/sec
$\mu = \frac{V}{\Omega R}$	Advance ratio	
Ω	Rotor rotational speed	rad/sec
ΩR	Rotor tip speed	ft/sec
ρ, ρ_o	Local and Stagnation densities respectively	slug/cu. ft
$\sigma = \frac{S}{\pi R^2}$	Rotor Solidity	
Γ_{max}	Blade maximum bound circulation	ft^2/sec
Δ	Incremental change	
$\leq$	Less or equal to	

SUMMARY

A new rotor configuration called the variable camber rotor was investigated numerically for its potential to reduce helicopter control loads and improve hover performance. This rotor differs from a conventional rotor in that it incorporates a deflectable 50% chord trailing edge flap to control rotor lift, and a non feathering (fixed) forward portion. Lift control is achieved by linking the blade flap to a conventional swashplate mechanism, therefore, it is pilot action to the flap deflection that controls rotor lift and tip path plane tilt.

This report presents the aerodynamic characteristics of the flapped and unflapped airfoils, evaluations of aerodynamics techniques to minimize flap hinge moment, comparative hover rotor performance and the physical concepts of the blade motion and rotor control. All the results presented herein are based on numerical analyses.

The assessment of payoff for the total configuration in comparison with conventional blade, having the same physical characteristics as an H-34 Helicopter rotor blade was examined for hover only. The variable camber rotor configuration is shown to reduce hover power required by at least 2.6% for a flap deflection of 2 degrees. This power improvement was attributed to a change in the spanwise lift distribution decreasing both profile and induced power of the rotor.

CHAPTER 1

INTRODUCTION AND BACKGROUND

Over the years, the design of helicopters has undergone cycles of refinement taking advantage of developments in advanced technology (reference 1). Increased demand in payload, hover performance and speed have forced the researcher to examine over and over the limits of rotor design and operation. One of the elements establishing these limits is the sectional performance of the airfoil employed.

Because of the progress in theoretical airfoil analysis, it has become possible to estimate two-dimensional characteristics which, until recently, could be quantified only experimentally. The new methods have permitted the definition of advanced airfoils which, compared to airfoils in use today, display improved drag divergence and maximum lift characteristics while retaining low pitching moment levels and acceptable profile drag.

The key sectional characteristics of the airfoils employed on a rotor can be separated into three flow regions:

- Supercritical flow at low lift, typical of the advancing blade tip in forward flight.
- Lift levels of $C_L = 0.6$ at Mach number near $M = 0.6$, representative of hover requirements.
- High lift at Mach number in the range of $0.3 < M < 0.5$ over the retreating blade. Most helicopters airfoil design objectives fall

within one of these three regions, illustrated in Figure 1.1 (see Reference 2).

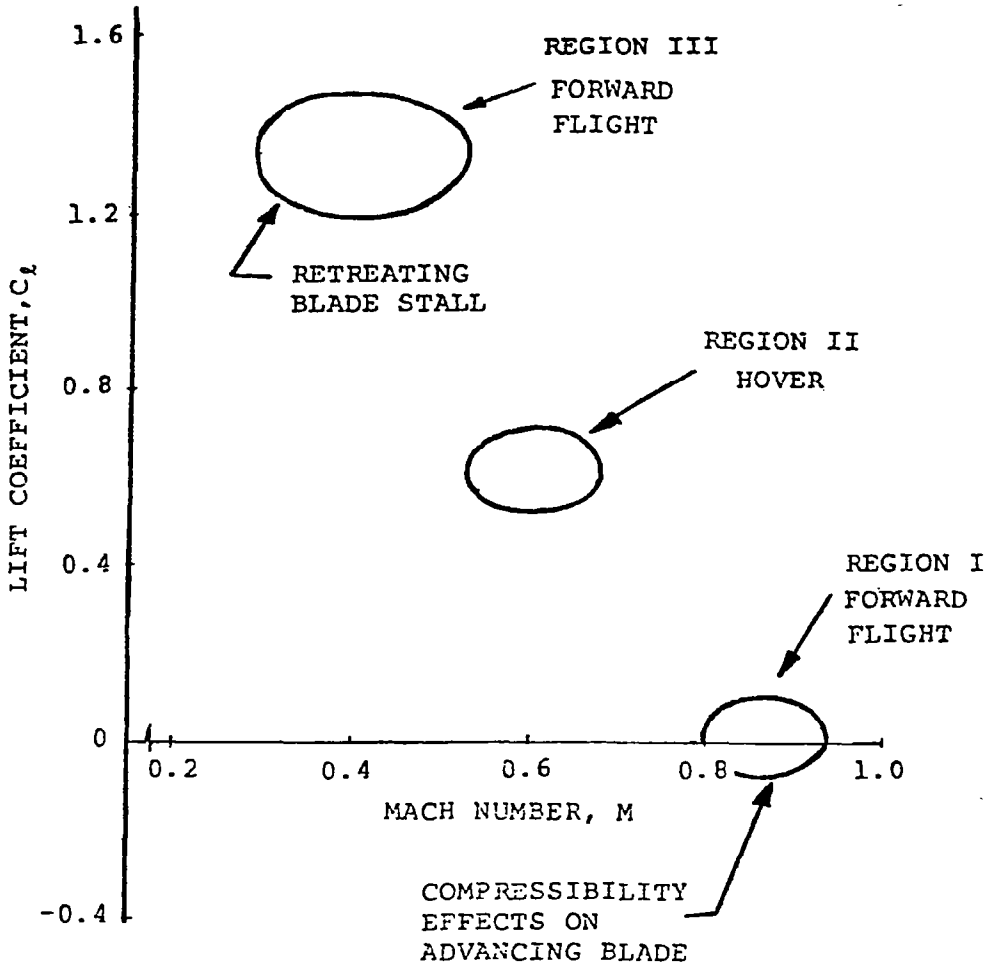

(SOURCE: REFERENCE 2)

Figure 1.1. LIFT COEFFICIENT AND MACH NUMBER COMBINATIONS (ROTOR ENVIRONMENT)

It is difficult to quantify the local flow along a rotor blade so that airfoil design objectives can be set. This difficulty arises from any or all of the following effects:

- Tip relief
- Blade elastic characteristics
- Unsteady aerodynamics
- Tip sweep
- Tip planform variation
- Reynolds number

Consequently, the design of a rotor with fixed geometry inevitably involves compromises in the choice of the blade airfoil section. A rotor utilizing variable geometry has the potential of eliminating or alleviating some of these compromises.

This project then explores an innovative idea of improvement of helicopters. This concept uses variable camber for blade lift control to reduce control loads and improve performance, while keeping the rotor control system as simple as possible. The variable camber rotor has the advantage of providing more mean-line curvature where high lift is required and reduced curvature at low lift and transonic conditions as required near the advancing blade tip, thus changing the design restrictions of fixed-contour rotor blades.

The advanced rotor development carried out during the late 1960's and early 1970's showed that helicopter rotors in high speed flight can become limited by advancing blade loads as well as retreating blade stall.

New guidelines were then set to control the margin between the drag rise and the growth in pitching moments at high subsonic Mach numbers. Figure 1.2 shows the regions in the rotor disc where phenomena take place which limit the rotor operation because of the rapid growth in drag (power required), the growth in sectional pitching moments (advancing blade loads or "Mach tuck"), and possibly local loss of lift, also associated with power and load penalties.

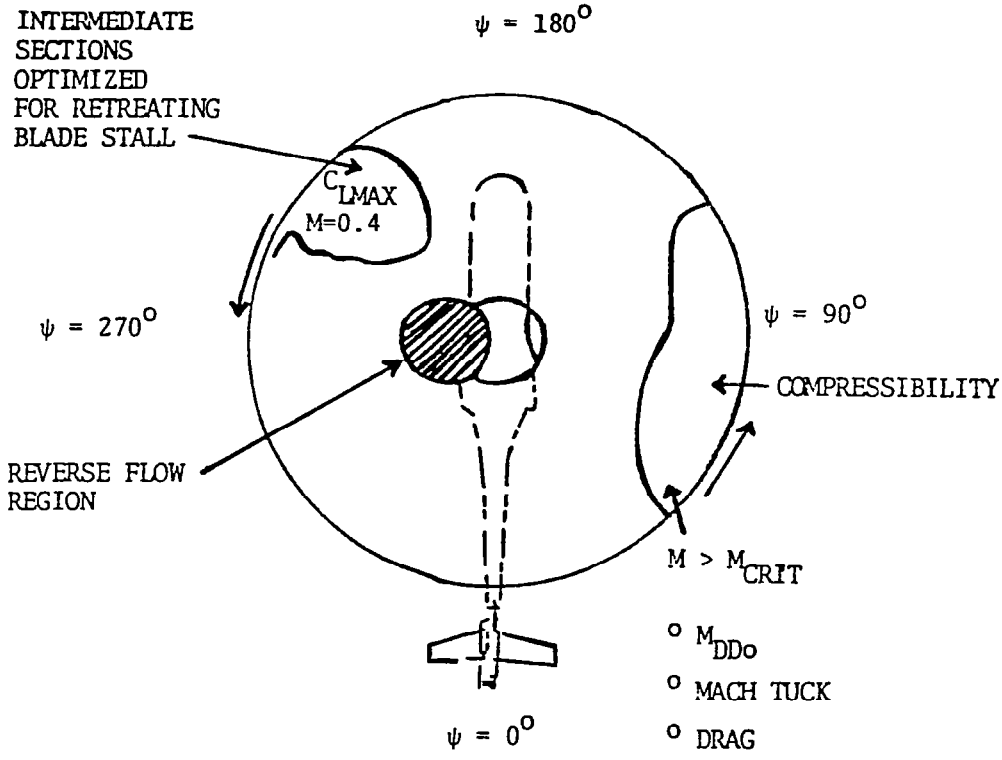

Figure 1.2. ROTOR ENVIRONMENT - FORWARD FLIGHT

After a preliminary investigation, the variable camber concept was selected, because it would yield airfoils which exceed the present boundary. In addition, an investigation of variable camber by use of the Boeing Vertol VR-7 airfoil modified with a 50 percent chord trailing-edge flap deflected 0 to 20 degrees illustrates the potential benefits of improved airfoil designs in terms of a potential improvement over the undeflected Vertol VR-7 airfoil or the best current advanced airfoils. (Figure 3, Ref. 3) illustrates the present state of helicopter airfoil optimization based on advanced/retreating blade characteristics.

CHAPTER 2

DESCRIPTION OF THE VARIABLE CAMBER ROTOR SYSTEM

2.1 General - The variable camber rotor model is a four-bladed fully articulated system, with the same physical characteristics as an H-34 helicopter blade (see ref. 4). Variable camber is provided in the form of deflectable trailing edge flaps on the blade. The rotor blades flap about a hinge that is offset from the shaft axis.

2.2 Blades - The airfoil section are VR-7 from root cutout to 0.9R and VR-8 from 0.9R to tip. An internally sealed flap in the inboard trailing edge area has an envelope of 0.5c and 0.9R. The overall changes imply that the trailing portion of the blade will be deflected about a hinge from some neutral position.

The sketches in figures 2.1 and 2.2 shows the variable camber rotor with the flap neutral and with the flap deflected 20 degrees respectively, and also delineates other features of the concept that are vital to achieving the design objectives. The primary features and their functions are as follows:

- The primary load carrying structure is the forward section of the blade and is not connected to the control system.
- The aft section or flap is attached to the forward section by a pin joint arrangement. It is also connected to the rotor control system for the control of rotor thrust level and vectoring. This section is configured by aerodynamic and mechanical

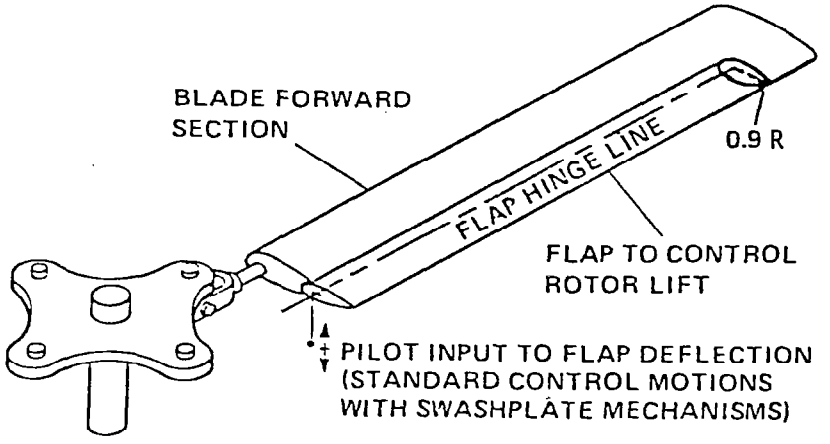

Figure 2.1. - Variable Camber rotor blade with flap neutral.

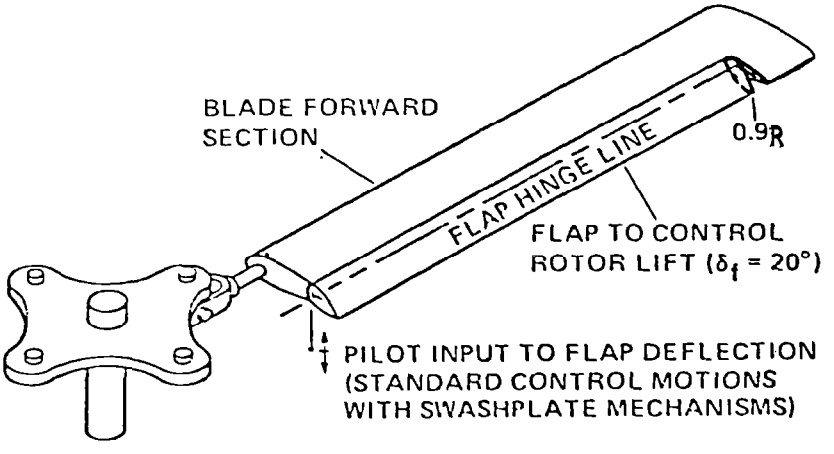

Figure 2.2 - Variable Camber rotor blade with a 0.5c Trailing edge flap deflected 20°.

techniques to achieve low flap hinge moments.

- The forward section has structural properties that are stiffer than the aft section in all directions.
- The rotor considered has conventional flap and lag hinges.
- The rotor hub is a conventional articulated hub.
- Control by cyclic pitch change will be accomplished by a linkage from the blade flaps to a "swash plate", which is a rotating plane that defines the pitch of the blades.

2.3 Articulated Rotor System - The blades are attached to the hub by hinges, free to flap up and down and swing back and forth. The main characteristics of this system are: 1) Blade root moments are small; 2) The articulated hinges can be offset from the center of rotation to produce high control moments, thus permitting large allowable travel of c.g.; 3) Lead-lag dampers are usually required (see ref. 5).

2.4 Design Criteria - The geometry of the hypothetical conventional rotor is given in table 2.1.

Table 2.1. Rotor Blade Geometry

GEOMETRICAL DEFINITION	DIMENSION
Rotor radius, R	28 FT
Blade chord, c	1.367 FT
Cutout radius	4.48 FT
Rotor Solidity, $bc/\pi R$	0.0622
Blade moment of inertia about flapping hinge	1264 FT-IB-SEC^2
Flapping hinge offset	1.0 FT
Number of blades	4
Blade taper ratio	1.0
Normal tip speed	700 FPS

CHAPTER 3

AERODYNAMIC SECTION ANALYSIS

This chapter detail the process by which one particular flapped rotor configuration was chosen and evaluated as to its potential for providing a relatively high final maximum lift coefficient (in the 1.67-1.9 range) with a small flap deflection (no more than 15-20 degrees); small deflections are desirable, since they minimize the drag increment involved. Although not presently a key design criterion, some consideration was given to the increase in pitching moment due to flap deflection.

The lift and drag characteristics of the chosen section were obtained by inserting the airfoil's geometrical coordinates into an airfoil analysis computer program.

As is implied above, this analysis covers only a single configuration which was chosen with only very rough optimization criteria. The two-dimensional airfoil analysis methods used herein permitted the prediction of the effects of flap configurations on airfoil characteristics. Though large amounts of empirical data are available on lift characteristics of many specific flap arrangements, and some reasonably reliable, somewhat generalized semi-empirical methods are available for analyzing limited classes of flap types and deflections (see Refs. 6 and 7), more reliable methods are avaiable in (Refs. 8 and 9) of a sufficient flexible and general nature to permit a broad and comprehensive optimization with regard to the two-dimensional characteristics of flapped airfoils.

3.1 Section Selection - The Vertol VR-7 airfoil was selected because it afforded a higher $C_{L\ max}$ and low speed capability than another section commonly used in rotors, the NACA 0012 (see Ref. 3, figure 3).

The maximum lift coefficient for the unflapped VR-7 airfoil (for the viscous/potential flow interaction, Reynolds number of 1.592×10^6) is 1.22. This figure had to be increased by 0.68 to put in it the desired maximum lift coefficient range. Simultaneously, parasite drag increments had to be minimized; there was no clear ceiling value for ΔC_{do}, but it was clear that the increments caused by such typical configurations as 25% chord plain flaps deflected 30-60 degrees would be unacceptably large (ΔC_d approximately .08-.20, representing easily an order of magnitude drag increase) (see Ref. 6, Fig. 6.1.7-22). It appeared that only by using large-chord flaps with small deflections would one escape large drag penalties.

Based on preliminary investigation through literature search etc., a configuration was adopted which included a plain flap with .50 chord ratio. The 0.50 chord ratio was selected because it appeared to represent a reasonable compromise between flap effectiveness and the tendency to increase drag (that is $dC_l/d\alpha$ and $dC_d/d\alpha$) (see Refs. 10, 11 and Appendix G, Ref. 7). Also, within the analysis performed here, it is assumed that the flap is of the sealed-gap type and, furthermore, that the blade surface remains continous and unbroken even with the flap deflected (see Figure 3.1), and (also ref. 8).

The two-dimensional lift, drag and pitching moment characteristics of the section were found by using the Ames Multielement airfoil analysis

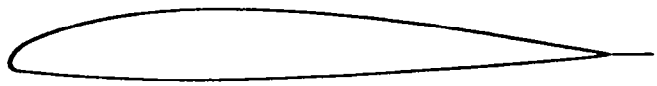

(a) FLAP NEUTRAL

(b) FLAP DEFLECTED 20°

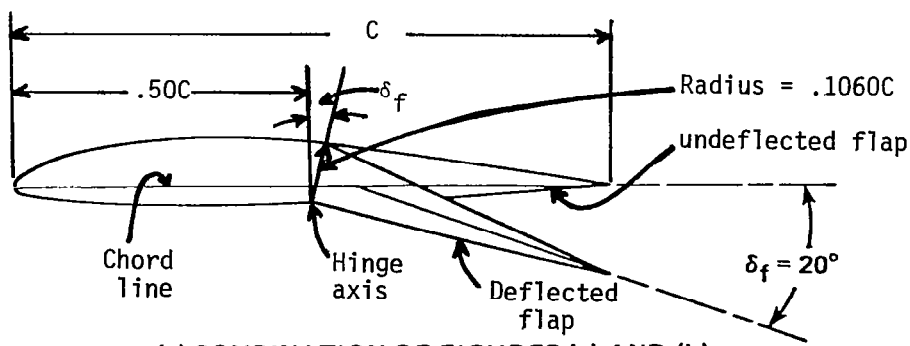

(c) COMBINATION OF FIGURES (a) AND (b)

Figure 3.1. - Boeing Vertol VR-7 with Flap neutral and with .50C flap deflected 20°.

computer code (Ref. 12) and (Ref 13), which required as inputs, the airfoil geometrical coordinates (percent of chord deviation vertically from the airfoil chord line as a function of percent of chord length, Mach number, Reynolds number, free stream velocity and angle-of_attack. The coordinates of the flapped airfoil were determined by graphical superimposition of the aft-chord of the Boeing Vertol VR-7 airfoil deflected 2 to 20 degrees on the undeflected forward half-chord (see Fig. 3.1). The effective point of rotation in this graphical process was taken to be at the 50-percent chord point on the airfoil's lower surface. Some interpolation and smoothing were applied to both the upper and lower surface coordinates to preserve a continous surface. The overall changes imply that the trailing portion of the blade will be deflected about a hinge from some neutral position.

Mach number and Reynolds number ranges were established based on the rotor environment in forward flight (see Ref. 3, figures 2 and 3), free stream velocity and assuming the rotor to be a four-bladed, fully articulated rotor system (see Ref. 4), with some gross physical dimensions as an H-34 standard blade (radius of 28.0 ft, constant blade chord of 1.367 ft, tip speed of 700 fps). With these specification and assuming sea-level day ambient conditions, tip Mach number was approximately 0.6, while tip Reynolds number was about 2.4×10^6; these quantities were decreased proportional to radius for stations farther inboard.

Lift coefficient versus angle-of-attack values were generated up to stall for flap deflections from 0 to 20 degrees. Simultaneously, the drag and pitching moment coefficients corresponding to these values were generated herein. Plots of the results are shown in figure 3.2, along with the curve for the unflapped VR-7 section generated by the same computer program.

Based on these results, it was shown that the changes obtained were associated with large increase in maximum lift, substantial shifts in the angle of zero lift (more negative without changing the lift-curve slope) and large pitching moment changes (more negative). This is due in part to the fact that for a cambered airfoil, the flow comes smoothly onto the nose at some angle which in general is different from zero. This angle is called ideal angle of attack, α_i (see Refs. 14 and 15). At angle different from α_i, the strength of the singularity increases with $(\alpha - \alpha_i)^2$, that is, the pressure distribution at the nose may be correlated with $\alpha - \alpha_i$. This, of course, is correlated with the stagnation point location; at $\alpha - \alpha_i$ the stagnation point is at the nose.

It has been known that for a straight airfoil, the lift coefficient $C_l = 0$ at $\alpha = 0$; but for cambered airfoils there is a basic lift, $C_l = C_{l_b}$ at $\alpha = \alpha_i$. It is called the basic lift because it is independent of the nose singularity, depend only on the camber. At angles different from α_i there is an additional lift, which is equal to $2\pi(\alpha - \alpha_i)$, and is

thus related to the singularity. These concepts are outlined by Allen in Ref 15, where the expressions are given as follows:

$$C_l = C_{lb} + 2\pi(\alpha - \alpha_i) \tag{3-1}$$

$$C_{lb} = 2 \int_0^{\pi} \frac{dyc}{dx} \cos\theta d\theta \tag{3-2}$$

$$\alpha_i = \frac{1}{\pi} \int_0^{\pi} \frac{dyc}{dx} d\theta \tag{3-3}$$

where

$$x = 1/2\ (1 - \cos\theta)$$

The angle θ is related to the chordwise coordinate x by the last equation, and is illustrated in the sketch below. dy_c/dx is the slope of the camberline. If $y_c(x)$ is given analytically, it can be transform to $y_c(\theta)$ and the above expressions integrated for C_{lb} and α_i.

Source: Ref. 16

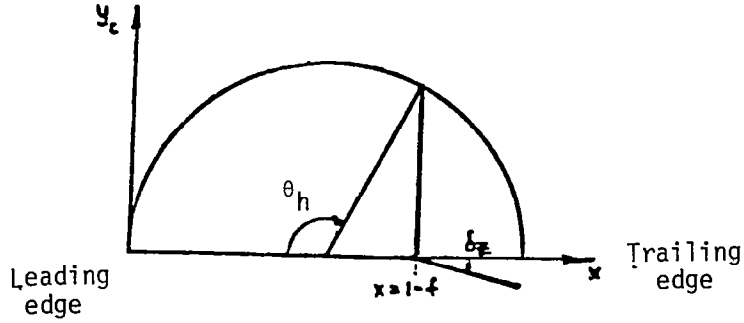

where f, is referred to as the flap chord, and could be expressed as:

$$f = 1/2\ (1 + \text{Cos}\ \theta_h)$$

Though the lift, drag and pitching moments coefficients values generated herein by the airfoil analysis computer codes are considered reasonable, the magnitude of the increment of the profile drag coefficients was compared by plotting the lift coefficient versus drag coefficient (see Figure 3.4). Figure 3.4 shows that there is only a minimal difference between the profile drag coefficient for the flapped airfoil deflected 2 degrees and the unflapped airfoil. Also by comparing with data from a 65-210 airfoil for a 0.50c flap deflected 0 to 10 degrees given in Ref. 11, there, the difference in drag coefficient between the unflapped airfoil and the airfoil with the flap deflected 10 degrees is .002. However, in the present analysis, it was assumed that there was no unanticipated roughness and that there was perfect continuity in the airfoil surface near the flap hinge, which would ensure that performance estimates were conservative, at least with regard to what is presently known about the drag of flapped airfoils.

3.2 Pressure Distribution - The results of the pressure distribution for the VR-7 airfoil with a 50 percent chord trailing edge flap are shown in the form of resultant-pressure increment diagrams (see Fig. 3.2); which represent changes in resultant pressure distribution caused by a change in angle of anyone part or a combination of the component parts of the airfoil with regard to the flap.

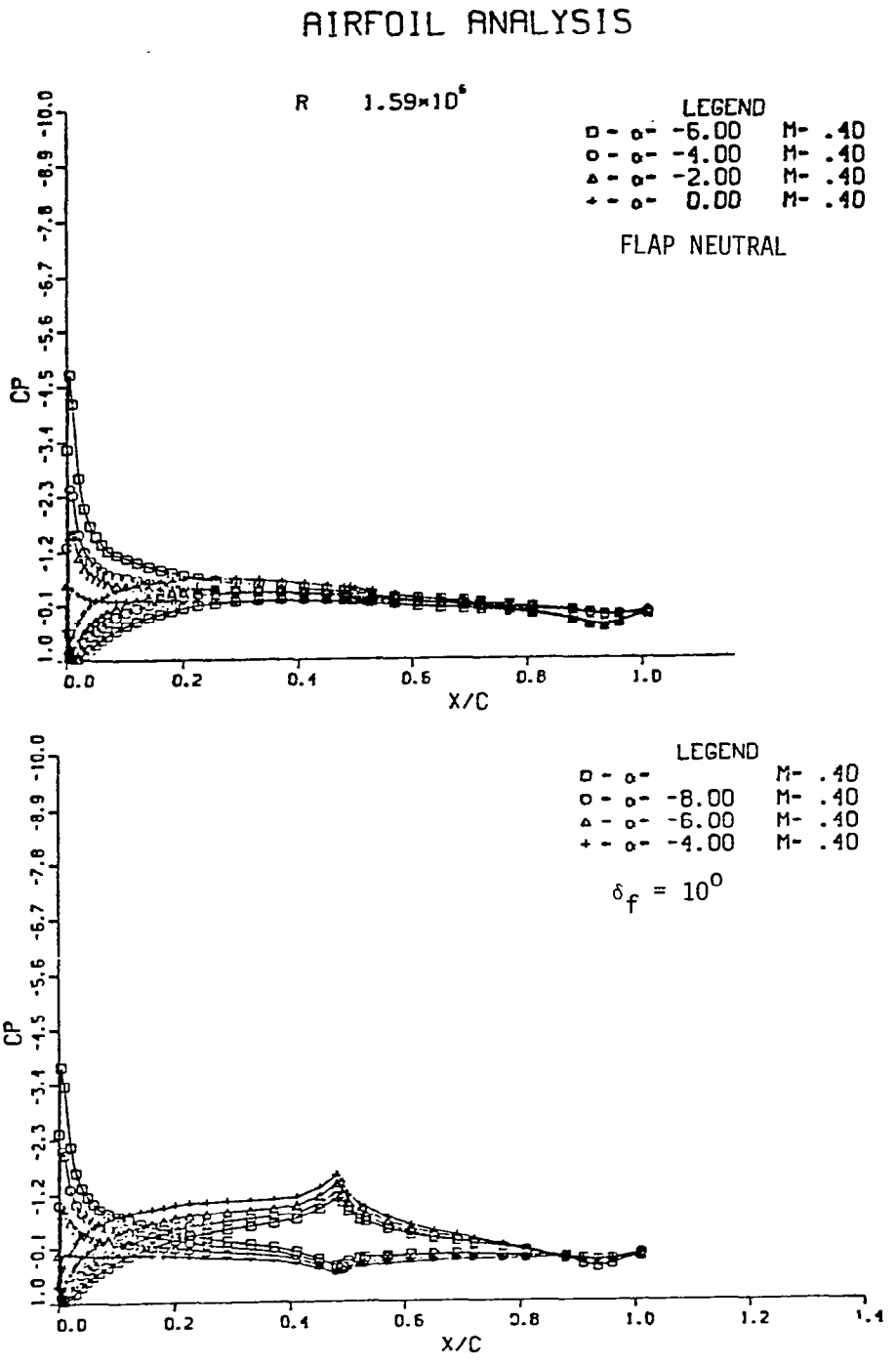

Figure 3.2. Numerical analysis of the resultant pressure distribution over the VR-7 airfoil at various angles of attack. Flap neutral and flap deflected 10 degrees.

The analysis were computed at angles of attack range (-16 to + 12 degrees) at interval of 2 degrees. The flapped configurations were set at angles of 0 to 20 degrees. Values were generated throughout the entire angle-of-attack range for each flap deflection. All diagrams of the resultant pressure or resultant pressure increment of the airfoil due to flap were computed and plotted as pressure coefficient (C_p) which can be represented by the following equation:

$$C_p = P_R = \frac{P-P_o}{q} \qquad (3\text{-}4)$$

where P, is the static pressure at a point on the airfoil; P_o is the static pressure in the free air stream; and q, is the dynamic pressure of the free air stream.

The pressure distributions for the various flap deflections showed peaks on the upper and lower surface near the 50 percent chordwise position where the direction of the surface changes rapidly. This imply that the deflection of the flap causes an increment of pressure over the entire airfoil, this increment reaching peak values at both the nose and at the hinge axis (see Refs. 11 and 16).

3.3 Trailing-edge Flap Characteristics - The downward deflection of the modified VR-7 airfoil with the 50 percent chord trailing edge flap effectively makes the ordinates of the mean camber line more positive in this region. As a consequence, the angle-of-zero lift (α_{Lo}) become more negative and the lift at a given geometrical angle is increased. Thus the term ($\cos\theta$-1), expressed in (Ref. 17, chapter 5, equation 34)

in equation:

$\alpha_{L_0} = \frac{1}{\pi} \int_0^{\pi} \frac{dz}{dx} (\cos\theta - 1) d\theta$ vanishes at the leading edge where $\theta = 0$;

and its absolute values reaches maximum at the trailing edge where $\theta = \pi$ (see Ref. 17).

The lift curve is displaced to the left as a result of an increase in α_{L_0} negatively (see Figure 3.3). The gain in lift at the given geometric angle of attack is shown as ΔC_l. By reference to Fig. 3.3, $\Delta\alpha_{L_0}$ is given by the formula (see Ref. 17):

$$\Delta\alpha_{L_0} = (\Delta C_l / 2\pi) = [(\pi - \theta_h) + 2 \sin \theta_h] \ \delta_f / \pi \qquad (3\text{-}5)$$

where θ_h is related to the hinge location by the expression $X_h = f = 1/2 (1 + \cos\theta_h)$. Equation (3-5) show that the incremental values of lift coefficient (C_l) about the aerodynamic center and α_{L_0} vary linearly with the flap deflection. Thus the portion of the mean camber line in the vicinity of the trailing edge powerfully influences the value of α_{L_0}.

Though the stalling angle (α_s) is reduced by the deflection of a flap, the reduction is not great enough to remove the gain arising from the increase in $C_{L_{max}}$ and the shift of the curve as a whole (see Figure 3.3).

This analysis further indicate, that with the flap neutral, the curve is linear to within 1 or 2 degrees of the airfoil stall, whereas with the flap deflected 10 to 20 degrees, the curve is linear for a range of angle of attack, and then assumes a break as the flap stalls. Beyond

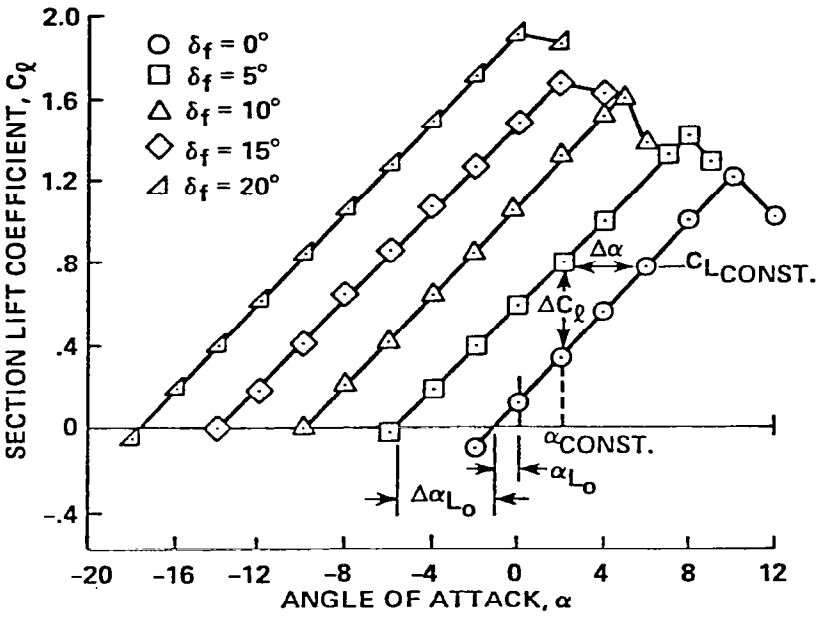

M = 0.4

RN = 1.6×10^6.

Figure 3.3 - Numerical analysis of the effect of flap deflection on lift curve.

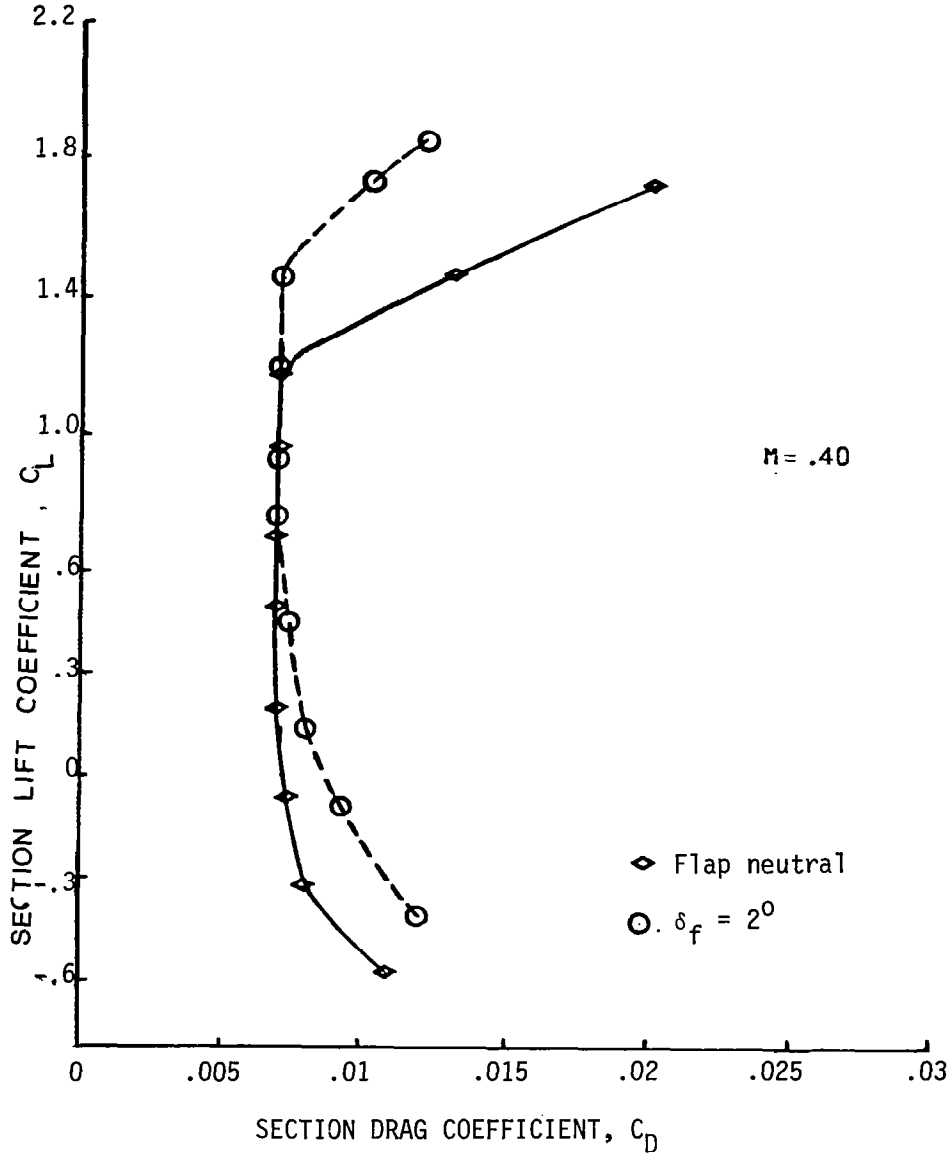

Figure 3.4 - Numerical analysis of the drag curves for the VR-7 airfoil section at flap neutral and 2 degrees flap deflection.
RN = 1.6×10^6.

the flap stall, the curve become more gradual, indicating that separation is continuing to build up over the airfoil proper as the lift increases until the airfoil stalls.

Also, it is known that for a thin airfoil, stalling occurs at the nose, and is determined principally by the history of the development of the boundary layer from the stagnation point on the lower surface, around the nose, into the adverse gradient downstream of the suction peak, on the upper surface (see Ref. 16). The important developments occur within the first few percent of the airfoil chord. This suggests the idea that a family of airfoils having the same nose but different after-bodies (camber, thickness distribution, etc.) should exhibit a correlation at stalling, namely, that at stall the conditions at the nose are identical for all the airfoils. This implies that the stagnation point location is at the same location in all cases and that the pressure distribution around the nose is a function only of stagnation point location. The latter point has, infact, been demonstrated by Rettie (Ref. 18). While in the case of the trailing edge, the stall starts at the trailing edge and depends on the whole boundary layer development history up to there. Also, the airfoil continues to develop lift after separation has occured; and the progress of development after separation is different for different airfoils (see Ref. 16).

3.4 Flap Deflection Range - The projected flap deflection range were based on the maximum allowable flap deflections for the linear limit of the airfoil characteristics up to stall conditions at several angle-of-attack ranges.

The allowable range of flap deflection (δ_f) required for this configuration is 0 to +20 degrees.

3.5 Trailing-edge Plain Flaps - The term "plain flaps" as used herein includes any conventional flap type airfoil, regardless of contours, that has not been modified with any form of internal balance, overhang balance or tab balance, etc to reduce the hinge moment (see chapter 4). Plain trailing edge flaps are formed by hinging the rearmost part of the wing section about a point within the contour (see ref. 19).

Figure 3.1.A shows the general planform of the VR-7 with flap neutral (i.e. $\delta_f = 0°$), while Figure 3.1.B shows the modified VR-7 airfoil with a 50 percent chord trailing edge plain flap deflected 20 degrees.

Thus, the plain trailing edge flap can then be considered as a starting point for all forms of controls. The effectiveness of the flap derives from the fact that on rotation it changes the camber of the section and so permits of a change of circulation and therefore, of lift at a given incidence.

Then, when applied to rotor analysis, the change in chordwise loading produced by a positive setting of the flap in this investigation will have a maximum near the rotor leading edge and a secondary peak at the flap hinge, falling to zero at the flap trailing edge (see Figure 3.2).

CHAPTER 4

HINGE MOMENT PREDICTION TECHNIQUES

This chapter discusses the characteristics of existing flap control devices, analyzes the effects of the existing devices to the variable camber flap configuration, propose new devices that show promise of lowering the hinge moment characteristics of those now in use.

Descriptions of the criteria for hinge-moment characteristics along with various types of aerodynamic balances are presented together with assumptions made in the derivations and the limitations of the method as applicable to the present configuration. Also, assessment is made as to the feasibility for getting low hinge-moments of control surfaces.

Due to lack of test data for the present analysis, only quantitative or rough qualitative evaluations of any of the effects were made. The methods presented herein, therefore, are considered to be reasonable; but not sufficiently reliable to enable a designer to arrive at a satisfactory final flap configuration without some development work on a full/large-scale wind-tunnel model or in flight. The methods are useful, however, for making preliminary design or for deciding the manner in which existing flaps should be modified in order to obtain desired changes in characteristics.

4.1 Hinge Moment Characteristics - The hinge moment characteristics of flaps have been found to be critically dependent on the flap contour near the trailing edge. In general, any increase in trailing-edge angle whether obtained by changing the basic airfoil section or by modifying the

contour of a given airfoil section, may be expected to reduce the degree of unbalance of the plain flap. The greatest balancing effect of a large trailing-edge angles occurs at small angles of attack and at small flap deflections; therefore the hinge-moment curves of flaps having large trailing angles usually are characterized by a high degree of linearity.

The explanation for the balancing effect resulting from the change of a large trailing-edge angle can be made on the basis of an effective change in airfoil camber. As an approximation, the effective contour of an airfoil in a viscous fluid of the contour is obtained by adding the boundary-layer displacement thickness on each airfoil surface to the geometrical coordinates of that surface. With positive angle of attack or flap deflection, the boundary-layer displacement thickness increases on the upper surface of the airfoil (where the pressure gradient become more adverse) and the boundary-layer-displacement thickness decreases on the lower surface of the airfoil (where the pressure gradient becomes less adverse). This change in boundary-layer-displacement thickness causes an unswept effective camber change which in turn, cause reductions in the effective flap deflection and therefore, a lower hinge moment. The changes in effective camber near the trailing edge are much more influential on hinge-moments than on lift, because the small ΔL at the trailing edge act on a long momentum. The magnitudes of the camber changes seems to depend to a large extent on the magnitude of the trailing-edge angle, the greater changes occuring for the larger trailing-edge angles. An open gap at the nose of the flap allows the boundary-layer

air to flow from the high-pressure airfoil surface to the low-pressure airfoil surface. The effective change in camber and consequently the effect of the boundary layer on the hinge-moments, particularly for flaps having larger trailing-edge angles, therefore are greater when the gap is open than when the gap is closed.

4.2 Plain Flap Hinge Moment Coefficient - The expression for calculating the hinge-moment coefficient (C_h) in subsonic two-dimensional compressible flow has already been deduced in Appendix A (also see Ref. 20) as:

$$C_h = b_0 - \frac{b_1 a_0}{a_1} + \frac{b_1}{a_1} C_L - \left(\frac{b_1 a_2 - a_2 b_2}{a_1} \right) \delta_f \qquad (4\text{-}1)$$

where the quanties a_0, a_1, a_2, b_1, b_2, and b are defined as follows:

$$a_0 = (C_L)_{\alpha' = \delta_f = 0}, \quad a_1 = \left(\frac{\partial C_L}{\partial \alpha} \right)_{\alpha' = \delta_f = 0},$$

$$a_2 = \left(\frac{\partial C_L}{\partial \delta_f} \right)_{\alpha' = \delta_f = 0}, \quad b_1 = \left(\frac{\partial C_h}{\partial \alpha} \right)_{\alpha' = \delta_f = 0}$$

$$b_2 = \left(\frac{\partial C_h}{\partial \delta_f} \right)_{\alpha' = \delta_f = 0} \quad \text{and} \quad b = \frac{b_1 \cdot a_2 - a_2 b_2}{a_1} = -\left(\frac{\partial C_h}{\partial \delta_f} \right)_{C_L = \delta_f = 0}$$

while C_L is the lift coefficient, δ_f, is the flap deflection, measured positively for a downward movement of the flap and α', is the incidence of the front part of the airfoil measured from the $\delta_f = 0$ chord line.

4.3 Beveled Trailing Edge Balance - It was shown in Ref. 21 that when a beveled trailing edge is added to a flap profile, the lift, pitching moment and hinge moment characteristics of the airfoil are markedly changed from those of the unbeveled a flap of airfoil contour. The slope of the lift curve C_{l_α} and the lift effectiveness $\alpha\delta$ are decreased. The aerodynamic centers of the lift due to angle of attack and of the

lift due to flap deflection are both moved forward. The rate of change of hinge-moment coefficient both with angle of attack $C_{h\alpha}$ and the flap deflection $C_{h\delta}$ are increased positively. At small flap deflections, the bevel tends to have the same effect on hinge-moment as a balancing tab (see section 4.4); but at large deflections its effect is more nearly like that of a trim tab (see section 4.4). The effect of gap at the flap nose is critical, the parameter $C_{h\delta}$ being much more positive at small deflections with an open gap than with a sealed gap. This effect generally causes the hinge-moment characteristics of a flap with beveled trailing edge to be undesirably nonlinear unless the gap at the flap nose is sealed.

A preliminary correlation of hinge-moment data for sealed flaps with beveled trailing edges is given in reference 22. It was shown that the trailing edge angle is of fundamental importance in determining the hinge-moment slopes of beveled flaps. The result of correlating the hinge-moment characteristics of 16 different flap arrangements indicated that the effects of a beveled trailing-edge may be expressed by the following relations:

$$\Delta C_{h\alpha} = .00113\ \Delta\phi\ C_{L\ \alpha}\ (C_f/C)^{-1.0} \qquad (4\text{-}2)$$

$$\Delta C_{h\delta} = .011 \Delta\phi C_{L\delta}\ (C_f/C)^{0.4} \qquad (4\text{-}3)$$

The parameters $\Delta C_{h\alpha}$ and $\Delta C_{h\delta}$ are the increments in hinge-moment coefficient slopes caused by changing the trailing-edge angle of a flap by the amount $\Delta\phi$ degrees. The slopes $C_{L\alpha}$ and $C_{L\delta}$ are those for the rotor (wing)

with an airfoil contour flap. Equations (4-2) and (4-3) were obtained from the equations for the curves of (figure 150, Ref. 21), faired through the experimentally determined points. The hinge-moment characteristics of a beveled-trailing-edge flap can be predicted, by adding the incremental hinge moment due to bevel (see equation 4-2 and 4-3) to the hinge-moment characteristics of a flap without a bevel.

The results of the calculations for determining the flap chord and the trailing-edge angle required to obtain desired values of C_{h_α} and C_{h_δ} are shown in (figure 4, Ref. 22). From the curve of (figure 4, Ref. 22), it is evident that, if a flap is fitted with a bevel to reduce C_{h_δ} to zero or to a small negative value, C_{h_α} will have a large positive value. For beveled flaps the adverse effect is not so great as would be indicated by the value of C_{h_α} at $\delta_f = 0°$, because the effect of the bevel on C_{h_α} tends to disappear at large values of δ_f. As shown in (figure 2, Ref. 22), the effect of the bevel on C_{h_δ} becomes greater and the effect on C_{h_α} becomes smaller as the flap is increased. Reference 22 indicated that, to reduce both C_{h_α} and C_{h_δ} to zero, it would be necessary to use flap chords and trailing-edge angles outside the range covered by the available data.

The data in Refs. 23 to 26 indicated that thickening and beveling the control-surface trailing-edge reduce the slope of the airfoil lift-curve (C_{l_α}) and also the lift effectiveness ($\alpha\delta$) of the control surface. The maximum flap deflection generally can be sufficiently increased to counteract the loss in control associated with the use of bevels.

4.4 Tabs - An analysis was made in Ref. 27 for the hinge-moment altering effectiveness of the tab based on the available two-and three-dimensionals tab data of references 21 and 28, with additional data from references 26 and 29 to 40. The results of the analysis indicated that the effects of tabs on control-surface hinge-moments can be estimated from geometric characteristics of the tab-flap-airfoil combination with a reasonable degree of accuracy.

In general, the tab effect on the control-surface hinge-moments is reduced by increasing the airfoil trailing-edge angle and by any alteration of the airfoil surface condition or of the airstream, such as moving the transition forward, roughening the surface, or increasing the turbulence, that tends to increase the boundary-layer thickness near the trailing edge.

No data were presented on the tab lift effectiveness, which determines the loss in control-surface lift effectiveness resulting from balancing-tab action. The control surface lift effect can be evaluated as indicated by the analysis in Ref. 41. The data used in the correlation came from the following ranges of tab variables: tab-flap chord ratio from 0.10 to 0.50, flap-airfoil chord ratio from 0.12 to 0.60 and trailing edge angle from 7 to 31 degrees.

Sufficient data were available from which to draw quantitative conclusions concerning the effects of changing the size of the tab relative to the flap-airfoil combination, the effect of the trailing-edge angle, and the effect of control-surface overhang balance on the tab hinge-moment effectiveness. Insufficient data were available to determine

quantitatively the effect of the parameters that varied the tab hinge-moment effectiveness by changing the boundary-layer thickness over the tab. Sufficient data were available, however upon which to base qualitative conclusions concerning such effects.

Reference 42, also presented an analysis of a tab that is linked in such a manner that the tab deflection is proportional to the flap deflection and this is commonly referred to as a linked tab. Such a tab is a very convenient device in that it can be combined with any of the flap balances (e.g. internal balance, overhang balance etc.) and also because the balancing or unbalancing effect can be altered rapidly by changing the ratio of tab deflection with flap deflection.

A unique characteristic of a linked tab is that a large change in C_{h_δ} can be produced without causing any appreciable change in C_{h_α}; a small effect on C_{h_α} introduced by the linkage usually may be neglected. Almost any desired values of C_{h_α} and C_{h_δ} can therefore be obtained by combining the linked tab with one of the other balancing devices.

Since a balancing linked tab deflects in a direction opposite to that of the flap to which it is attached (see Figure 4.1), a reduction occurs in the net lift resulting from flap deflection. An analysis of a large amount of pressure-distribution data from Ref. 21 indicated that the most efficient trailing-edge balancing tab is one having a chord between 20 and 25 percent of the flap chord, because such a tab produces the least change in lift for a given change in flap hinge moment. On the other hand, a linked tab used to augment the lift of a flap (leading or unbalancing tab) should produce the greatest change in lift for a

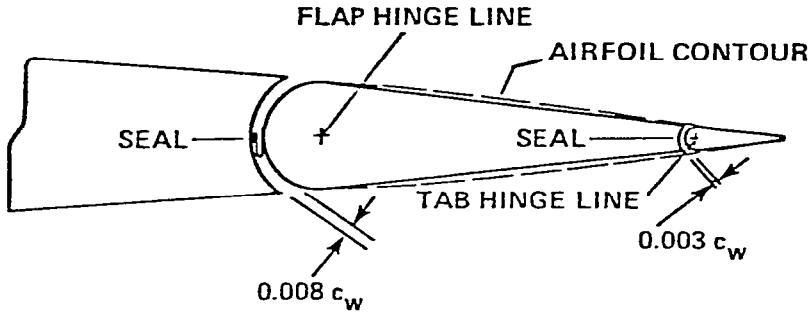

(SOURCE: REF. 43)

Figure 4.1. - Cross Section of Flap and trailing-edge tab.

given change in flap hinge-moment. A tab of this type is most efficient when the tab chord is equal to about 50 percent of the flap chord (see Ref. 42).

It was shown in Refs. 44 and 42, that the effect of linked tabs on the hinge-moment of flaps can be expressed as a function of the deflection ratio $\partial\delta_t/\partial\delta_f$ and of four factors that are defined as follows:

$$F_3 = \frac{b_t}{b_f}\left(\frac{C_t}{C_f}\right)^2 \tag{4-4}$$

$$F_4 = (C_t/C_f)^{0.7} + 0.51\ C_f/C \tag{4-5}$$

$$F_5 = 1.3 - 0.026\phi \tag{4-6}$$

$$F_6 = 1 - 0.85\left[\left(\frac{c_b}{c_f}\right)^2 - \left(\frac{t/2}{c_f}\right)^2\right] \qquad (4\text{-}7)$$

The factor F_3 accounts for the effects of the span and the spanwise location of the tab. The factor F_4 accounts for the effects of the tab chord and the flap chord. The factor F_5 accounts for the effect of the trailing-edge angle, and the factor F_6 accounts for the effect of the tab on the pressure difference across a flap overhang balance (either exposed or internal). The inclusion of the factor F_6 in the tab correlation makes unnecessary an adjustment in the increment $\Delta C_{h\delta}$ resulting from a flap overhang balance for the effect of the tab on the pressure across the overhang balance.

The term in the factors F_3, F_4, and F_5 can be evaluated, from charts given in (figure 40, Ref. 42), while the factor F_6 can be evaluated, from the chart in (figure 25, Ref.42).

The correlation of the effect of linked tabs on the flap hinge-moment parameter $C_{h\delta}$ is given in (figure 41, Ref. 42) and is based on data from reference 27. The equation of the correlation curve is

$$\Delta C_{h\delta} = 0.0222\, F_3F_4F_5F_6\left(-\frac{\partial\delta_t}{\partial\delta_f}\right) \qquad (4\text{-}8)$$

This equation may be used to estimate the incremental changes in $C_{h\delta}$ of a flap resulting from a given linked tab or to determine the configurations of tabs that are capable of producing a given change in $C_{h\delta}$ of a flap.

4.5 Allowable Tab Deflection - Experimental investigations conducted in references 32, 45, 46 and 47 indicated that the tab effectiveness decreases with an increase in the flap deflection. They also indicated

that there was reason to believe that a satisfactory maximum tab deflection exists between the angles of ±20 degrees for moderate flap deflections. The results indicated that, for a constant tab chord, it was better to use a large-span tab deflected to a small angle than a short-span tab deflected to a large angle.

4.6 Overhang Balance - Reference 48 presented an analysis of data for control surfaces having plain-overhang balance. The analysis was limited to the effects of overhang, nose shapes, gap and Mach number. Some empirical relations were derived that can be used for the prediction of the characteristics of balanced control surfaces from geometric constants (see also Ref. 44). Reference 48 considered the empirical relations only applicable to the preliminary design of control surface balances and to modifications of balances already in use.

The aerodynamic balancing effect of an overhang balance is considered to be a maximum when the contour of the balance conforms to the contour of the airfoil for the entire length of the overhang. Rounding or tapering the nose causes a reduction in the effect of the balance. The effects of variations in the nose shape were found to depend on the overhang length. Ref. 47, therefore, introduced a product of two factors as a measure of the net balancing effect of plain-overhang balances. The two factors are F_1, which is related to the length of the overhang, and F_2, which is related to the sectional shape of the balance nose. Thus, Ref. 47 finds as a balance factor (see also Ref. 44):

$$K_1 = F_1 F'_2 \tag{4-9}$$

$$F_1 = \left[\left(\frac{\bar{c}_b}{c_f} \right)^2 - \left(\frac{\bar{t}/2}{c_f} \right)^2 \right] \frac{b_b}{b_f} \tag{4-10}$$

and the expression for F'_2 is given in figure 4.2 for three general types of nose shapes. $\bar{c}_b$, c_f, and $\bar{t}$ indicate the root-mean square balance chord, control surface chord, and airfoil section thickness at the hinge line respectively. b_b and b_f indicate the span of the plain overhang balance and the span of the control surface. As may be seen from figure 4.2, the expression for F'_2 is, in general, the product of an area-moment ratio and a basic nose-shape factor that specifies the relative location of the point

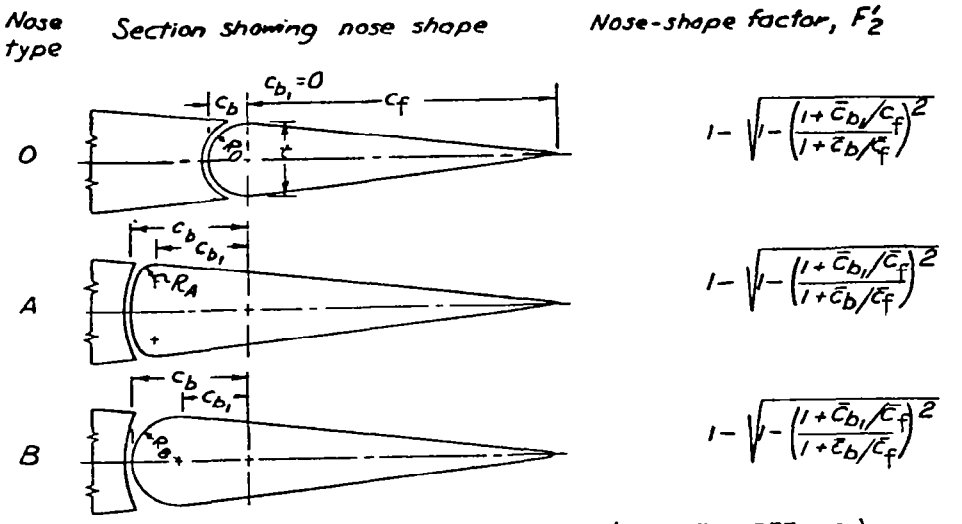

(SOURCE: REF. 42)

(Where $\bar{c}_b$ and $\bar{c}_{b_1}$ are the root-mean square balance chord and root-mean square contour balance chord over the span of the control surface respectively.)

Figure 4.2. - Various nose shapes considered in correlation of plain-overhang and corresponding expressions for nose-shape factor

of tangency of a circular-arc nose and the airfoil contour. The basic nose-shape factor F_2 is defined (see also Ref. 42) as:

$$F_2 = 1 - \sqrt{1 - \left(\frac{1 + \bar{c}_{b_1}}{\frac{\bar{c}_f}{1 + \bar{c}_b/\bar{c}_f}} \right)^2} \qquad (4.11)$$

where $\bar{c}_{b_1}$ is the root-mean-square contour balance chord. With the contour balance chord is meant the distance from the hinge line to the leading edge of the plain-overhang balance. It should be noted that for any overhang having a nose formed by circular arcs (nose types 0, A and B of figure 4.2)

$$F'_2 = F_2 \qquad (4\text{-}12)$$

Graphical solutions of the expressions for the overhang factor F_1 (for overhangs having spans equal to the control-surface span) and the basic nose shape factor F_2 are presented in figure 4.3. The value of F_1 for balances which do not extend over the entire span of the control surface is obtained by multiplying the value of F_1 obtained from figure 4.3 by the ratio of balance span to control-surface span. The use of figure 4.3 should allow a rapid determination of F_1 and F_2, provided the geometric constants $\bar{c}_b$, $\bar{c}_{b_1}$, $\bar{t}$ and $\bar{c}_f$ are known.

An analysis in Reference 22 of data on control surfaces with beveled trailing edges indicated that the effect of plan form of the wing could be accounted for reasonably well by assuming that both the lift-curve slope and the increment of hinge-moment slopes due to aerodynamic balance are affected by plan form changes in the same manner. The same assumption was made in Ref. 48 for the variation of hinge-moments with control deflection.

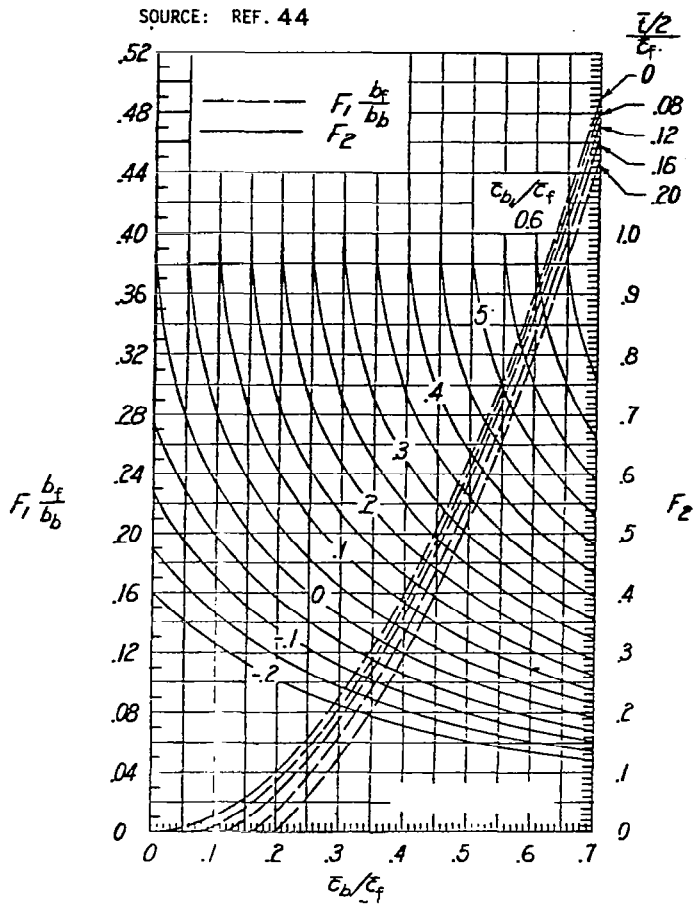

Figure 4.3. Charts for Determining Numerical Values of Overhang Factor F_1 and of Nose-Shape Factor F_2 from Geometric Constants of Balanced Flap

Ref. 48 uses (figure 2, Ref 48) to determine the effects of overhang balances on the variation of hinge-moment coefficient with control deflection. Figure 2 (Ref. 48) present curves of $\Delta C_{h\delta}/C_{l_1\alpha}$ or $\Delta C_{h\delta}/C_{l_1\alpha}$ plotted against the balance factor K_1. The parameter $C_{l_1\alpha}$ is the average value of the lift-curve slope over the span of the control surface and will be generally somewhat different for the lift-curve slope of the

entire rotor (see Ref. 48). A method for estimating the value of $C_{l1\alpha}$ for flaps of wings of various plan forms is given in Ref. 22. Figure 2, reference 48 indicated that the variation of the parameter $\Delta C_{h\delta}/C_{l1\alpha}$ with K_1 for finite span flaps was the same as the variation of $\Delta C_{h\delta}/C_{l1\alpha}$ with K_1 for two-dimensional flaps. The following equations were given in Ref. 44 for the hinge-moment parameter increments:

$$\Delta C_{h\alpha} = 0.017 \frac{AR}{AR + 2} F_1 \qquad (4\text{-}13)$$

$$\Delta Ch_{\delta} = 0.10 \frac{AR}{AR + 2} F_1 F'_2 \qquad (4\text{-}14)$$

The data used in the correlation of $\Delta C_{h\delta}$ were obtained from two-dimensional flap models.

Charts for estimating the required length of balances having several representative nose shapes (see figure 4.2) are presented in (figure 27 Ref. 44). For a given design problem, the value of the product $F_1F'_2$ corresponding to the required value of $\Delta C_{h\delta}$ must first be obtained from the correlation presented in (figure 26, Ref. 44). The value of $\overline{C}_b/\overline{C}_f$ required for this value of $F_1F'_2$ may be estimated from (figure 27, Ref 44) for any of the nose shapes considered. The charts given in (figure 27, Ref. 44) were derived for flaps on airfoils having the thickness distribution defined in reference 49. The charts may be used, however, to obtain first approximations to the required overhangs for flaps on airfoils having other thickness distributions (see Ref. 44). For such airfoils, more accurate values for the required overhangs can be obtained by calculating the value of the product $F_1F'_2$ corresponding to the first approximation value of C_b/C_f from the expressions given in Figure 5.2 for F'_2 and the

charts of Figure 4.3 for F_1 and F_2. However, if the calculated value is obtained from (figure 2, Ref. 48), a new value of $\overline{C_b}/\overline{C_f}$ must be assumed and the process repeated until satisfactory agreement is reached between the required and the calculated values of $F_1F'_2$.

The lift-effectiveness parameter $\Delta\alpha/\Delta\delta$ is changed somewhat by an overhang balance and the magnitude of the change is dependent on the gap at the balance nose. A correlation of these effects is given in Reference 21, 44, and 48; and the faired curves of that correlation are reproduced in (fig. 29, ref. 44). The value of $\Delta\alpha/\Delta\delta$ increases as the balance (defined by the product $F_1F_2^1$) is increased and the rate of increase is greater for the larger gaps. For the sealed-gap condition, the increase in $\Delta\alpha/\Delta\delta$ with increased flap balance results from an increase in C_{l_δ}; whereas, for highly balanced flaps, the increase in $\Delta\alpha/\Delta\delta$ with increased gap size is caused primarily by a decrease in C_{l_α} (see refs. 21 and 44). The $\Delta\alpha/\Delta\delta$ values given in (figure 29, ref. 44) are applicable only to small deflections, and because of the reduction with increased balance of critical deflection (δ_{cr}), the maximum lift increment of a highly balanced flap usually is considerably less than the maximum lift increment of the corresponding plain flap. The critical flap deflection (δ_{cr}) is defined as that deflection at which plain-overhang balance is no longer effective in reducing the slope of the hinge-moment curve.

The fact that δ_{cr} varies approximately as $F'_2\sqrt{F_1}$, whereas ΔC_{h_δ} varies as $F_2^1F_1$, indicates that for the same degree of a balance a larger increment of lift probably can be obtained from a flap having a

long overhang and a moderate nose shape type B (fig. 4.2) than from a flap having a short overhang and a blunt nose shape similar to type A (see fig. 4.2).

A factor that is probably quite closely related to δ_{cr} is the magnitude of the peak pressures over the balance nose. If $\Delta C_{h\delta}$ is assumed to remain the same, a short blunt-nose balance produces higher peak pressures than a long balance with a moderate nose shape. The high peak pressure associated with the very blunt nose shape increases the possibility that the control surface may become overbalanced at high Mach numbers and probably increase the rate at which Mach number reduces the value of δ_{cr}. The peak pressures increase the possibility that supercritical local velocities will be reached over the nose of the balance. With regard to the rotor the long overhangs will permit static balance to be obtained by the addition of a minimum of otherwise nonuseful weight. Control surfaces with bluntnose overhangs (types A and B), figure 4.2 have already shown some tendency toward increased balance at high deflections (see refs. 50 and 51).

As pointed out earlier in the section, the parameter $\Delta C_{h\alpha}$ is relatively independent of nose shape for sealed balances and appears to depend principally on the balance chord. The choice of the best combination of nose shape and overhang for a given $\Delta C_{h\delta}$ may therefore be influenced by the value of $\Delta C_{h\alpha}$ obtained; and the degree of influence may depend on the specific application.

The choice of an open or sealed gap for use with the overhang will be influenced by the fact that the nose shape has more effect on $C_{h\alpha}$

with the gap open than with the gap sealed. For balances having values of K_1 (balance factor) greater than about 0.05, the use of an open gap generally increase the lift-effectiveness parameter of the control surface (see refs. 50 and 51). Part of the gain in the lift-effectiveness parameter of the control surface, however, is obtained at the expense of a loss in C_{l_α}.

For the variable camber flap arrangements, the selection of overhang and nose shape may be made principally from a consideration of the value of C_{h_δ} required; but the adjustment of the nose shape or overhang of flaps to obtain a desired value of C_{h_α} is not recommended. A nose shape similar to type B (see figure 4.2) seems the most promising of those tested: therefore, for the present analysis, it should only be necessary to determine the overhang for a nose shape of type B (fig. 4.2) required to give a value of C_{h_δ} already decided upon. The value of C_{h_δ} actually obtained may be adjusted later within a limited range, by making minor modifications to the nose shape, without, changing the length of the overhang (see ref. 44). The effect of nose shape on the peak pressures, the critical deflection, however, must be given consideration.

The hinge-moment parameters C_{h_δ} and C_{h_α} are of almost equal importance for control surfaces, and the selection of the overhang and nose shape therefore depends on obtaining desirable values for each of these parameters. As it has already been pointed out, the nose shape has little effect on C_{h_α} provided the gap is sealed. The overhang may consequently be selected to obtain the desired value of C_{h_α}; and the nose

shape may then be selected to obtain the desired value of C_{h_δ}, due consideration being taken of the effect of nose shape on the peak pressure, on the critical deflection; and on the variation of C_{h_δ} with deflection. If the desired value of C_{h_δ} cannot be obtained by selection of only the nose shape, some adjustment of the overhang may be necessary, and compromise values of C_{h_δ} and C_{h_α} will thereby be obtained.

4.7 Sealed Internal Balance - An internal balance is a feasible and an aerodynamically desirable means of controlling the magnitude and the direction of the rate of change of flap hinge moment with angle of attack and with the flap deflection. Because the internal balance is entirely concealed within the airfoil contour, the lift, the drag, and the pitching-moment characteristics of the control surface are in no way affected by the presence of the balancing surface. Thus, the internal balance can then be referred to as a mechanism by which the pressure difference between two points on the airfoil is used to act upon a flat plate or similar devices entirely enclosed with the airfoil profile and thus to work in deflecting the control surface.

Several types of internal balances were discussed in ref. 52. It was shown that the most commonly used, although not necessarily the most aerodynamically desirable type of internal balance is that with a balancing plate rigidly attached to the flap and with the vents located near the hinge axis.

It was shown in ref. 21, that the increments of hinge-moment coefficient slope caused by a sealed internal balance vented near the hinge

may be expressed by the equation for the faired correlation data (also see ref. 53) as:

$$\Delta C_{h_\alpha} + .0237\left[\left(\frac{c_b}{c_f}\right)^2 - \left(\frac{t/2}{c_f}\right)^2\right] c_f/2 \qquad (4\text{-}15)$$

$$\Delta C_{h_\delta} = 0.359\left[\left(\frac{c_b}{c_f}\right)^2 - \left(\frac{t/2}{c_f}\right)\right]\left(\frac{c_f}{c}\right)^{1.4} \qquad (4\text{-}16)$$

where c_b is the chord of the balancing surface, c_f is the chord of the flap measured at any airfoil section from hinge axis to trailing edge of the airfoil, c is the chord of the airfoil section; and t is the thickness of the control surface at hinge. These correlations are believed to be most reliable when the following conditions (also see ref. 21) apply:

(1) The balance plates are attached rigidly to the noses of the flaps and the vents are as close to the hinge line as practicable.

(2) There is no leakage across the seal.

(3) The cover plates are of airfoil contour.

Small variations in any of these conditions may cause large changes in the effect of an internal balance.

Refs. 44 and 54, also discussed sealed internal balances. They indicated that the chordwise pressure distributions of a rotor (wing) with a plain sealed flap are unaffected by the addition of a sealed internal balance.

Sealed internal balances for use with flaps (see ref. 44) usually consist of a plate (attached rigidly to the flap nose) in a chamber that is vented to the airstream in such a manner that a pressure difference across the plate is created principally by flap deflection and to a lesser

degree by changes in the angle of attack because this is where it experience the greatest pressure differential in the vicinity of the flap. A flexible seal connects the nose of the balance plate to the forward wall of the balance chamber.

For a sealed internal balance, the balancing force can normally be obtained from the pressure differences between two chambers in which the air is essentially static. The balancing moment can then be derived from the geometry of the system provided the pressure difference is known.

For the variable camber rotor flap arrangements, the configuration consist mainly of overhang balance (balancing surface), sealed to the forward structure by a flexible material, capable of sustaining only tensile stresses (see figure 4.4).

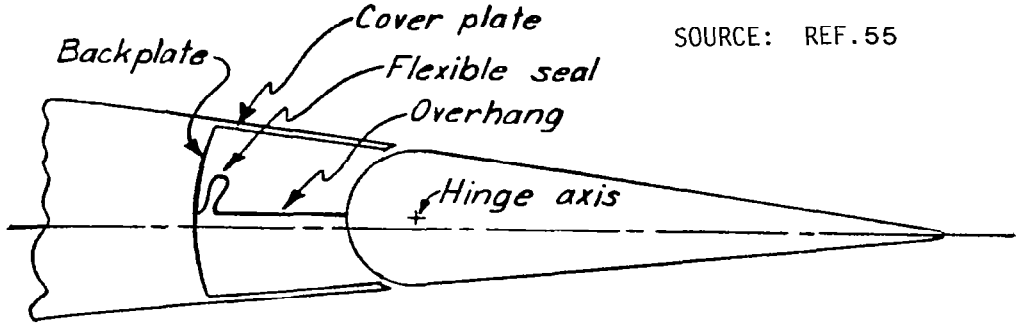

SOURCE: REF.55

Figure 4.4 Schematic diagram of a typical internal-balance arrangement for the Variable Camber flap on a rotor.

The moment resulting from the type of balance shown in figure 4.4 can be determined by the following methods:

(1) The method of resolution of forces consists of finding the forces exerted by each part of balance system as a result of a pressure difference across these parts. The moments of these forces about the control-surface hinge are then added to get the total moment of the balance system.

(2) The method of volume displacement consists of finding the rate of change of volume swept by the balance with deflection. The moment of the balance is:

$$M_B = \left(\frac{dv}{d\delta}\right) \Delta p \qquad (4\text{-}17)$$

where Δp is the pressure difference across the balance.

An internal balance with seal and vertical-line backplate is shown in figure 4.5. The moments of such balance can be written as the sum of

SOURCE: REF. 54

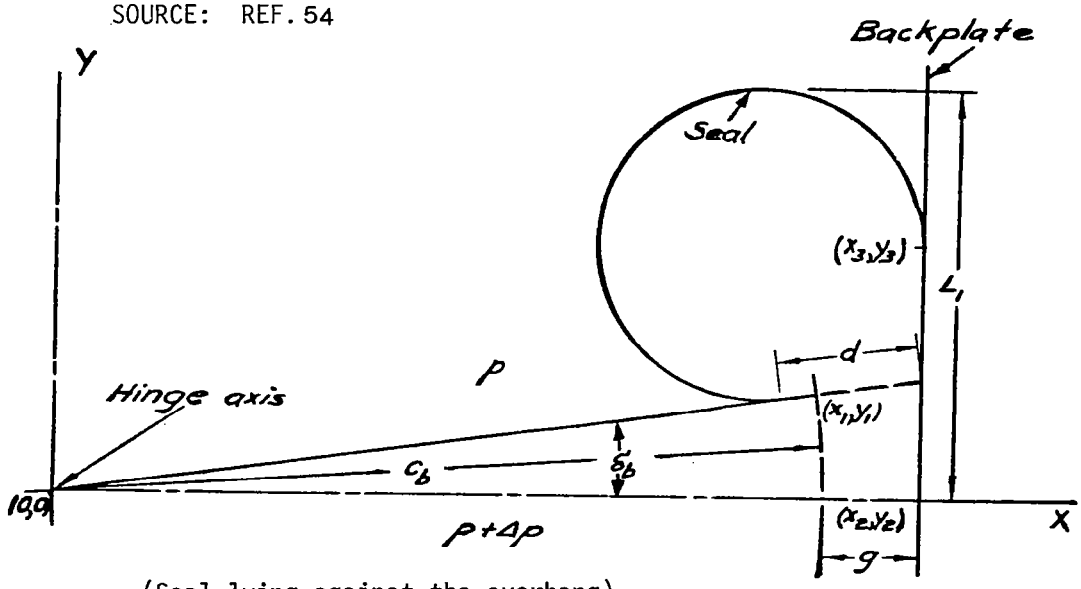

(Seal lying against the overhang)

Figure 4.5 - Internal balance with Seal and vertical-line backplate

the moment resulting from the overhang and that resulting from the seal; therefore:

$$M_B = \frac{\Delta p}{2}\left[c_b{}^2 - (t/2)^2\right] + M_s \tag{4-18}$$

where c_b is the overhang chord; t is the thickness of overhang at hinge axis; and M_s is the seal-moment or incremental hinge-moment resulting from seal of unit span (two-dimensional). The moment exerted by a seal can be expressed in terms of the seal-moment ratio (m_s) as:

$$M_B = \frac{\Delta P}{2}\left[c_b{}^2 - (t/2)^2\right] + \frac{\Delta P}{2}\, c_b^2 m_s \tag{4-19}$$

or, the increment of hinge-moment coefficient caused by the balance can be related to the pressure coefficient across the balance or resultant pressure coefficient (P_R) and to the geometry of the system by the following equation for a unit span (two-dimensional) (also see ref. 55) as :

$$\Delta C_h = 1/2\ P_R\left[\left(\frac{\bar{c}_b}{c_f}\right)^2 (1 + m_s) - \left(\frac{\bar{t}/2}{c_f}\right)^2\right] \tag{4-20}$$

where $\bar{c}_b$ is the root-mean square chord of the balance plate and m_s is the ratio of the moment contributed by the balance plate, $\bar{t}$ is the root-mean square section thickness at the flap hinge line.

To obtain numerical values for ΔC_h, an investigation was made as to the variation of the seal-moment ratio (m_s) with two important balance dimensions-the width of the gap to be sealed and the developed width of the seal. Values of m_s were determined analytically in ref. 54; and checked experimentally in ref. 55 for several typical balance arrangements.

The characteristics of a flap having almost any arrangements of the balance plate and of the flexible seal can be calculated from the characteristics measured for one particular balance configuration provided the pressure difference between the two chambers are known.

For the arrangement represented in this analysis, the balanced surface is attached rigidly to the flap in such a manner that its angular or linear travel is directly proportional to the flap deflection; the vents are so located that the balanced-actuating pressure varies with flap deflection and with angle of attack in approximately the same manner as does the hinge-moment of the unbalanced flap. If the pressure coefficient across balance (P_R) which was obtained from the pressure distribution of the VR-7 airfoil modified with a 0.50c trailing edge flap and the balance plate deflection (δ_b) are of the same algebraic sign, values of m_s should be taken from (figs. 14 to 21, ref. 55), but on the other hand, if P_R and δ_b are of opposite signs, values of m_s should be taken at negative values of δ_b (figs. 14 to 21, ref. 55). Also see figure 5.6 for sign conventions for overhang deflection.

Hinge moments of internally balanced control surface normally become large at large deflections as a result of a decrease in $\partial P_R/\partial\delta$ with deflection. In order to offset somewhat the effect of a decrease in $\partial P_R/\partial\delta$ with deflection and to give the most nearly linear control-surface hinge moments, $\partial m_s/\partial\delta_b$ should have a positive value. (A positive value of $\partial m_s/\partial\delta_b$ that increased with deflection would even be more desireable but generally cannot be obtained). The positive value of $\partial m_s/\partial\delta_o$ may be considered favorable inasmuch as linear or nearly linear control-surface

SOURCE: REF. 54

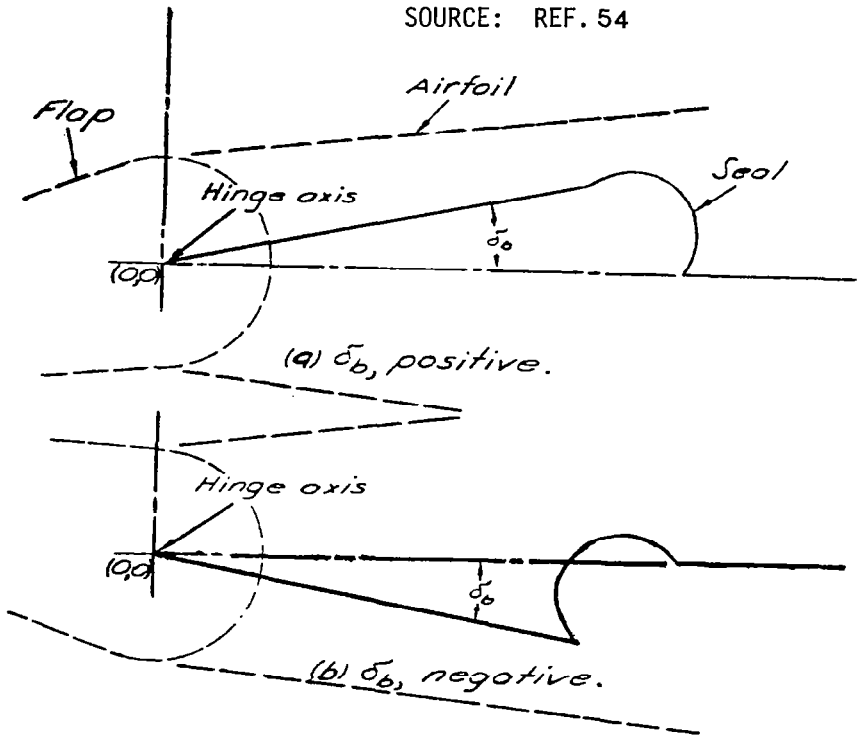

Figure 4.6. Sign Conventions for Overhang deflection

hinge moments, although not altogether necessary, are generally desireable (see ref. 54).

4.8 Flexible Seals - The flexible seals analyzed in refs. 54 and 55 were assumed to be nonporous, inextensible, perfectly flexible, and weightless. These assumptions imply that the unrestrained part of the

seal forms an arc of a circle and has a tensile force per unit span, of $T = \Delta pr$ acting everywhere tanqent to the arc (see fig. 4.5). The moments resulting from these seal arise either from the tensile stress in the seal or from the seal lying along and equalizing the pressure over part of the overhang (see ref. 54).

If the resolution-of-forces method (see section 4.7) is applied to the seal shown in figure 4.5, the lever arm of the tensile force in the seal is zero. The reduction in effective overhang chord caused by such seals is equal to the amount of overhang covered by the seal; this amount can be determined as follows (also see ref. 54).

$$S = \left(\frac{d}{\tan \frac{90° - \delta_b}{2}} \quad \frac{270° + \delta_b}{57.3} \right) + (d + x_2 \tan \delta_b) + (d + c_b + x_2 \sec \delta_b) \tag{4-21}$$

where the first term in equation (4-21) represents the width of the seal in a free arc; the second term the width of seal lying along the backplate; and the third term, the width of seal lying along the overhang. In order to find the amount of overhang covered by the seal, the distance (d) must be known. This quantity can most conveniently be found if d is plotted against the seal width s for various overhang deflections (see ref. 54). Appropriate values can then be read from the curves.

The seal-moment characteristics over the deflection range for various sizes of fabric seal and sealed nose gap, with and without overhead limit were investigated in ref. 55. The effect of changes in gap width can be seen best by reference to (figure 10, ref. 54 and figure 15, ref. 55)

respectively, where it is evident that an increase in gap width for a seal of constant width increases the seal moment at small positive deflection and decreases the seal moment at large positive deflections; the effect is therefore, a change in $\partial m_s/\partial \delta_b$ in the negative unfavorable condition. If the most nearly linear control-surface hinge-moment characteristics over the entire deflection range are desired, small gaps of the order of $g \leq 0.1$ should be used (preferably $g = 0.005$). In terms of control-surface hinge-moments, increasing the gap width tends to result in high control-surface hinge moments at large control-surface deflections and low or overbalanced moments at small control-surface deflection.

The effect on the seal moment characteristics of varying the seal width, with other variables kept constant, is evident in (figures 14 to 19, ref. 55). The curves indicated that m_s which depends on seal width, for a given sealed-gap width decreases at small positive deflections and increases at large positive deflections as the seal width increases. The curves also indicated that, for a given sealed-gap width, as the seal width increases, the maximum value of m_s generally increases; and occurs at an overhang deflection that increases the seal width. It appeared, therefore, that an optimum balance configuration would employ a seal width such that the seal would barely touch the chamber ceiling when maximum deflection is attained (see figs. 5 and 8, ref. 55).

4.9 Off-Center Seal Attachment - A comparison of seal-moment characteristics obtained with various types of seal attachments was made in ref. 55. The result showed that the seal-moment characteristics obtained

with the off-center attachment were generally unfavorable over the deflection range because a decreasing balancing tendency or an increasing unbalancing tendency is indicated, regardless of the point of attachment. It was shown that when attached above center, the seal invariably lay against the backplate and there was an overhead restriction at positive deflections (see figures 7 and 12, ref. 55); while, when attached below the center, the seal had a moment vector that tend to decrease positively, and then increase negatively with overhang deflection (see figs. 6 and 13, ref. 55). The effects account for the unbalancing characteristics of this types of seal attachment.

The effect of attaching the seal off-center to a backplate, when the seal did not contact the balance-chamber ceiling was to shift the seal-moment curve by an angle the sine of which was equal to the off-center displacement (expressed as a fraction of the overhang). The curve of (fig. 25, ref. 55) approximately verify this conclusion.

Since an off-center seal attachment produces an unbalancing effect on the overhang caused by flap deflection or the increase in the angle of attack, this type of seal attachment is believed by the author to be undesirable and should be avoided.

4.10 Effect of Vent location on $P_{R\alpha}$ and $P_{R\delta}$ - An indication of the probable effects of changes in the chordwise location of the balance-chamber vents (determined from data in refs. 21 and 53) is given in (fig. 36, ref. 42). It was noticed, that moving the vents forward of the hinge line causes $P_{R\alpha} = (\frac{\partial P_R}{\delta \alpha})$ to increase and $P_{R\delta} = (\frac{\partial P_R}{\partial \delta_f \alpha})$ to decrease. For the type of internal balance, considered in the correlations, the

variation of the resultant pressure across the balance plate with deflection was about two-thirds the variation of the peak resultant pressure at the hinge with deflection. Also it has already been indicated in section 4.7, that the vents are to be close to the hinge line as practicable; but contour changes caused by aerodynamic forces may be of sufficient magnitude to produce objectionable stick-force characteristics for flaps that otherwise would be satisfactory. The type and extent of covering distortion depends on the external pressure distribution over the surface of the flap, on the pressure inside the flap, on the initial tension of the covering material, on the modulus of elasticity of the covering material, and on the method of attachment of the covering material. Also different vent locations may cause positive, negative or static internal pressures.

(1) Positive internal pressures causes both surfaces of the flap to bulge. Bulging of the forward part of the flap seems to have little effect on the hinge-moment parameters, but the increase in trailing edge angle causes these parameters to become less negative. The stick forces, therefore, are decreased and may become overbalanced if the undistorted flap is designed to give stick forces within the required limits. Also large positive internal pressures can result in complete failure of fabric-covered flaps and in the failure of rivets used to attach the metal skin to the flap ribs. Loads of this type can be controlled to some extent by careful selection of the vent locations, but the possibility of high skin stresses resulting

from inadvertent variation in the vent locations should not be overlooked (see ref. 42).

(2) Negative internal pressures causes both flap surfaces to be drawn in with the result that the trailing edge-angle is decreased. The parameters C_{h_α} and C_{h_δ} therefore become more negative and the stick forces may increase to such an extent that the pilot's ability to control the helicopter may be seriously restricted at high speeds.

(3) For internal pressures near static pressure, the external-pressure differential can cause both surfaces to bow in the same direction.

4.11 Effect of Cover-plate Misalignment on C_{h_α} and C_{h_δ} - The characteristics of an internally balanced flaps have been found to be very sensitive to the alignment of the cover plates just forward of the vents. The effects of misalignment as determined in a few tests, are shown in (figure 37, ref. 42) and the data are presented in ref. 18. When small flap deflections and small changes in angle of attack are considered, bending the cover plates slightly out had been shown to decrease the effect of the balance on C_{h_α} and increases the effect of the balance on C_{h_δ}. While bending the cover plates out had been shown to decrease the deflection range for which the balance has an effect on the hinge-moment slopes, probably because of earlier separation of the flow.

4.12 Influence of Gap at Flap Nose - Though it is known that the existence of a gap at the flap nose has an effect on the hinge-moment parameters; and though many publications studied the influence of such a gap, no analytical method was found to take the influence of a gap into account. Reason for this is probably the fact that the influence of the gap is dependent upon size and location of the gap as well as on the nose shape of the control surface (blunt, medium or sharp). Reference 56 presents the following empirical method to estimate the influence of some of the variables on the lift-curve slope $C_{L\alpha}$.

The wing lift-curve slope $C_{L\alpha}$ was given in Ref. 56 by the following relation:

$$C_{L\alpha} = \frac{AR\, C_{l\alpha}}{ARE_e + \frac{57.3}{\pi} C_{l\alpha}} \qquad (4\text{-}22)$$

where E_e is the effective edge velocity correction factor (see ref. 57); and the value of $C_{l\alpha}$ for a given section is expressed empirically as follows:

$$C_{L\alpha} = C_{L\alpha_o} \frac{(C_{l\alpha})_{\text{gap open}}\ (C_{l\alpha})_{\text{sealed}}}{(C_{l\alpha})_{\text{gap sealed}}\ (C_{l\alpha})_{\text{faired}}} \qquad (4\text{-}23)$$

where $C_{l\alpha_o}$ can be read from (fig. 42, ref. 56) which shows the effect of airfoil thickness and trailing-edge angle on section lift-curve slope. Figure 43 (see ref. 56) shows the plots of $\{(C_{l\alpha})_{\text{gap open}}\}/\{(C_{l\alpha})_{\text{gap sealed}}\}$ against break location for various gap sizes. The break location indicates the position of the gap along the chord. The curves in (fig. 43, ref. 56) show that $\{(C_{l\alpha})_{\text{gap open}}\}/\{(C_{l\alpha})_{\text{gap sealed}}\}$ decreases as the gap is moved toward the leading edge of the airfoil until it reaches a position of about 0.50c. The gap sizes ranges from 0.001c to 0.010c and the data indicate a decrease in $\{(C_{l\alpha})_{\text{gap open}}\}/\{(C_{l\alpha})_{\text{gap sealed}}\}$ as the gap size increase.

Figure 44 (see Reference 56) presents the plots of $\{(C_{l\alpha})_{\text{sealed}}\}/\{(C_{l\alpha})\}_{\text{faired}}$ against break location giving the effect of the break in the airfoil contour on $\{(C_{l\alpha})_{\text{sealed}}\}/\{(C_{l\alpha})_{\text{faired}}\}$. Comparison of measured values of the lift-curve slope with calculated values using the above method is shown in Ref. 56.

Generally, the plain flap gives a greater lift effectiveness with smaller hinge-moments with the flap gap sealed than with it unsealed. The negative slope of $C_{h\alpha}$ and $C_{h\delta}$ decreases with sealing the gap at the nose of the flap.

For flaps having overhang balance and aerodynamic balance, the following effects of the gap can be noticed. Unsealing the gap generally causes an increase in lift-effectiveness $\alpha\delta$ for flaps with blunt and medium nose overhangs and a decrease in $\alpha\delta$ for plain flaps and flaps with elliptical nosed overhang. Unsealing the gap at the flap nose makes $C_{h\alpha}$ and $C_{h\delta}$ less negative. Changing the nose shape from blunt to elliptical makes $C_{h\alpha}$ more negative for the sealed gap and less negative for the unsealed gap.

It has already been mentioned in section 4.7, that the presence of a gap i.e. the existence of a leakage, causes large unpredictable effect in case of an internal balance. Also the effect of a gap at the nose of a tab may be very large, although the available data on this effect are too inconsistent to permit any reliable correlation. For some flaps, such a gap has resulted in a reduction of the tab balancing effect by as much as 50 percent. In any design the tab should be sealed or at least made as small as possible (see section 4.4).

From the above discussion, the difficulty in predicting the influence of a gap at the flap nose on the hinge-moment parameters become clear.

4.13 Application of Equations and Design Charts - The procedure to be followed in the preliminary design of flaps for the Variable Camber Rotor depends to a large extent on other aspects of the rotor design. In the present analysis an investigation is made of the chordwise parts of the rotor that must be allocated to the flaps plus balance in order that specified stick forces may be obtained. The flap configuration chosen in this design consists of a sealed internally balanced flap. Some of the equations and charts, which already have been presented in earlier sections, are used in arriving at the flap arrangements that would be expected to meet certain required conditions.

In order to show how the characteristics of a sealed internally balanced flap can be obtained from those of the sealed unbalanced flap (plain flap) and to indicate the magnitude of some of the effects about which analysis have been drawn, the effect of the balanced configuration on the hinge-moment characteristics for the section shown in fig. 4.4 has been determined. The characteristics of the unbalanced flap section are shown in figure 4.7. From equation (4-20) the incremental hinge-moment coefficient were computed for four balances having vertical-line backplate. The values of the pressure coefficient across the balance P_R for use in equation (4-20) were obtained from the calculated value for the VR-7 airfoil (see chapter 3). The vertical line clearance (L_1) (see figure 4.5) required for seal to develop moments for the variable camber

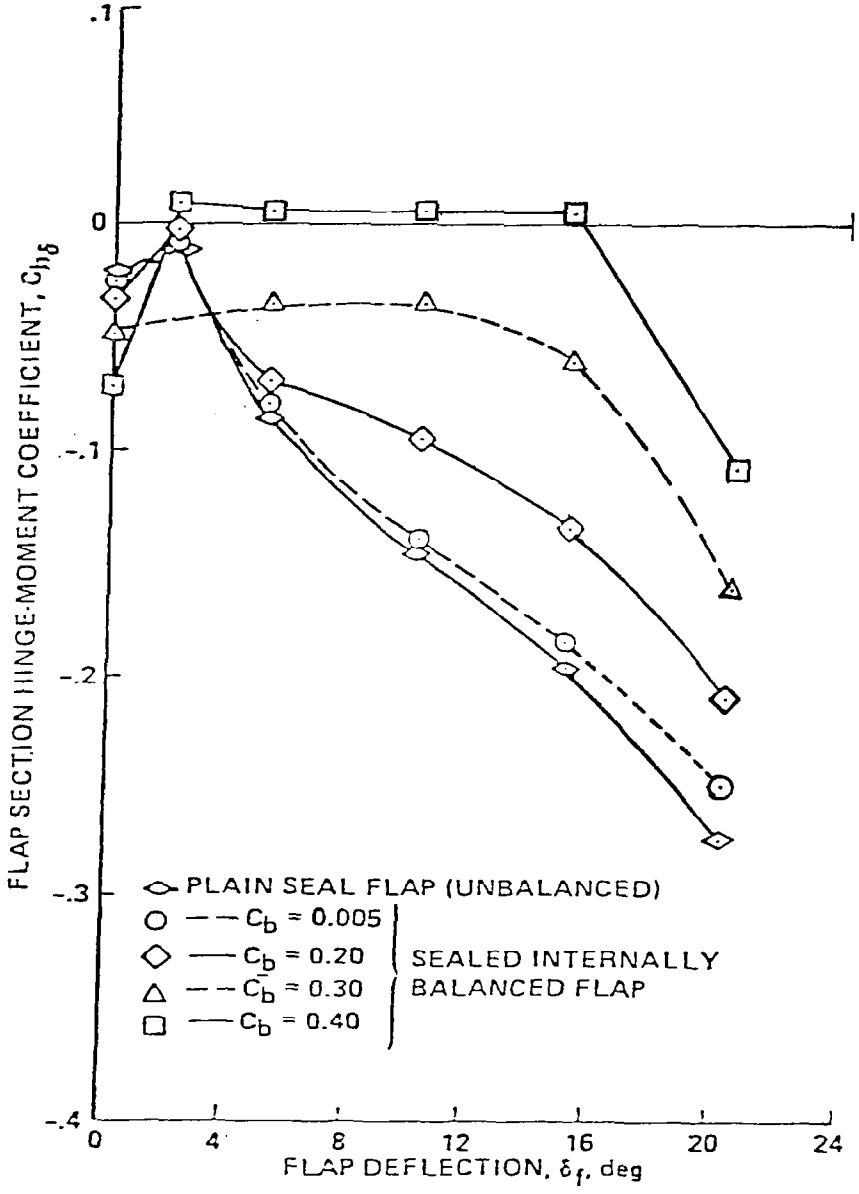

Figure 5.7. - Hinge-moment characteristics of a flap on the VR-7 airfoil having four balance configuration with the same vertical-line backplate. $\alpha = 0^\circ$

flap arrangement was obtained from (fig. 14, ref. 54) as $L_1 = 0.34$ for a deflection range of 0 to ±20 degrees, ample space is provided for the seal to develop the moments indicated in (fig. 10, ref. 54). The width of the seal(s) used in this analysis was obtained from (fig. 14, ref. 54), and was believed to be approximately 0.4 ft. In ref. 54, it was shown that if the most nearly linear control-surface hinge-moment characteristics over the entire deflection range is desired, small gaps of the order of $g < 0.1$ should be used. In light of the numerous literature surveyed, it is recommended that the gap size to be considered for this present analysis should be 0.005 ft (0.6 in). Values of m_s for computing the exact balancing moment over the deflection range for a seal width(s) of 0.4 and a sealed gap width of 0.005 were interpolated from the data in (figure 10, ref. 54 and figs. 14 and 15, ref. 55) respectively.

The hinge-moment parameters of the balance flap were obtained by considering the plain flap and the effect of the balance separately as follows (see also refs. 44 and 55):

$$(C_h)_{\substack{\text{balanced}\\\text{flap}}} = (C_h)_{\substack{\text{plain}\\\text{flap}}} + (\Delta C_h)_{\text{balance}} \tag{4-24}$$

Table 4-1 shows a sample of the computations required for obtaining hinge-moments of the balanced flap from this equation.

4.14 Assessment of Feasibility for Getting Low Hinge-Moment - The estimation of control-surface hinge-moments is one of the most important and one of the most difficult problems confronting the aerodynamicist. This is due to the fact that these moments create the forces which the

pilot must overcome at his cockpit controls and which give him a sense of "feel" of the helicopter/airplane (see ref. 58).

Prediction of the control forces required of the pilot for maneuvering the helicopter within its aerodynamic and structural limitations for the variable camber configuration will be based on an estimate of these parameters, and the success of the concept depends largely on how accurately this estimate is made.

The many variables encountered in the aerodynamic design of a flapped lifting surface make it difficult to obtain a generalized solution. Thus the theoretical results presented in this analysis may be limited to (1) the range wherein the variation of hinge-moment coefficient with angle-of-attack and with flap deflection is linear; (2) flaps having internally sealed radius noses; (3) low subsonic speed.

In sections 4.1 to 4.13, several methods of predicting the hinge-moment parameters of various types of control surfaces were discussed. The correlations that have been presented may be used to illustrate the relative effects of the various balancing devices on the hinge moment parameters of C_{h_α} and C_{h_δ}. The variation in these parameters that might be expected to accompany the addition of each of the balances for a 0.50c plain flap on an H-34 standard four-bladed, fully articulated helicopter rotor are shown in table 4-1. By means of methods which have already been described, the values of C_{h_α} and C_{h_δ} of the true-contour plain flap were estimated. The incremental ΔC_{h_δ} required for a given reduction in stick force is largest for balances that produce the

Table 4-1

COMPUTATION OF HINGE MOMENT COEFFICIENTS OF BALANCED FLAP

FROM THOSE OF UNBALANCE OR PLAIN FLAP: $\alpha = 0°$ and $C_b = 0.30$

Flap Deflection δ_f (deg.)	Resultant Pressure coefficient P_R	Balance Plate Deflection δ_b	Seal Moment Ratio m_s	$1/2\left(C_b/C_f\right)^2$ .18 x (2)	$1-\left(\frac{t/2}{C_f}\right)^2$ .9777 + (4)	Incremental hinge-moment coefficient caused by balance ΔC_h (5) x (6)	$(C_h)_{plain\ flap\ or\ unbalance}$	$(C_h)_{balance}$ (7) + (8)
0	-.104	0	.5080	-.0187	1.4857	-.0278	-.0218	-.0496
2	.0431	2	.4990	.0078	1.4677	.0114	-.01194	-.00054
5	.204	5	.4625	.0367	1.4402	.0529	-.0888	-.0359
10	.449	10	.3800	.081	1.3577	.1099	-.1457	-.0358
15	.638	15	.1850	.115	1.1627	.1337	-.1949	-.0612
20	.752	20	-.315	.135	0.6627	.0895	-.2527	-.1632

greatest changes in C_{h_α} for a given change in C_{h_δ}. In the order of increasing effects on C_{h_α} for a given effect on C_{h_δ}, the various balances may in general be listed as follows: balancing tab, sealed internal balance, plain-overhang balance, and balance obtained by increasing the trailing-edge angle.

It was found that all the devices discussed will give lower level hinge-moment than that experienced by the plain flaps. Adequate comparisons between the different devices themselves to establish the superiority of one system over another was not made in any of the reviewed reports. It was not possible to make this comparisons here due to the many differences in test conditions within the literature surveyed.

The wide variation in the forms of aerodynamic balances employed is indicative of the lack of any completely satisfactory method of balance. The reduction in control force provided by the balance is usually accompanied by one or more disadvantages, such as insufficient balance or overbalance for some flight conditions, reduction in control effectiveness, loss of "feel" in the control, etc. Other considerations which may impose limitations is the most desirable length of overhang to be used for aerodynamic balance; since a long overhang will require a large part of the fixed structure (forward section) of the rotor to be cut away to allow for free movement of the balance.

It is frequently found that full balance cannot be obtained in a satisfactory manner by the use of a single device; for example, a large degree of balance with the inset-hinge type of control surface requires such a long overhang that the permissible deflection of the flap is

limited. It is helpful, therefore, to have available several independent means of reducing hinge-moments.

To be able to state that one system is the best in reducing hinge-moment, the following should be done:

(1) The qualities wanted must be stated. These qualities will be specifications of hinge-moment level wanted or desired.

(2) Enough tests must be run using different systems and devices to determine the performance level of each. A comparison between each devices or system can then be made.

The combinations of two or possibly three types of balance may be desirable to obtain specified values of the flap hinge-moment parameters or to avoid the difficulties that are encountered almost invariably when a large amount of one type of balance is used. A system, using a spring-tab with an aerodynamic balance has been known to reduce hinge moment to any desired level up to deflections at which the tab has lost effectiveness. An alternative arrangement may be to use a narrow chord flap with a sealed trailing edge in combination with sealed internal balance vented at the hinge line. The bevel will cause a large reduction in C_{h_α} and small reduction in C_{h_δ}, whereas the sealed internal balance vented at the hinge line will cause a large reduction in C_{h_δ} and a small reduction in C_{h_α}. With such a combination, the hinge-moment parameters probably could be adjusted to any desired value. Also the beveled trailing edge should be useful in combination with other types of balances, because it involves no additional linkages (see ref. 59).

In view of the various aerodynamics techniques to minimize hinge-moments level discussed, it is the author's feeling that a system incorporating a sealed, internally balanced flap with a tab offers the greatest possibility in reducing hinge-moment. But the final selection of an aerodynamic balance for the variable camber rotor flap arrangements must be a compromise depending on the relative importance of the various factors to be considered.

From the foregoing discussions, it may be concluded by saying, that for the present analysis, a sealed internal balance is recommended.

CHAPTER 5

HOVERING ROTOR PERFORMANCE

The hover performance characteristics of a rotor blade equipped with a trailing-edge flap was obtained by utilizing a prescribed wake hover computer program, call PWAKE (see ref. 60). The PWAKE is based on the application of lifting line theory to the calculation of rotor hover performance, with a prescribed wake representation derived from experimental flow visualization studies of model rotor wakes. The PWAKE program was run first with the flapped rotor blade at values of C_T/σ of .06, .078 and .09, a range which covers most of the hover regime of helicopters, and then again with a rotor with the unflapped airfoil; in this way, a direct evaluation of the effect of flaps are made.

The section aerodynamic characteristics required are the static lift and drag coefficients as a function of angle of attack and Mach number: C_L (α, M) and C_d (α,M).

The program input was arranged such that the model rotor blade was configured as follows: the inboard portion (at .01 of radius) is the VR-7 with 2 degrees flap deflection extending to 90% of radius. From this point to the tip, the unflapped VR-8 section was used. Both the flapped and the unflapped rotor blades had a linear geometeric twist.

Figure 5.1, illustrates the rotor blade section aerodynamic angles relative to each other and to the rotor disk plane. The angle ϕ is the inflow angle of attack and contains the induced vleocity v. The blade

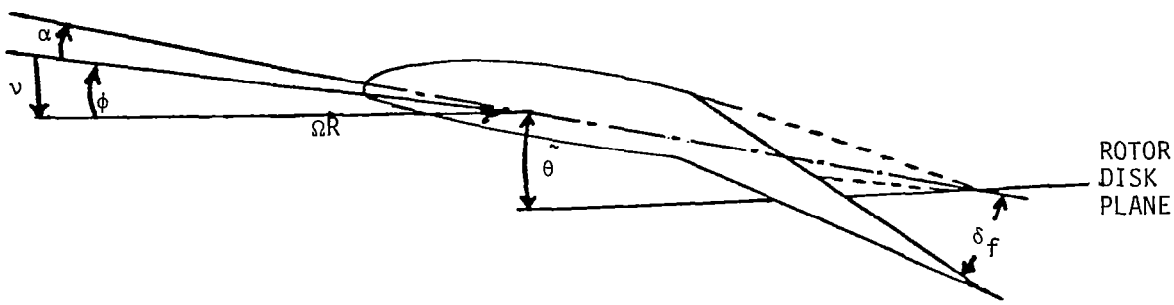

Figure 5.1. - Rotor Blade Section Aerodynamic

pitch angle θ is measured from the chordline of the airfoil section to the plane of the rotor disk. The two-dimensional blade angle of attack, α is therefore seen to be the difference between the blade pitch and inflow angles, while δ_f is the flap deflection.

The principal overall result is shown in Figure 5.2, a plot of power coefficient for various thrust conditions. This plot shows clearly a saving in power consumption for the flapped rotor as compared with the unflapped case. This result is clearly reflected in Figure 5.3, in which the area under each of the curves represents the induced torque for that case; it is apparent that induced torque is lower with

the flap deflected rather than with it retracted. The profile power distribution is displayed in Figure 5.4.

The total power breakdown is as follows for the case of C_T/σ = .078:

	Profile Power(HP)	Induced Power(HP)	Total Power(HP)
Unflapped Rotor	219	893	1112
Flapped Rotor	211	872	1083
ΔHP Due to Flaps	-8	-21	-29

Thus, there is an improvement of 21 hp in induced power and a reduction of 8 hp in profile power, giving a total improvement of 29 hp or 2.6% over the unflapped case.

Figures 5.5 and 5.6 show further details of this effect. In Figure 5.5, it is seen that the flap deflection changes the magnitude of the inflow velocity and redistribute it over the radius. This can be inferred from figure 5.5 by the integral:

$$\int_{.222}^{.735} \nu\, r\, dr/R + \int_{.93}^{.95} \nu\, r\, dr/R \leq \int_{.735}^{.93} \nu\, r\, dr/R + \int_{.95}^{.99} \nu\, r\, dr/R$$

which relate to the power distribution and also by $\int C_l \sin Q\, dr/r$ which relates to the induced power. Also in Figure 5.6 lies the reason why the profile drag near the tip is actually less in the flapped case than in the unflapped case. In the flapped case, the lift coefficient

distribution near the tip is lower than in the unflapped configuration. Since the profile drag increment due to compressibility effects near the tip is a strong function of lift coefficient, the lower tip loading of the flapped rotor leads to a reduction in profile drag in this region relative to the unflapped rotor.

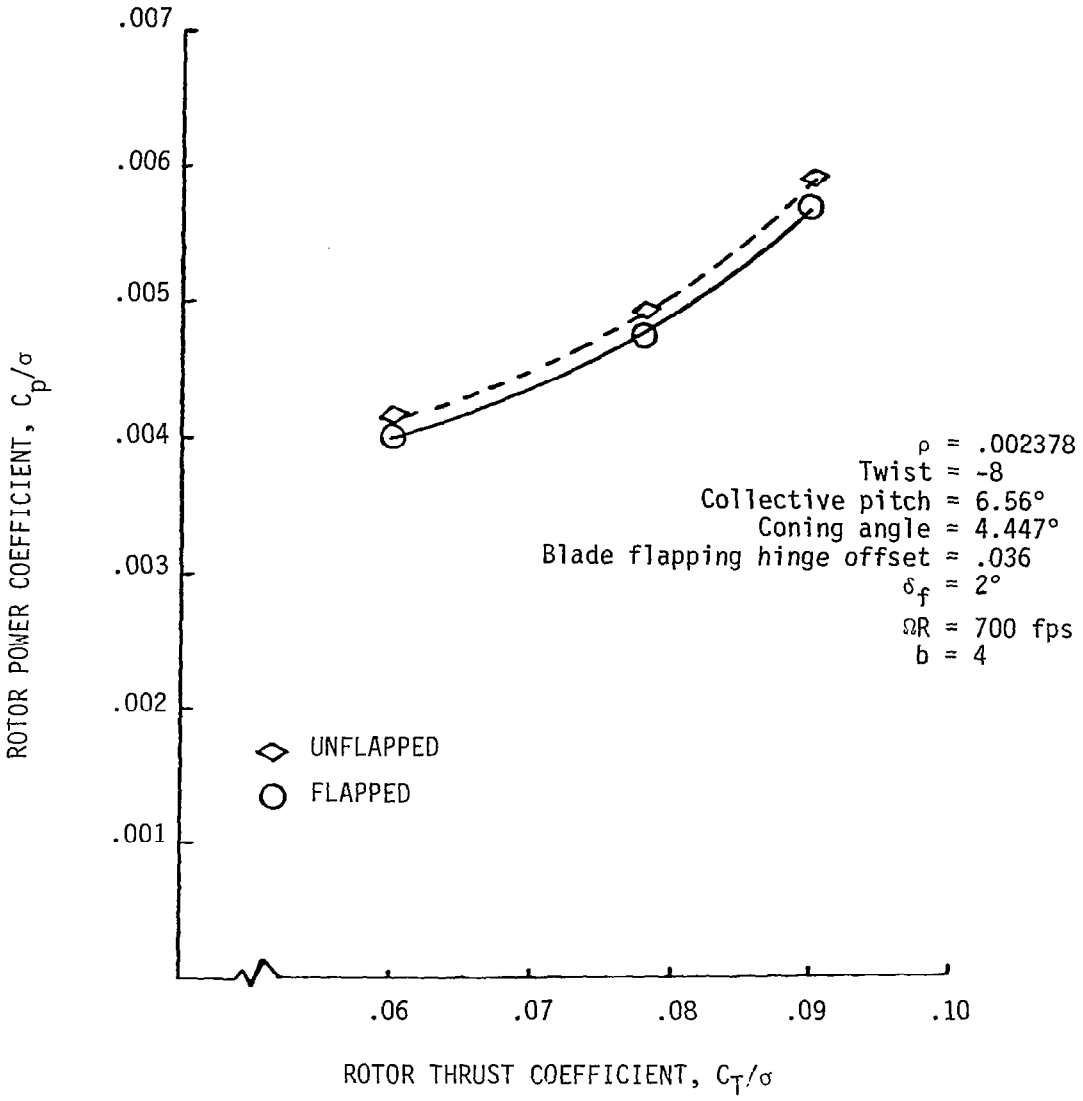

Figure 5.2. - Numerical analysis of rotor power coefficient versus rotor thrust coefficient.

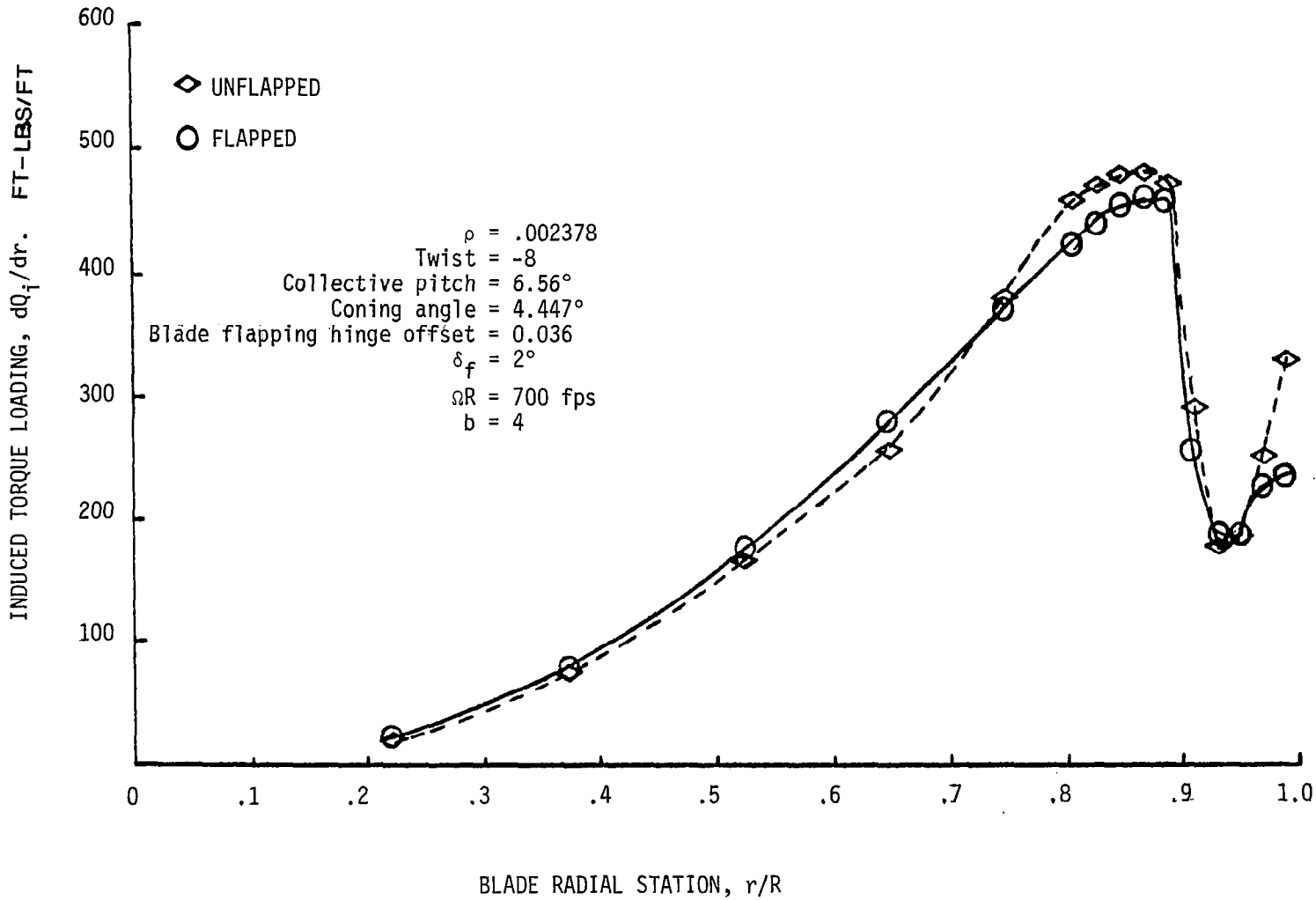

Figure 5.3. - Numerical analysis of induced torque loading versus blade radial station.

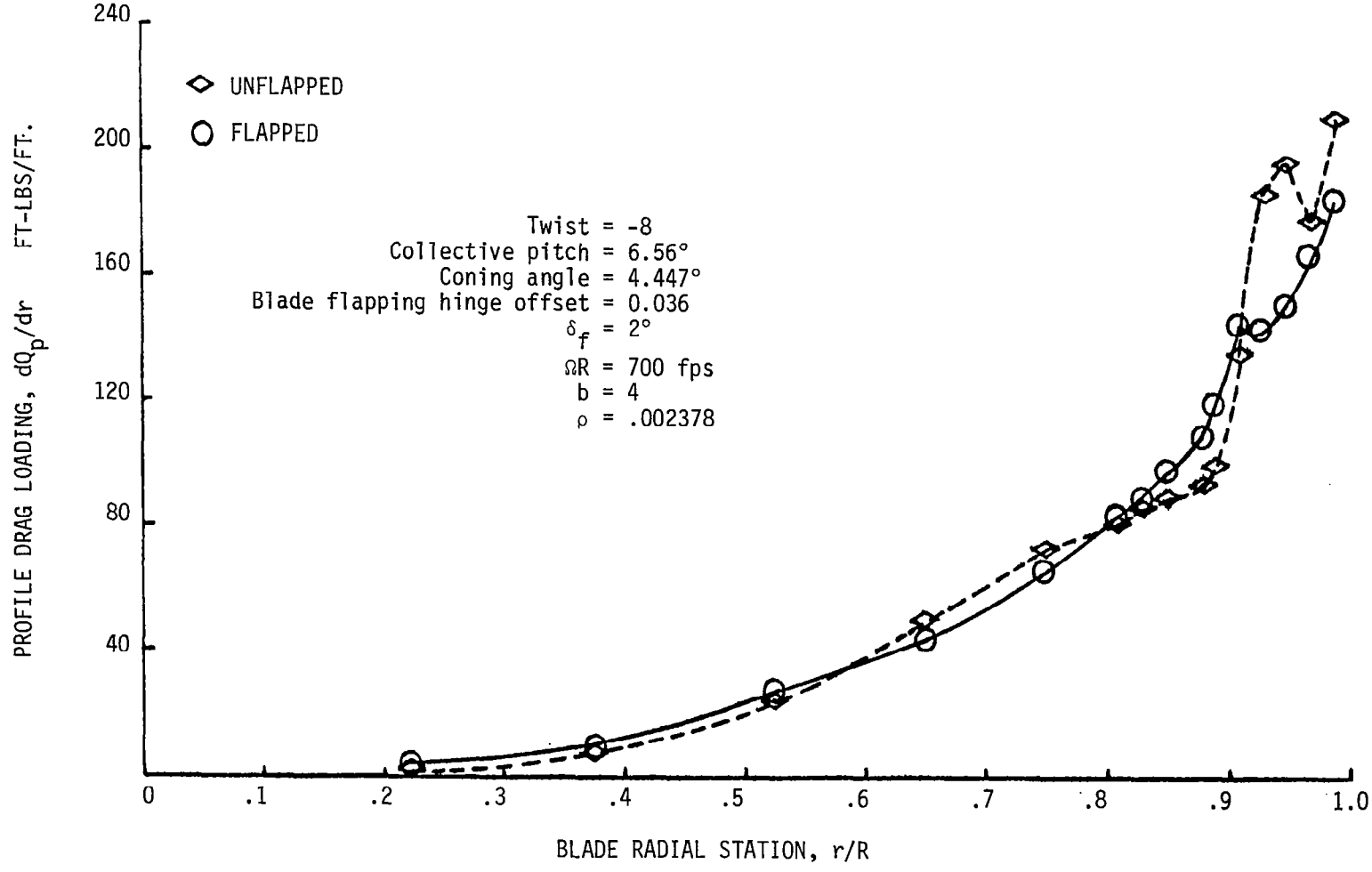

Figure 5.4. - Numerical analysis of profile drag loading vs. blade radial station.

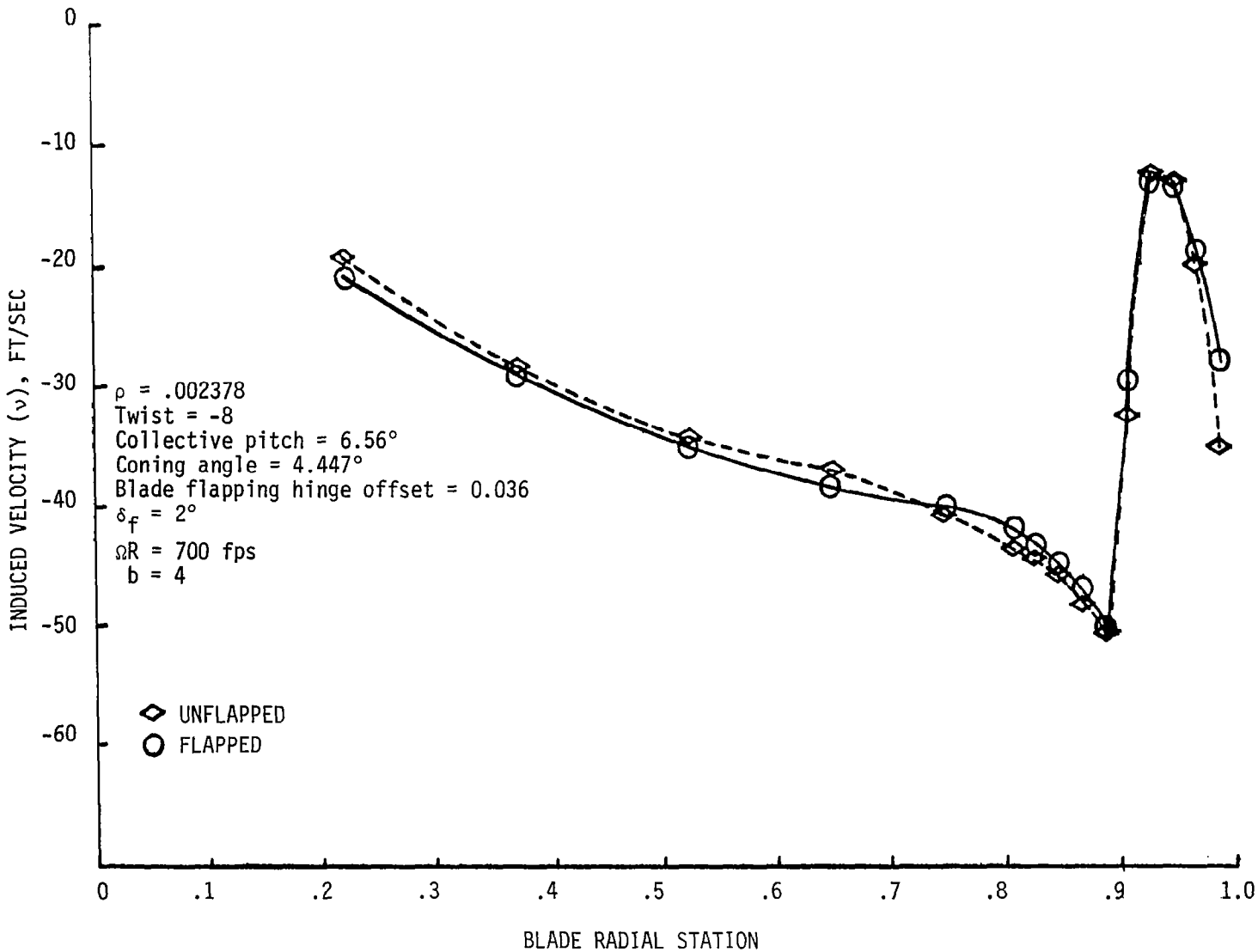

Figure 5.5. - Numerical analysis of the induced velocity versus blade radial station.

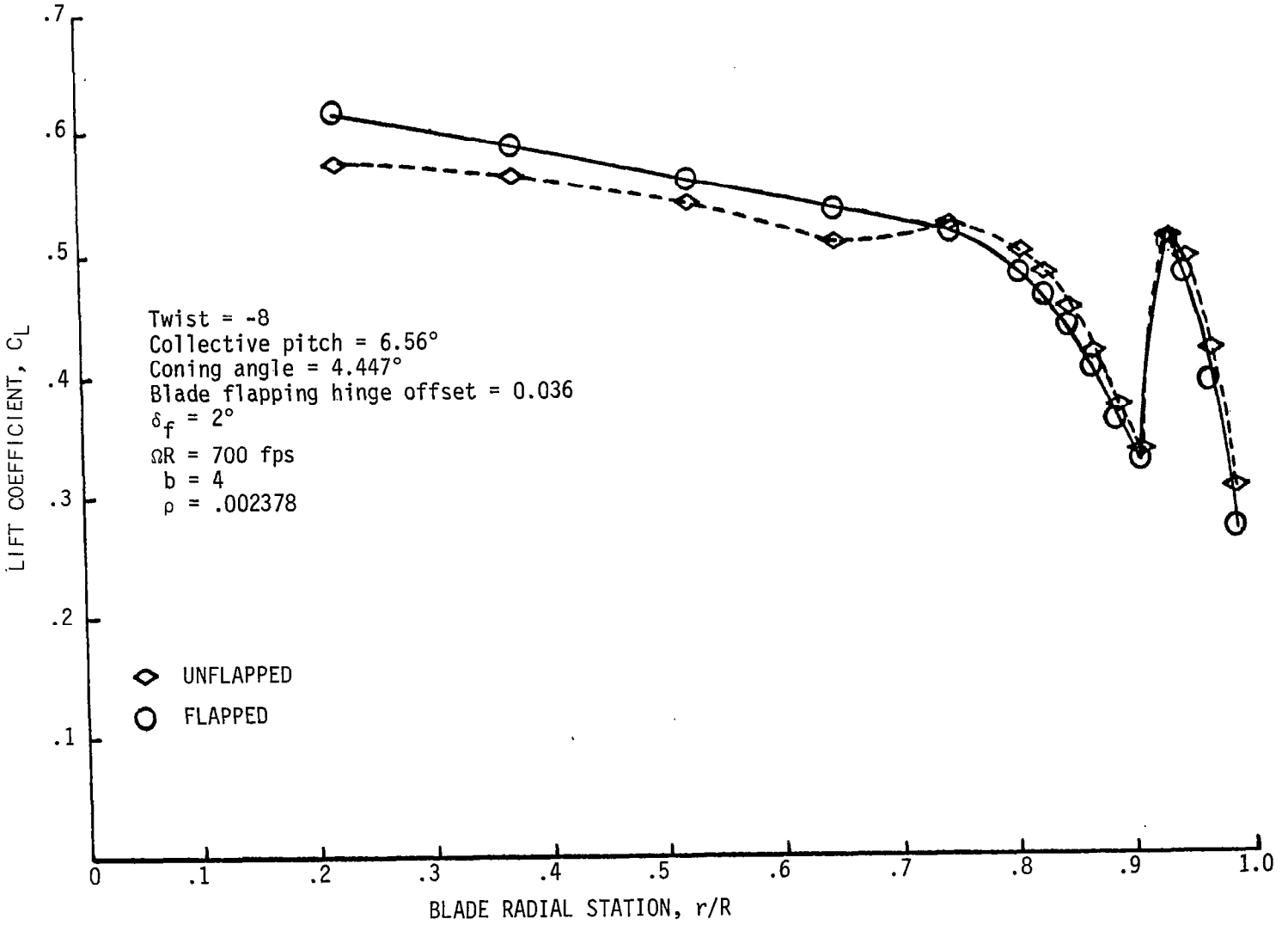

Figure 6.6. - Numerical analysis of the lift coefficient versus blade radial station.

CHAPTER 6

PHYSICAL CONCEPTS OF BLADE MOTION AND ROTOR CONTROL

A knowledge of the Physical Concepts of blade motion and rotor control is useful in gaining a physical understanding of the behavior of the variable camber rotor concept in forward flight, as well as in estimating the maximum flap deflections that would be required, as the rotor blade moves into forward flight, from the hover region with the flap deflected 2 degrees. The equations for computing the lift, propulsive forces and the control setting are available from various theories, however, to reduce computations to a minimum, due to the many variables involved, this analysis presents charts, whereby experimental values can be obtained directly.

Positive directions of forces and moments are shown in the following sketch:

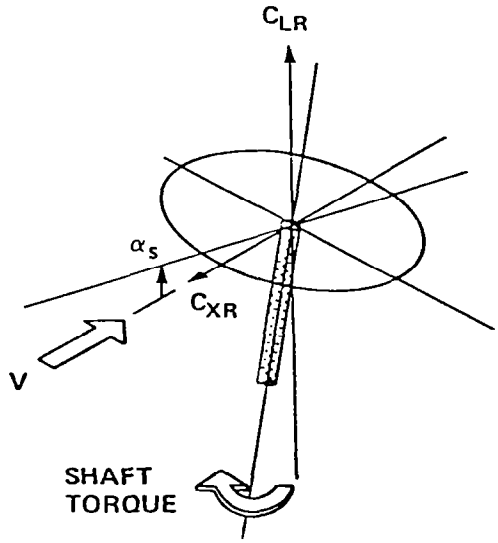

(SOURCE: REF. 61)

ROTOR DESCRIPTION

The experimentally derived charts in the 40- by 80-Foot Wind Tunnel (see ref. 4) for a wide range of lift and propulsive force coefficients, are presented in figures 6.2 to 6.4 for an H-34 helicopter rotor blade (see chapter 2), having a linear twist of -8 degrees, and operating in forward flight at tip-speed ratios ranging from 0.30 to 0.46.

The rotor blade section aerodynamic for the hovering performance was illustrated in chapter 5, by utilizing a sketch with the same

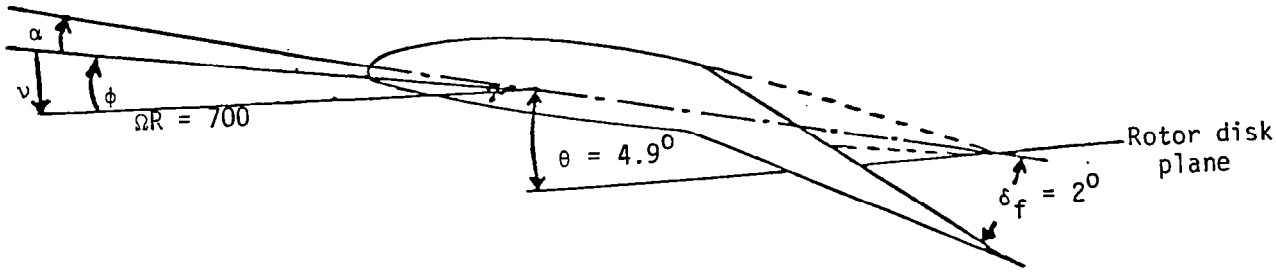

Figure 6.1. - Rotor Blade Section Aerodynamics.

physical characteristics as figure 6.1, and the values taken from PWAKE at 0.75 radius are presented in table 6.1.

Table 6.1-Rotor Blade Section Geometry

Pitch angle, $\theta = \theta_{hover}$	4.9 degs.
Inflow angle, ϕ	4.36 degs.
Effective angle of attack, α	0.538 deg.
Flap deflection, $\delta_f = \delta_{f\ hover}$	2 degs.

Also, it was shown in ref. 62, that the "effective" change in angle of attack for a unit change in flap deflection could be represented by the following parameter:

$$\alpha_\delta = \left.\frac{\partial \alpha}{\partial \delta_f}\right|_{C_L = \text{constant}} \tag{6.1}$$

From PWAKE (chapter 5), the value of α_δ taken at 0.75R was 0.886.

6.1 Computation of Control Setting for Required Lift and Propulsive Force - The steps required for calculating the control axis and propulsive force coefficients were as follows (for a given μ) for the known parameters, L, D or f, ρ, s, and ΩR:

(1) Compute C_{XR}/σ from the relationship

$C_{XR}/\sigma = \text{Drag}/\rho s(\Omega R)^2$ or use $\frac{f}{\overline{bc}R} = 0.09$

(2) Compute C_{LR}/σ from the relationship

$C_{LR}/\sigma = \text{Lift}/\rho s(\Omega R)^2$.

(3) Find α_s from figures 6.2 to 6.4.

(4) Find $\theta_{.75}$ from figures 6.2 to 6.4

(5) Find α_c from figures 6.2 to 6.4 or from $\alpha_c = \alpha_s - B_{1s}$.

(6) Compute B_{1s} from the relationship

$B_{1s} = \alpha_s - \alpha_c$.

(7) Compute Geometric θ for $C_T/\sigma = 0.078$ at forward flight from the relationship

$\theta_{\text{Geometric}} = \theta_{.75} + B_{1s}$ for $\psi = 270°$

The computed values are presented in Table 6.2.

6.2 Calculation of Required Flap Deflections - To estimate the flap deflection that would be required by the helicopter rotor blade flying at a given tip-speed ratio, the procedure was as follows for the known parameters θ_{hover}, α_δ and V.

(1) Compute $\Delta\theta_{flap}$ from the relationship

$$\Delta\theta_{flap} = \theta_{Geometric} - \theta_{hover}. \tag{6.2}$$

(2) Compute δ_f from the relationship

$$\delta_f = \Delta\theta_{flap} / \alpha\delta. \tag{6.3}$$

The computed values are presented in Table 6.3, and also shown in figure 6.5 is a plot of the maximum flap deflection versus the free stream velocity. The results indicated that the flap deflections vary linearly with the free stream velocity, and that the required flap deflection at forward flight for an internally sealed flap in the inboard trailing edge area having an envelope of 0.5c and 0.90R is approximately 9 to 22 degrees for tip speed ratios ranging from 0.30 to 0.46.

TABLE 6.2 - CONTROL AXIS AND PROPULSIVE FORCE COEFFICIENTS

ADVANCE RATIO $\mu = \frac{V}{\Omega R}$	ROTOR-BLADE TIP MACH NUMBER AT 90° AZIMUTH POSITION $M_{(1)(90)}$	ROTOR-BLADE TIP MACH NUMBER AT 270° AZIMUTH POSITION $M_{(1)(270)}$	1 ROTOR-PROPULSIVE FORCE COEFF. $C_X/R/\sigma$	2 ANGLE OF ROTOR SHAFT α_s	3 COLLECTIVE PITCH AT 0.75R $\theta_{.75}$	4 ANGLE OF ATTACK OF CONTROL AXIS (SWASH PLATE) α_c	5 LONGITUDINAL CYCLIC COEFFICIENT B_{1s}	6 GEOMETRIC θ AT C T/σ OF 0.078 AT FORWARD FLIGHT θ GEOMETRIC
0.30	0.74	0.42	.0041	-3.6	7	-10	6.4	13.4
0.40	0.82	0.36	.0072	-6.5	11	-16	9.5	20.5
0.46	0.82	0.324	.0095	-7.5	13.5	-18.5	11	24.5

TABLE 6.3 - REQUIRED FLAP DEFLECTION

V ft/sec	μ	1 $\Delta\theta$ flap	2 δ_f
210	0.30	8.5	9.6
280	0.40	15.6	17.6
322	0.46	19.6	22.12

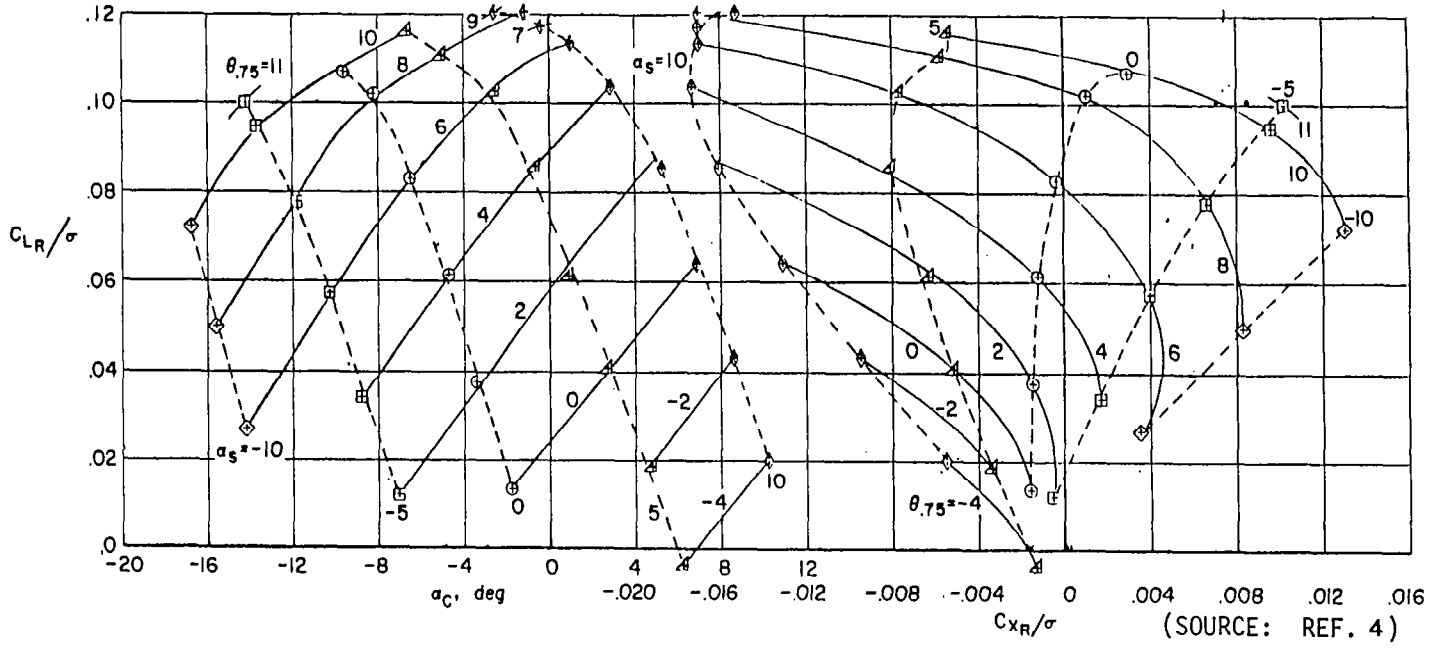

Control axis and propulsive force coefficients.

Figure 6.2. - Articulated rotor with $\theta_1 = -8^0$, $V/\Omega R = 0.30$.

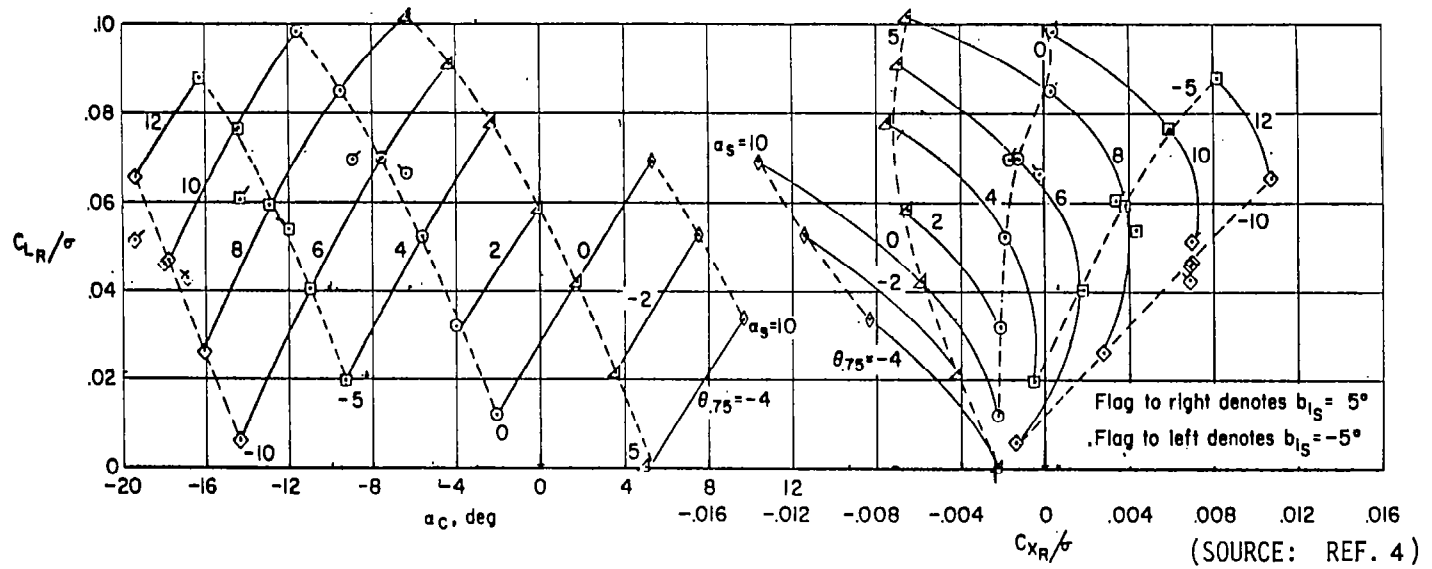

Control axis and propulsive force coefficients.

Figure 6.3. - Articulated rotor with $\theta_1 = -8^0$, $V/_{\Omega R} = 0.40$.

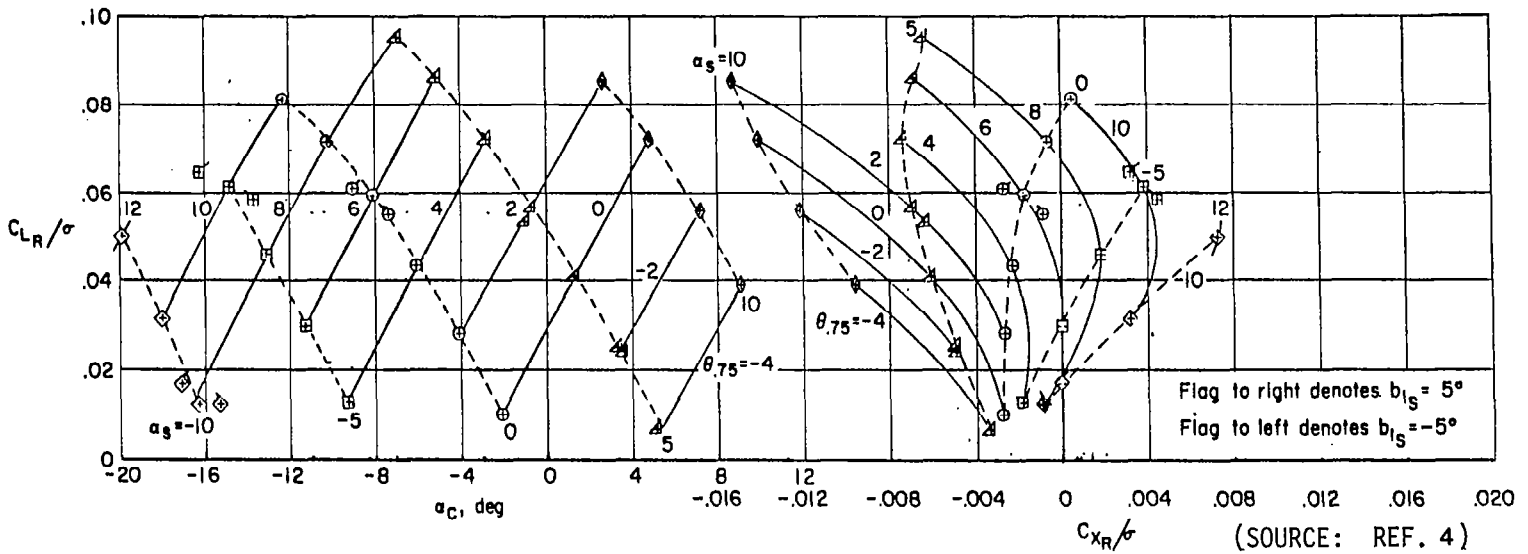

Control axis and propulsive force coefficients.

Figure 6.4. - Articulated rotor with $\theta_1 = -8^\circ$, $V/_{\Omega R} = 0.46$.

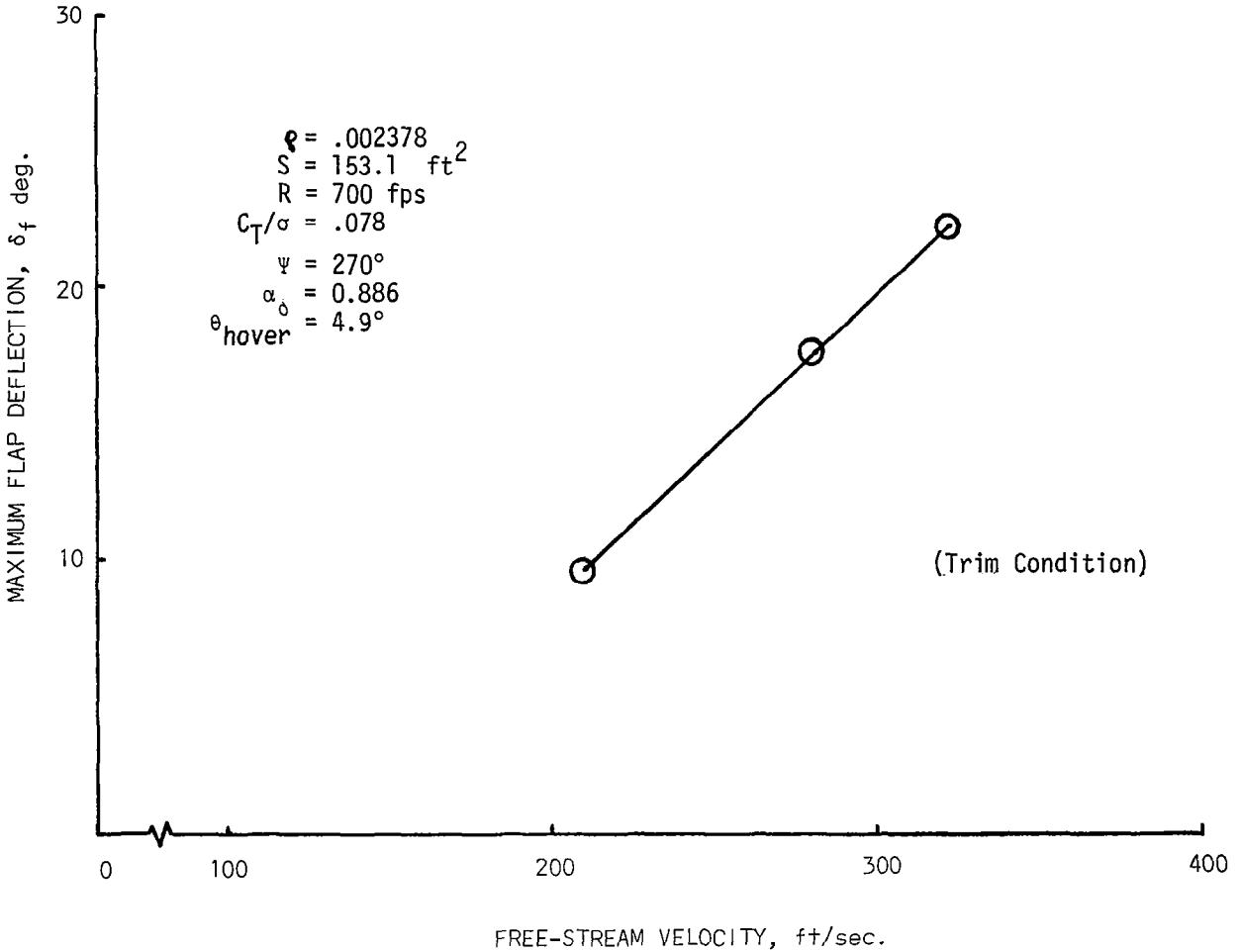

Figure 6.5 - Numerical analysis of flap deflection versus free stream velocity.

CHAPTER 7

ASSESSMENT OF PAYOFF FOR TOTAL CONFIGURATION

The assessment of payoff for the total configuration is important in the evaluation of the variable camber rotor concept. The variable camber rotor has the advantage of providing more meanline curvature where high lift is required and reduced curvature at low lift and transonic condition as required near the advancing blade tip, thus changing the design restrictions of fixed-contour rotor blades.

In evaluating the aerodynamic section, the analysis shows that the variable camber obtained by a large chord flap deflection permitted the attainment of low drags at lift coefficients above the design range of the plain VR-7 airfoil.

In assessing the various aerodynamics techniques to reduce the levels of hinge moments, it was found that all the devices discussed will give lower level hinge moment than that experienced by the plain flaps. Adequate comparisons between the different devices themselves to establish the superiority of one system over another was not made in this analysis, due to the many differences in test conditions within the literature surveyed. The wide variation in the forms of aerodynamic balances employed is indicative of the lack of any completely satisfactory method of balance. The results of the various analyses indicated that for a given lift coefficient, the reduction in flap section hinge-moment coefficient obtainable by the addition of a small aerodynamic overhang balance will change with

the variation of the flap nose shape and the size of the gap at the flap nose. In general, the lift effectiveness of the flap was the same as for a plain flap and was unaffected by the small amount of aerodynamic overhanging balance.

The variable camber rotor has also been shown to be effective in improving hover shaft power by approximately 3%. This improvement was the result of change in the rotor spanwise lift distribution decreasing both profile and induced power of the entire rotor. It was also the result of reduced profile drag near the tip for the flapped rotor as compared to the unflapped configuration. Since the profile drag increment due to compressibility effects near the tip is a strong function of the lift coefficient, the lower tip loading of the flapped rotor leads to a reduction in profile drag in this region relative to the unflapped rotor.

As indicated above, the configuration analyzed herein does achieve the goal of a reduction in both induced and profile power, however, other factors need to be kept in mind which could affect this result. First, the effect of the airfoil pitching moment on blade aerodynamics has not been considered in this model. However, the section pitching moment associated with large chord flap deflection is small as compared with that for an ordinary small-chord deflected to produce the same lift-curve displacement. The pitching moment seem to vary greatly along the radius, as shown in Table 8.1:

TABLE 8.1. - PITCHING MOMENT COEFFICIENT

STATION	LOCAL M	SECTION C_M
.222R	.14	-.0384
.375R	.24	-.040
.75R	.49	-.0427
.95R	.62	-.0476
.99R	.65	-.0521

(All these values are somewhat approximate, but should be accurate ± .005). Thus, pitching moment causing blade torsion should be large but not unmanageably so; as long as these loads are steady (as they would be, in hover) they should present no great problem in control system design.

However, this relatively large blade pitching moment could have an adverse effect on rotor performance because of changes in effective twist due to torsion on the blade. The negative (nose down) moments could well reduce the blade angle-of-attack on blade section such that some or all of the performance gains due to flap deflections are wiped out. More sophisticated models of flapped rotors must be design which take such effects into account.

Also, the structural analysis for the concept was not considered in this analysis, and at first sight, the structural problems associated with the 0.5c flap appear formidable. But with the forward section having structural properties that are stiffer than the aft section in all directions, this should permit the application of the large chord flap without major changes in the structure (also see ref. 63).

In addition, attention must be given to experimenting with various flapped rotor configurations. In all probability large-chord, small deflection configurations will be found to be best, and Air Force sources on maneuvers flaps in fighters should be consulted to verify the performance of such devices in a variety of flight conditions. Special emphasis should be placed on obtaining reliable method for drag prediction for flapped airfoils, since, this is a key area in the profile power-induced power tradeoff and the drag model used herein is sketchy and approximate.

Finally some thought should be given to purely mechanical issues: to achieve a flap deflection along the radius, as is proposed in the present configuration. A number of questions about drag and aeroelasticity effects must be answered before a reliable evaluation of the flapped rotor concept can be made.

CHAPTER 8

CONCLUDING REMARKS AND RECOMMENDATIONS

8.1 Concluding Remarks

8.1.1. Airfoil Section Analysis: - The airfoil section analysis at different Mach numbers and Reynolds numbers on the VR-7 with a 50-percent chord flap deflected 0 to 20 degrees indicated the following conclusions:

1. Considerable reduction of the drag coefficients above the low drag range of the plain airfoil may be effected by use of small deflections of a large-chord flap.

2. The variation of maximum lift, minimum drag, and pitching moment at minimum drag with flap deflection were nearly linear within the range of flap deflections analyzed.

3. Reasonably accurate values of the angle of zero lift and the pitching moment coefficient for airfoils with large-chord flaps may be obtained from the analysis.

8.1.2 Hinge Moment Prediction Techniques: - The hinge- moment characteristics for various arrangements of sealed internal balances were investigated theoretically for the variable camber rotor. The results of the investigation indicated the following conclusions:

1. The flap with a sealed gap gave a smaller minimum profile-drag coefficient than the flap with the unsealed gap.

2. Unsealing the gap at the flap nose appreciably decreased the flap lift effectiveness, and the lift curve for the airfoil was also decreased.

3. Increasing the gap width for a seal of constant width or decreasing the developed seal width tends to result in reduced balance effectiveness.

4. Varying the cross-section of the overhang from that of a thin plate presents no important aerodynamic disadvantage, and if such a change is desired for structural reasons, a considerable range of design is available in which the seal moments are unaltered.

5. Variation of the width of the seal, the sealed gap, or the location of the seal attachment to the forward portion of the rotor blade (wing) structure was shown to affect the seal moments through most of the overhang deflection range.

6. The presence of a small gap at the nose of a plain-overhang balanced flap and of the corresponding unbalanced flap does not appreciably alter the rate of change of hinge moment plotted against control deflection.

7. The tab was effective in producing increments of flap hinge moment at all deflections at which analysis were made and was slightly more effective when the angle of attack and the tab deflection were of the same sign.

8. The characteristics of the tab appear to be independent of flap nose shape and the small amount of flap overhang for the unstalled conditions of the airfoil-flap-tab combinations.

9. The amount of data concerning beveled trailing edges available during the investigation is considered too small to justify any definite conclusions. It is believed, however, that use of the method presented herein will lead to reasonably accurate estimates of the effects of beveled trailing edges on the hinge-moment characteristics of sealed control surfaces. The available data were insufficient, however, to extend the correlation to include unsealed control surfaces.

10. No correlation factor was obtained that would adequately account for all the variables which affect rate of change of hinge moment coefficient with angle of attack or which affect the deflection range over which the balance is effective.

11. For positive and zero angles of attack the gap at the flap nose reduced the balance effectiveness at positive deflections of the flap.

12. The data were too meager to justify any definite generalizations concerning the effects of Mach number on plain-overhang balances except that increases in Mach number consistently decreased the deflection range over which the balance was effective in reducing the slope of the hinge moment curve.

13. The results of the various analyses indicated that for a given lift coefficient, the reduction in flap section hinge-moment coefficient obtainable by the addition of a small aerodynamic overhanging balance will change with the variation of the flap nose shape and the size of the gap at the flap nose. In general, the lift effectiveness of the flap was the same as for a plain flap and was unaffected by the small amount of aerodynamic overhanging balance.

8.1.3 Hovering Rotor Performance: - The analysis for the hovering rotor performance showed the following conclusions:

1. The variable camber rotor has been shown to be effective in reducing power consumption. This improvement was the result of change in rotor spanwise lift distribution which is lower near the tip for the flapped case than the unflapped configuration. Since the profile drag increment due to compressibility is a strong function of lift coefficient, the lower tip loading of the flapped rotor leads to a reduction in profile drag in this region relative to the unflapped rotor.

2. The flap deflection changes the magnitude of the inflow velocity and redistribute it over the radius, which reduce induce power.

8.1.4 Physical Concepts of Blade Motion and Rotor Control: - Charts based on several full-scale wind-tunnel tests were used from which lift, propulsive forces and control setting were computed. The results of the analysis indicated that the maximum flap deflection vary linearly with

the free stream velocity and also, that the required flap deflection at forward flight for a ratio of thrust coefficient to solidity of 0.078 is approximatly 9 to 22 degrees at tip speed ratios ranging from 0.30 to 0.46.

8.2 Recommendations

1. Special emphasis should be placed on obtaining reliable methods of drag prediction for flapped airfoils, since this is a key issue in the profile power induced power tradeoff.
2. A design study should be given to purely mechanical techniques to achieve a flap deflection along the radius.
3. Further analytical studies should be conducted to examine the dynamic and structural characteristics of the variable camber rotor concept, with particular emphasis on the coupling between the flap deflection and the blade bending and flap/lag motion.
4. Make recommendations for experimental research to develop the concept.

REFERENCES

1. Dadone, L.: Rotor Airfoil Optimization - An Understanding of the Physical Limits. In: Proceedings of the 34th Annual Forum of the American Helicopter Society, May 15-17, 1978.

2. Dadone, L. U.: Design and Analytical Study of a Rotor Airfoil. NASA CR 2988, 1978.

3. Awani, A. O.: Doctor of Engineering Project Proposal for the Analysis of a Variable Camber Rotor. University of Kansas, Lawrence, Kansas, KU-CRINC-480-1, Sept. 1980.

4. McCloud III, J. L.; Biggers, J. C.; and Stroub, R. H.: An Investigation of Full-Scale Helicopter Rotors at High Advance Ratios and Advancing Tip Mach Numbers. NASA TN D-4632, July 1968.

5. Awani, A. O.: Analysis of a Variable Camber Device for Helicopter Rotor Systems. Doctoral Dissertation, University of Kansas, Lawrence, Kansas, Aug. 1981.

6. USAF Stability and Control Handbook (DATCOM). Air Force Flight Dynamics Laboratory, Wright-Patterson AFB, Ohio, July 1979.

7. Torenbeek, E.: Synthesis of Subsonic Airplane Design. Delft University Press, 1976.

8. Abbott, Ira H.; and Von Doenhoff, Albert E.: Theory of Wing Sections, Including a Summary of Airfoil Data. McGraw Hill Book Co., 1949.

9. Hoerner, S. F.; and Borst, H. V.: Fluid Dynamic Lift: Practical Information on Aerodynamic and Hydrodynamic Lift, 1975.

10. Cahill, Jones F.: Summary of Section Data on Trailing-Edge High-Lift Devices. NACA RM L8D09, Aug. 1948.

11. Klein, Milton M.: Pressure Distributions and Force Tests of an NACA 65-210 Airfoil Section with a 50-Percent Chord Flap. NACA TN 1167, Jan. 1947.

12. Olson, L. E.; James, W. D.; and McGown, P. R.: Theoretical and Experimental Study of the Drag of Single and Multielement Airfoils. J. Aircraft, Vol. 16, No. 7, July 1979.

13. Bauer, Frances; Garabedian, Paul; Korn, David; and Jameson, Antony: Supercritical Wing Sections II. Lecture Notes in Economics and Mathematical Systems, Vol. 108, Springer-Verlag, 1975.

14. Roshko, Anatol: Pressure Distribution at the Nose of a Thin Lifting Airfoil. Douglas Aircraft Co. Rept. SM-23368, 1958.

15. Allen, H. Julian: General Theory of Airfoil Sections Having Arbitrary Shape or Pressure Distribution. NACA Rept. 833, 1945.

16. Roshko, Anatol: Computation of the Increment of Maximum Lift Due to Flaps. Douglas Aircraft Co. Rept. SM-23626, July 1959.

17. Kuethe, Arnold M.; and Chuen-Yen, Chow: Foundations of Aerodynamics. John Wiley & Sons, 1976.

18. Rettie, I. H.: An Investigation of the Velocity Distribution Around the Nose of the Aerfoil with a Flap. A.R.C. R & M 3027, 1957.

19. Lan, C. E.; and Roskam, Jan: Airplane Aerodynamics and Performance. Roskam Aviation and Engineering Corp., Ottawa, Kansas, 1981.

20. Woods, L. C.: The Theory of Airfoils with Hinged Flaps in Two-Dimensional Compressible Flow. C. P. No. 138, Aug. 1952.

21. Sears, Richard I.: Wind-Tunnel Data on the Aerodynamic Characteristics of Airplane Control Surfaces. NACA A.C.R. 3L08 (WR L-663), Dec. 1943.

22. Purser, Paul E.; and Gillis, Clarence L.: Preliminary Correlation of the Effects of Beveled Trailing Edges on the Hinge-Moment Characteristics of Control Surfaces. NACA CB 3E14, 1943.

23. Jones, Robert T.; and Ames, Milton, B., Jr.: Wind-Tunnel Investigation of Control-Surface Characteristics. V - The Use of a Beveled Trailing-Edge to Reduce the Hinge Moment of a Control Surface. NACA WR L-464, March 1942.

24. Hoggard, H. Page, Jr.: Wind Tunnel Investigation of Control-Surface Characteristics. X - A 30-Percent-Chord Plain Flap with Straight Contour on the NACA 0015 Airfoil. NACA WR L-366, Sept. 1942.

25. Rogallo, Francis M.; and Purser, Paul E.: Wind Tunnel Investigation of a Plain Aileron with Various Training-Edge Modifications on a Tapered Wing. II - Ailerons with Thickened and Beveled Trailing-Edges. NACA WR L-228, Oct. 1942.

26. Purser, P. E.; and McKee, John W.: Wind Tunnel Investigation of a Plain Aileron with Thickened and Beveled Trailing Edges on a Tapered Low-Drag Wing. NACA WR L-526, Jan. 1943.

27. Crandall, Stewart M.; and Murray, H. E.: Analysis of Available Data on the Effects of Tabs on Control-Surface Hinge Moments. NACA TN 1049, May 1946.

28. Rogallo, F. M.: Collection of Balanced-Aileron Test Data. NACA WR L-419, 1944.

29. Sears, Richard I.: Wind-Tunnel Investigation of Control-Surface Characteristics. I - Effect of Gap on the Aerodynamic Characteristics of an NACA 0009 Airfoil with a 30-Percent-Chord Plain Flap. NACA WR L-377, June 1941.

30. Sears, R. I.; and Liddell, Robert B.: Wind-Tunnel Investigation of Control-Surface Characteristics. VI - A 30-Percent-Chord Plain Flap on the NACA 0015 Airfoil. NACA WR L-454, June 1942.

31. Gillis, Clarence L.; and Lockwood, Vernard E.: Wind-Tunnel Investigation of Control-Surface Characteristics. XIII - Various Flap Overhangs Used with a 30-Percent-Chord Flap on an NACA 66-009 Airfoil. NACA WR L-314, 1943.

32. Harris, Thomas A.: Reduction of Hinge Moments of Airplane Control Surfaces by Tabs. NACA Rept. 528, 1935.

33. Rogallo, F. M.; and Lowry, John G.: Wind Tunnel Development of Ailerons for the Curtiss XP-60 Airplane. NACA A.C.R., Sept. 1942.

34. Rogallo, F. M.; and Crandall, Stewart M.: Wind-Tunnel Investigation of Trimming Tabs on a Thickened and Beveled Aileron on a Tapered Low-Drag Wing. NACA A.C.R., March 1943.

35. Sears, R. I.; and Hoggard, H. Page, Jr.: Characteristics of Plain and Balanced Elevators on a Typical Pursuit Fuselage at Attitudes Simulating Normal-Flight and Spin Conditions. NACA WR L-379, March 1942.

36. Garner, I. Elizabeth: Wind-Tunnel Investigation of Control-Surface Characteristics. XX - Plain and Balanced Flaps on an NACA 0009 Rectangular Semispan Tail Surface. NACA ARR L4I11f, 1944.

37. Lowry, John G.; Maloney, James A.; and Garner, I. Elizabeth: Wind-Tunnel Investigation of Shielded Horn Balances and Tabs on a 0.7-Scale Model of XF6F Vertical Tail Surface. NACA WR L-516, 1944.

38. Rogallo, F. M.; and Purser, Paul E.: Wind-Tunnel Investigation of a Plain Aileron with Various Trailing-Edge Modifications on a Tapered Wing. III - Ailerons with Simple and Spring-Linked Balancing Tabs. NACA WR L-470, Jan. 1943.

39. Bryant, L. W.; Burge, C. H.; Sweeting, N. E.; and Greening, J. R.: Experiments on the Balancing of Ailerons by Geared Tabs and Trailing Edge Strips. S. & C. 1195a, British A.R.C., April 5, 1941.

40. Phillips, William H.; and Nissen, James M.: Flight Tests of Various Tail Modifications on the Brewster XSBA-1 Airplane. I - Measurements of Flying Qualities with Original Tail Surfaces. NACA WR L-412, 1943.

41. Swanson, Robert S.; and Crandall, Stewart M.: Analysis of Available Data on the Effectiveness of Ailerons Without Exposed Overhang Balance. NACA A.C.R. L4E01, 1944.

42. Toll, T. A.: Summary of Lateral-Control Research. NACA TN 1245, March 1947.

43. Imlay, Frederick H.; and Bird, J. D.: Wind-Tunnel Tests of Hinge-Moment Characteristics of Spring-Tab Ailerons. NACA ARR 4A26 (WR L-318), Jan. 1944.

44. Toll, Thomas A.: Summary of Lateral-Control Research. NACA Rept. 868.

45. Street, William G.; and Ames, Milton, B., Jr.: Pressure-Distribution Investigation of an NACA 0009 Airfoil with a 50-Percent-Chord Plain Flap and Three Tabs. NACA TN 734, Nov. 1939.

46. Ames, Milton B., Jr.; and Sears, Richard I.: Pressure-Distribution Investigation of an NACA 0009 Airfoil with a 30-Percent-Chord Plain Flap and Three Tabs. NACA TN 759, May 1940.

47. Ames, M. B., Jr.; and Sears, R. I.: Pressure-Distribution Investigation of an NACA 0009 Airfoil with an 80-Percent-Chord Plain Flap and Three Tabs. NACA TN 761, May 1940.

48. Purser, P. E.; and Toll, Thomas A.: Analysis of Available Data on Control Surfaces Having Plain-Overhand and Frise Balances. NACA ACR L4E13 (WR L-665), 1944.

49. Jacobs, Eastman, N.; Ward, Kenneth E.; and Pinkerton, Robert M.: The Characteristics of 78 Related Airfoil Sections from Tests in the Variable-Density Wind Tunnel. NACA Rept. 460, 1933.

50. Purser, P. E.; and Toll, Thomas A.: Wind-Tunnel Investigation of the Characteristics of Blunt-Nose Ailerons on a Tapered Wing. NACA WR L-262, Feb. 1943.

51. Letko, W.; Hollingworth, T. A.; and Anderson, R. A.: Wind-Tunnel Tests of Ailerons at Various Speeds. IV - Ailerons of 0.20 Airfoil Chord and True Contour with 0.35 Aileron-Chord Extreme Blunt-Nose Balance on the NACA 23012 Airfoil. NACA ACR 3H28 (WR L-433), Aug. 1943 and March 1947.

52. Sears, Richard I.; and Gillis, Clarence L.: Wind-Tunnel Investigation of Control Surface Characteristics. VIII - A Large Aerodynamic Balance of Two Nose Shapes Used with a 30-Percent-Chord Flap on a NACA 0015 Airfoil. NACA WR L-378, July 1942.

53. Rogallo, F. M.; and Lowry, J. G.: Resume of Data for Internally Balanced Ailerons. NACA RB 41, March 1943.

54. Murray, Harry E.; and Erwin, Mary A.: Hinge Moments of Sealed-Internal-Balance Arrangements for Control Surfaces. I - Theoretical Investigation. NACA ARR L5F30 (WR L-174), Aug. 1945.

55. Fischel, Jack: Hinge Moments of Sealed-Internal-Balance Arrangements for Control Surfaces. II - Experimental Investigation of Fabric Seals in the Presence of a Thin-Plate Overhang. NACA ARR L5F30a (WR L-52), Aug. 1945.

56. Bates, William R.: Collection and Analysis of Wind-Tunnel Data on the Characteristics of Isolated Tail Surfaces with and without End Plates. NACA TN 1291, May 1947.

57. Swanson, Robert S.; and Priddy, E. Verne: Lifting-Surface-Theory Values of the Damping in Roll and of the Parameters Used in Estimating Aileron Stick Forces. NACA ARR L5F23 (WR L-53), Aug. 1945.

58. Perkins, C. D.; and Hage, R. E.: Airplane Performance Stability and Control. John Wiley & Sons, 1949.

59. Jones, Robert T.; and Ames, Milton B., Jr.: Wind Tunnel Investigation of Control-Surface Characteristics. V - The Use of a Beveled Trailing Edge to Reduce the Hinge Moment of a Control Surface. NACA ARR (WR L-464), March 1942.

60. Landgrebe, Anton J.: An Analytical and Experimental Investigation of Helicopter Rotor Hover Performance and Wake Geometry Characteristics. USAAMRDL TR 71-24, June 1971.

61. Stroub, R. H.: An Investigation of a Full-Scale Rotor with Four Blade Tip Planform Shapes. NASA TM 78580, May 1979.

62. Roskam, Jan: Flight Dynamics of Rigid and Elastic Airplanes, Part I. Roskam Aviation and Engineering Corp., Lawrence, Kansas, 1972.

63. Powlishen, F.: K-16B Rotor Stress Analysis. Kaman Aircraft Corp., Rept. G-113-24, Nov. 18, 1960.

64. Woods, L. C.: The Application of the Polygon Method to the Calculation of the Compressible Subsonic Flow Round Two-Dimensional Profiles. ARC CP 115, 1953.

65. Von Karman, T.: Compressibility Effects in Aerodynamics. Journal of the Aeronautical Sciences, Vol. 8, No. 9, July 1941, pp. 337-356.

66. Woods, L. C.: The Two-Dimensional Subsonic Flow of an Inviscid Fluid About an Aerofoil of Arbitrary Shape. ARC R & M 2811, Nov. 1950.

APPENDIX A

METHOD FOR DETERMINING HINGE MOMENT CHARACTERISTICS

This analysis gives methods for calculating the quantities a_0, a_1, a_2, m_0, h, b_0, b_1, b_2, and b defined in the List of Symbols, in subsonic two-dimensional compressible flow. The theory is applicable to airfoil of moderate thickness (say up to 20% thick) and for small values of flap deflection (δ_f) say $\leq$ 20 degrees.

An exact method for the calculation of a_0, a_1 and h for airfoils of any thickness in incompressible flow is given in (Appendix I, Ref. 20). The exact theory of hinged flat plate in incompressible flow but without restrictions on the value of δ_f is given in (Appendix IV, Ref. 20).

The independent variables of the theory given in Ref. 20 are η and y defined in the List of Symbols, while the dependent variables are γ and θ. The quantity γ can be readily evaluated as a function of q/U. It has been shown (see Ref. 64) that when the approximation

$$M = M_\infty \tag{A.1}$$

is admissible, γ and θ are conjugate harmonic functions in the W plane. Equation (B.1) and an equation similar to $\gamma = \int_{q=u}^{q} 1/2(m + m_\infty) \frac{\rho}{\rho_0}$ $d\left(\log \frac{u}{q}\right) = \gamma\left(\frac{q}{u}\right)$ were first used by Von Ka´rma´n (see Ref. 65) to show that θ and ψ are approximate harmonic functions in the (γ, θ) plane. Although the theory given below is not really valid when M_∞ is greater than the critical value corresponding to the first appearance of sonic speed locally ($m = 1-M^2)^{1/2}$ $\frac{\rho_0}{\rho} = \beta\, \rho_0/\rho$, it can still be applied

with some confidence to calculate the subsonic field when small supersonic patches exist. This point is important in the theory of controls as a high but localized velocity peak does occur at the flap hinge on the upper surface when δ_f is positive.

The complex number defined by

$$f = r + i\theta \tag{A.2}$$

is approximately an analytical function of W(r and θ being conjugate harmonic functions), but if the flow is incompressible, $r = \log (U/q)$, $w = \phi + i\psi$, and so:

$$f = \log \left(\frac{U}{q} e^{i\theta} \right) = \log \left(\frac{Udz}{dw} \right) \tag{A.3}$$

whence, it follows that f is exactly an analytical function of w. Thus the theory of section A.1 (but not of section A.2) will be exact in incompressible flow.

A.1 Basic Mathematical Theory - The theory of this section is quite general and applies to airfoils with and without deflected flaps.

If θ and θ_α are measured from the direction of flow at infinity, ie, if $\theta_\infty = \theta_{\alpha\infty} = 0$, it follows from $r \left(\frac{q}{u} \right)$ and equation (A.2) that

$$f_\infty = f_{\alpha\infty} = 0 \tag{A.4}$$

Now f is an analytical function of $W = -2a \cos\S = -2a \cosh (\eta + i\gamma)$ and there it is an analytical function of §. In fact, as shown in Ref. 66 ,

$$f(\xi) = \frac{-1}{\pi} \int_{y^* = -\pi}^{\pi} \log \sinh 1/2(iy^* - \xi) d\theta(y^*), \tag{A.5}$$

where $\theta(y^*)$ is the value of θ on the airfoil surface. Equation (A.5) is the no-lift solution. If the airfoil is placed at small absolute angle of incidence α , then on the Joukowski Hypothesis, as in Ref. 64,

$$f_\alpha(\xi) = f(\xi) - i\alpha - \log \frac{\text{Sinh } 1/2(\xi + 2ia)}{\sinh 1/2\ \xi} \qquad \text{(A.6)}$$

in which it is assumed that the trailing edge is at $y = \pi$, and the stream direction is from $x = -\infty$ (see fig. A.1). The form of equation (A.6) shows that the effect of incidence on the front stagnation point is to displace it from $y = 0$ to $y = -2\alpha$.

Important auxiliary equations can be deduced by considering the form of f_α takes near infinity. From equations (A.5) and (A.6) it follows

$$f = + \frac{1}{\pi} \int_{y^*=-\pi}^{\pi} (y_2\xi + \log 2)d\theta(y^*) - \frac{1}{2\pi} \int_{y^*=-\pi}^{\pi} y^* d\theta(y^*)$$

$$+ e^{+\xi} \left\{ 2ie^{+i\alpha} \sin\alpha + \frac{1}{\pi} \int_{y^*=-\pi}^{\pi} e^{-iy^*} d\theta(y^*) \right\}$$

$$+ e^{+2\xi} \left\{ ie^{+2i\alpha} \sin 2\alpha + \frac{1}{2\pi} \int_{y^*=-\pi}^{\pi} e^{-2iy^*} d\theta(y^*) \right\} + O(e^{+3\xi})$$

comparing the equation with equation (A.4), it was concluded that

$$\int_{y^*=-\pi}^{\pi} d\theta(y^*) = 0 \qquad \text{(A.7)}$$

and

$$\int_{y^*=-\pi}^{\pi} y^* d\theta(y^*) = - \int_{-\pi}^{\pi} \theta(y^*)dy^* = 0 \qquad \text{(A.8)}$$

Equation (A.7) is the obvious requirement that $\theta(y^*) = \theta(2\pi + y^*)$, while equation (A.8) fixes the orientation of the airfoil for the no-lift

position. If θ is measured from the airfoil chord then $\theta = \underset{\sim}{\theta} + \alpha_0$ and (A.8) yields

$$\alpha_0 = \frac{-1}{2\pi} \int_{-\pi}^{\pi} \underset{\sim}{\theta}(y^*)dy^*, \tag{A.9}$$

which fixes the value of no-lift angle.

From the definition, when $W \to \infty$ implies that $\xi \to -\infty$, and

$$e^{+\xi} = \frac{-a}{w} + 0\left(\frac{a}{w}\right)^3,$$

and so the expansion for f_α can be written

$$f_\alpha = -\frac{a}{w}\left\{ 2^{+i\alpha} \sin\alpha + \frac{1}{\pi} \int_{y^*=-\pi}^{\pi} e^{-iy^*} d\theta(y^*) \right\} \tag{A.10}$$

$$+\left(\frac{a}{w}\right)^2 \left\{ ie^{+2i\alpha} \sin 2\alpha + \frac{1}{2\pi} \int_{y^*=-\pi}^{\pi} e^{-2i\alpha} d\theta(y^*) \right\} + 0\left(\frac{a}{w}\right)^3$$

From this equation it was concluded that

$$\int_{y^*=-\pi}^{\pi} \cos y^* \, d\theta(y^*) = \int_{y^*=-\pi}^{\pi} \sin y^* d\theta(y^*) = 0 \tag{A.11}$$

otherwise when $\alpha = 0$, f will have a term $o\left(\frac{a}{w}\right)$, and since from definition of γ.

$$\frac{q}{u} \doteqdot e^{-\gamma/\beta_\infty} \tag{A.12}$$

q/u will have the form $1 + A/|W|$ for large $|W|$, and a lift producing circulation will exist. (An alternative proof for the case of incompressible flows appears in (Appendix I, Ref. 20).

Finally it follows from $d\phi = qds$, $d\psi = \partial/\partial \underset{o}{qdn}$ and $\phi = -2\alpha \cos \gamma$ that on the airfoil surface

$$\frac{sU}{2\alpha} = \int_{o}^{y} \frac{U \sin\gamma}{q} \, dy \tag{A.13}$$

where the origin of S is taken at the front stagnation point.

A.2 The Airfoil with a Hinged Flap - The theory to be presented below is only valid for small values of flap deflection angle ($\delta_f < 20°$). In general if $\delta_f > 20$ degrees or large, the only recourse is to find the flow about the airfoil and flap ab initio for each value of δ_f. The polygon method (see ref. 64) would be very suitable for such a calculation. However, as shown below, a theory applicable even to comparatively thick airfoils can be developed when terms $o(\delta_f^2)$ can be neglected.

A.2.1 The Velocity Distribution - Subscripts α and δ_f will be used to denote values when the airfoil is at incidence absolute α with a flap deflection(δ_f), while the absence of subscript denote the case $\alpha = \delta_f = 0$. Consider the airfoil, for which $\alpha = \delta_f = 0$, shown in Figure A.2(a). Since solution has been obtained for this case, we can therefore deduce q/u and s/c as functions of y(defined by $\theta = -2a \cos \gamma$) and(Figure A.1). If the polygon method had been used to find the solution, q/u and s/c will be immediately available as functions of y(see example (b), section 5, ref. 20); otherwise suppose q/u is given as a function of S, then the equation

$$\frac{\phi}{2\alpha} = -\cos y = \left(\frac{cU}{2\alpha}\right) \int_{o}^{s/c} q/ud\,(s/c) - 1$$

which follows from $d\phi = qds$, $d\psi = \zeta/\zeta_o qdn$ and $\phi = -2a\cos\gamma$, enables $s/c = s/c(y)$, and hence $q/u = q/u(y)$ to be calculated. The constant $(cU/2a)$ must satisfy

$$1 \doteqdot \left(\frac{cU}{2a}\right) \int_o^{P/c} q/U \, d(s/c)$$

where p is the perimeter distance from the leading to the trailing edge.

In figure A.2 the flap surface is shown starting at c, where $y = \lambda_o$, and F, where $y = -\lambda_1$. When $\delta_f = 0$, each of c and F correspond to a value of x/c of 1-E. The hinge will be taken to be at x/c = 1-E', and of course for thin airfoil $E \doteqdot E'$.

The most important increments (θ_p, say) to θ due to the deflection of the flap are shown in figure A.3. They are due to (i) the front stagnation point shifts to some point A, where $y = \lambda$ say, and consequently the flow direction between A and B is reversed, i.e. θ is decreased by π in $0 < y \leq \lambda$, (ii) the deflection of the flap reduces θ by δ_f in $-\pi \leq y \leq -\lambda_1$, $\lambda_o \leq y \leq \pi$, and (iii) θ is incresed by $\alpha'_o - \alpha_o$ in $-\pi \leq y \leq \pi$ due to a change in the no-lift angle from α_o to α'_o. Unfortunately these are not the only increment to θ, for the modification to the velocity distribution which they produce (see equation A.26 below) slightly distorts the relation between s and λ (equation (A.13)) and consequently causes a slight change ($\Delta\theta$) in $\theta(y)$. Thus θ can be written for $\delta_f \neq 0$ as:

$$\theta_{\delta_f} = \theta_o + \theta_p + \Delta\theta$$

where θ_0 is the value of θ when $\delta_f=0$. For a thin airfoil the distortion in the (s,y) relation will result in quite small values of $\Delta\theta$ away from the nose of the airfoil as $\Delta\theta = \Delta s/R$, where Δs is the change in s. The largest values of $\Delta\theta$ will be near the nose, but these will have a comparatively small effect on the velocity distribution over the flap, and therefore on C_h. Thus only a small error will be introduced (except in the velocity distribution, near the nose) by writing

$$\theta_{\delta_f} = \theta_0 + \theta_p \qquad (A.15)$$

Now θ_0 satisfies equations (A.7), (A.8) and (A.11), and since θ_{δ_f} must also satisfy these equations, this must also be true of θ_p. The increment θ_p is a step function with jumps in value as set out in the following table:-

Y	$-\pi$	λ_1	0	λ	λ_0	π
Jump in θ_p	$-\delta_f + \alpha_o' - \alpha_o$	δ_f	$-\pi$	π	$-\delta_f$	$\delta_f - \alpha_o' + \alpha_o$

and consequently the Stieltjes integrals in equations (A.8) and (A.11) degenerate to

$$2\pi\left(\delta_f - \alpha_o' + \alpha_o'\right) - \delta_f(\lambda_1 + \lambda_0) + \pi\lambda_0 = 0 \qquad (A.16)$$

$$\delta_f(\cos\lambda_0 - \cos\lambda_1) + \pi(1 - \cos\lambda) = 0 \qquad (A.17)$$

$$\delta_f(\sin\lambda_0 + \sin\lambda_1) - \pi\sin\lambda = 0 \qquad (A.18)$$

Equation (A.7) is obviously satisfied by θ_p. Equations (A.17) and (A.18) yield

$$\lambda_o - \lambda_1 = \lambda \tag{A.19}$$

and

$$\sin 1/2\,\lambda = \frac{\delta_f}{\pi} \sin \lambda_m \tag{A.20}$$

where

$$\lambda_m = 1/2(\lambda_o + \lambda_1) \tag{A.21}$$

These equations imply that we cannot fix the postions of c and F (see Fig. A.2) independently. It is convenient to regard δ_f and λ_m as the dependent variables. Equation (A.16) fixes the value of $(\alpha_o' - \alpha_o)$, the change in no-lift angle due to the flap deflection. Using equation (A.20) and ignoring the terms $o(\delta_f^2)$ give

$$\alpha'_o - \alpha_o = \delta_f \left(1 - \frac{\lambda_m}{\pi} + \frac{\sin\lambda_m}{\pi}\right) \tag{A.22}$$

whence

$$\left(\frac{\partial(\alpha'_o - \alpha_o)}{\partial \delta_f}\right)_{\delta_f=0} = 1 - \frac{\lambda_m}{\pi} + \frac{\sin \lambda_m}{\pi} \tag{A.23}$$

In (Appendix III, ref. 15), it is shown that these equations are exact for incompressible flow about a flat hinged plate.

Substitution of equation (A.15) into equation (A.5) yields

$$f_{o,\delta_f}(\xi) = f(\xi) - i(\delta_f - \alpha'_o) + \frac{\delta_f}{\pi} \log \frac{\sinh 1/2\,(\xi - i\lambda_o)}{\sinh 1/2(\xi + i\lambda_1)} + \log \frac{\sinh 1/2\,\xi}{\sinh 1/2(\xi - i\lambda)}.$$

If the airfoil is now placed at an absolute incidence of α the front stagnation point will be displaced from $y = \lambda$ to $y = \lambda - 2\alpha$, and hence (c.f. equation (A.6)) will give

$$f_{\alpha,\delta_f}(\xi) = f(\xi) - o(\delta_f - \alpha' + \alpha_o + \alpha_o) + \frac{\delta_f}{\pi} \log \frac{\sinh 1/2(\xi - i\lambda_o)}{\sinh 1/2(\xi - i\lambda i)}$$

$$+ \log \frac{\sinh 1/2\xi}{\sinh 1/2(\xi + 2i\alpha - i\lambda)} \qquad \text{(A.24)}$$

on the airfoil surface, $\eta=0$, and equation (A.24) becomes with the aid of (A.19) and (A.21)

$$\gamma_{\alpha,\delta_f}(y) = \gamma(y) + \frac{\delta_f}{\pi} \log \frac{\sin 1/2(y - 12\lambda - \lambda_m)}{\sin 1/2(y - 1/2\lambda = \lambda_m)} + \log \frac{\sin 1/2\, y}{\sin 1/2\,(y + 2\alpha - \lambda)} \qquad \text{(A.25)}$$

where λ and λ_m are related by equation (A.20). The velocity distribution now follows from the expression for r defined earlier. At low Mach numbers the approximation (A.12) is valid, when equation (A. 25) yields

$$\frac{q_{\alpha,\delta_f}(y)}{U} = \frac{q}{U} \left\{ \frac{\sin 1/2(y - 1/2\lambda + \lambda_m)}{\sin 1/2(y - 1/2\lambda + \lambda_m)} \right\}^{\delta_f/\pi\beta_\infty} \left\{ \frac{\sin 1/(y + 2\alpha - \lambda)}{\sin 1/2y} \right\}^{1/\beta_\infty} \qquad \text{(A.26)}$$

In the calculations of the various derivatives for C_L, C_m and C_h it would be convenient at first to regard α and δ_f as independent variables. Subsequently α will be replaced by ($\alpha = \alpha' + \alpha_o$ when $\delta_f \neq 0$ and equation (A.22))

$$\alpha = \alpha' + \alpha_o + \delta_f \left(1 - \frac{\lambda m}{\pi} + \frac{\sin \lambda m}{\pi}\right) \qquad \text{(A.27)}$$

so that α' and δ_f become the independent variables.

A.2.2 Calculation of C_1, a_0, a_1, and a_2 - The lift coefficient, C_L, is defined by the contour integral taken round the airfoil surface.

$$C_L = -\frac{1}{c} \oint C_p \cos\theta \, ds ,$$

where the pressure coefficient C_p is a function of y, δ_f and α. Thus since

$$\frac{1}{c} \cos\theta \, ds = \frac{\cos\theta}{cq} \, d\phi = \left(\frac{2a}{Uc}\right)\left(\frac{U \cos\theta}{q}\right) \sin y \, dy,$$

$$C_L = -\left(\frac{2a}{Uc}\right) \int_{-\pi}^{\pi} C_p \sin y \left(\frac{U \cos\theta}{q}\right) dy \qquad (A.28)$$

If ν is the ratio of the specific heats, C_p is given by

$$C_p = \frac{2}{\nu M_\infty^2}\left\{\left[1 - \frac{\nu - 1}{2} M_\infty^2 \left\{\left(\frac{q_{\alpha,\delta_f}}{U}\right)^2 - 1\right\}\right]^{\nu/\nu-1} - 1\right\},$$

from which it folows that

$$\frac{\partial C_p}{\partial (q/U)} = -2\left(\frac{q}{U}\right) \rho/\rho_\infty \qquad (A.29)$$

It is easily deduced from $\gamma(q/U)$, equations (A.20) and (A.25) that

$$\left(\frac{\partial (q/U)}{\partial \alpha}\right)_{\alpha = \delta_f = 0} = \frac{1}{\beta_\infty}\left(\frac{q}{U}\right)\left(\frac{2M_\infty}{M+M_\infty}\right) \frac{\rho_\infty}{\rho} \cot 1/2\, y$$

and

$$\left(\frac{\partial (q/U)}{\partial \delta_f}\right)_{\alpha = \delta_f = 0} + = -\frac{1}{\beta_\infty}\left(\frac{q}{U}\right)\left(\frac{2m}{M+M_\infty}\right) \frac{\rho_\infty}{\rho} \left\{\frac{1}{\pi} \log \frac{\sin 1/2(y-\lambda m)}{\sin 1/2(y+\lambda m)} + \frac{\sin \lambda m}{\pi} \cot 1/2\, y\right\},$$

and hence from equation (A.29)

$$\left(\frac{\partial C_p}{\partial \alpha}\right)_{\alpha=\delta_f=0} = -\frac{2}{\beta_\infty} X \left(\frac{q}{U}\right)^2 \cot 1/2\, y \qquad (A.30)$$

and

$$\left(\frac{\partial C_p}{\partial \delta_f}\right)_{\alpha=\delta_f=0} = \frac{2}{\beta_\infty} X \left(\frac{q}{U}\right)^2 \frac{1}{\pi} \log \frac{\sin 1/2\,(y - \lambda m)}{\sin 1/2\,(y - \lambda m)} + \frac{\sin \lambda m}{\pi} \cot 1/2\, y \qquad (A.31)$$

where $X = \frac{2m_\infty}{M+M_\infty}$

is a function of q/U. This function is given in (Table 2, ref. 64 for M_∞ = 0.5 to 0.79). Differentiating equation (A.28) with respect to α and δ_f and making use of equations (A.30) and (A.31), give

$$\left(\frac{\partial C_l}{\partial \alpha}\right)_{\alpha=\delta_f=0} = \frac{2}{\beta_\infty} \left(\frac{4a}{Uc}\right) \int_{-\pi}^{\pi} X(q/U \cos \theta) \cos^2 1/2\, y\, dy \qquad (A.32)$$

and

$$\left(\frac{\partial C_l}{\partial \delta_f}\right)_{\alpha=\delta_f=0} = -\frac{1}{\beta_\infty} = \left(\frac{4a}{Uc}\right) \int_{-\pi}^{\pi} X(q/U \cos \theta) \sin y \times \left\{ \frac{1}{\pi} \log \frac{\sin 1/2(y - \lambda m)}{\sin 1/2(y - \lambda m)} + \frac{\sin \lambda m}{\pi} \cot 1/2\, y \right\} dy \qquad (A.33)$$

If the polgon method of calculating q/u has been used, (4a/uc), $\frac{q}{u}(y)$ and $\theta(y)$ will be known, $\chi(y)$ can be readily deduced from tables such as those given in ref. 64, and so the integral in (A.32) can be evaluated numerically without difficulty. A calculation of this type appears in ref. 64.

A simple approximation can be found by writing

$$X = q/u \cos \theta = 1 \tag{A.34}$$

in the integrals of equations (A.32) and (A.33). It was found that

$$\left(\frac{\partial C_L}{\partial \alpha}\right)_{\alpha=\delta_f=0} = \frac{2\pi}{\beta_\infty} \quad \frac{4a}{Uc} \tag{A.35}$$

and

$$\left(\frac{\partial C_L}{\partial \delta_f}\right)_{\alpha=\delta_f=0} = 0 \tag{A.36}$$

Equation (A.36) is in any case obvious since C_L depends only on α. From

$$C_L = \alpha \left(\frac{\partial C_L}{\partial \alpha}\right)_{\alpha=\delta_f=0} + \delta_f \left(\frac{\partial C_L}{\partial \delta_f}\right)_{\alpha=\delta_f=0},$$

and equations (A.27), (A.35) and (A.36), it follows that

$$C_L = \frac{2\pi}{\beta_\infty}\left(\frac{4a}{Uc}\right)\left\{ \alpha_o + \alpha' + \delta_f \left(1 - \frac{\lambda m}{\pi} + \frac{\sin \lambda m}{\pi}\right)\right\} .$$

A comparison of this equation with the expression for $C_L = a_o + a_1\alpha' + a_2\delta_f$ yields

$$a_o = \frac{2\pi}{\beta_\infty}\left(\frac{4a}{Uc}\right)\alpha_o \tag{A.37}$$

$$a_1 = \frac{2\pi}{\beta_\infty}\left(\frac{4a}{Uc}\right) \tag{A.38}$$

and

$$a_2/a_1 = 1 - \frac{\lambda m}{\pi} + \frac{\sin \lambda m}{\pi} \tag{A.39}$$

$$C_L = a_o + a_1 \alpha' + a_2 \delta_f$$

It is well known that for thick airfoil in incompressible flow, equations (A.38) and (A.39) are exact (see Appendix I, ref. 20), while in (Appendix IV, ref. 20) it is shown that equation (A.39) is exact for the flat plate in incompressible flow. An approximation for the parameter (4a/UC), which occurs throughout the analysis, is given in (Appendix II, ref. 20).

A.2.3 Calculation of C_m, h and M_0 - The equation corresponding to (A.28) for the moment coefficient about the leading edge is

$$C_m = \left(\frac{2a}{Uc}\right) \int_{-\pi}^{\pi} C_p \left(\frac{x}{c} + \frac{y}{c} \tan \theta \right) \left(\frac{u}{U} \cos \theta \right) \sin y \, dy$$

where x/c is measured from the leading edge. Differentiating this equation with respect to α and δ_f and making use of equations (A.30) and (A.31) give

$$\left(\frac{\partial C_m}{\partial \alpha}\right)_{\alpha=\delta_f=0} = - \frac{2}{\beta_\infty} \left(\frac{4a}{Uc}\right) \int_{-\pi}^{\pi} X \left(\frac{x}{c} + \frac{y}{c} \tan \theta \right) \left(\frac{q}{U} \cos \theta \right) \cos^2 1/2y \, dy,$$

and

$$\left(\frac{\partial C_m}{\partial \delta_f}\right)_{\alpha=\delta_f=0} = \frac{1}{\beta_\infty} \left(\frac{4a}{Uc}\right) \int_{-\pi}^{\pi} X \left(\frac{x}{c} + \frac{y}{c} \tan \theta \right) \left(\frac{q}{U} \cos \theta \right)$$

$$x \left\{ \frac{1}{\pi} \log \frac{\sin 1/2(y - \lambda m)}{\sin 1/2(y + \lambda m)} + \frac{\sin \lambda m}{\pi} \cot 1/2y \right\} \sin y \, dy$$

which can be evaluated directly when q/u has been calculated by the polygon method (see reference 64).

Approximations to these equations can be found by writing Ux = 2a + ϕ, which lead to

$$\frac{x}{c} = 1/2 \left(\frac{4a}{Uc}\right) \quad (1 - \cos y),$$

ignoring the very small "$\frac{y}{c}$ tan θ" term, and using equation (A.34). The results are

$$\left(\frac{\partial C_m}{\partial \alpha}\right)_{\alpha=\delta_f=0} = - \frac{\pi}{2\beta_\infty} \left(\frac{4a}{Uc} \right)^2, \tag{A.40}$$

and

$$\left(\frac{\partial C_m}{\partial \delta_f}\right)_{\alpha=\delta_f=0} = - \frac{1}{2\beta_\infty} \left(\frac{4a}{Uc} \right)^2 \sin\lambda m \ (1 - \cos \lambda m),$$

but $C_l = a_1\alpha$, and so it follows from equations (A.35) (A.40) and the definition of h and m_o that

$$h = 1/4 \ (4a/Uc) \tag{A.41}$$

$$m_o = \frac{1}{2\beta_\infty} \ (4a/Uc)^2 \sin \lambda m(1 - \cos \lambda m).$$

Thus

$$C_m = - hC_L - m_o\delta_f$$

A.2.4 Calculation of C_h, b_o, b_1, and b_2 - By comparing with the equation for C_m given in section A.2.3, it is clear that the coefficient of the hing-moment, C_h is given by

$$C_h = \left(\frac{2a}{Uc}\right) \frac{1}{E^2} \left(\int_{-\pi}^{-\lambda_1} + \int_{\lambda_o}^{\pi} \right) C_p \left\{ \frac{x}{c} - 1 + E' + \frac{y}{c} \tan \theta \right\} \left(\frac{U}{q} \cos \theta \right) \sin y \, dy, \tag{A.42}$$

the hinge being at x/c = 1-E', where $y = \lambda'_m$. From equations (A.19) and (A.21), $\delta_f \to 0$ implies $\lambda_1 \to \lambda_o \to \lambda_m$. Thus

$$(C_h)_{\alpha=\delta_f=0} = 1/2 \left(\frac{4a}{Uc}\right) \frac{1}{E^2} \left(\int_{-\pi}^{-\lambda m} + \int_{\lambda m}^{\pi} \right) C_p \left\{ \frac{x}{c} - 1 + E' + \frac{y}{c} \tan \theta \right\}$$

$$\left(\frac{U}{q} \cos \theta \right) \sin y \tag{A.43}$$

which has to be calculated numerically just as in the exact treatment of equation (A.32)

Differentiating equation (A.41) give, with the aid of equations (A.30) and (A.31),

$$\left.\frac{\partial C_h}{\partial \alpha}\right|_{\alpha=\delta_f=0} = -\frac{2}{\beta_\infty E^2}\left(\frac{4a}{Uc}\right)\left(\int_{-\pi}^{-\lambda m} + \int_{\lambda m}^{\pi}\right) X\left\{\frac{x}{c} - 1 - E' + \frac{y}{c}\tan\theta\right\}$$

$$x\left(\frac{q}{U}\cos\theta\right)\cos^2 1/2\, y\, dy$$

and

$$\left(\frac{\partial C_H}{\partial \delta_f}\right)_{\alpha=\delta_f=0} = -\frac{1}{\beta_\infty E}\,2\left(\frac{4a}{Uc}\right)\left(\int_{-\pi}^{-\lambda m} + \int_{\lambda m}^{\pi}\right) X\left\{\frac{x}{c} - 1 - E' + \frac{y}{c}\tan\theta\right\}$$

$$\left(\frac{q}{U}\cos\theta\right)\sin y \quad x\left\{\frac{\sin\lambda m}{\pi}\cot 1/2\, y + \frac{1}{\pi}\log\frac{\sin 1/2(y - \lambda m)}{\sin 1/2(y + \lambda m)}\right\} dy.$$

The expression $\left(\frac{\partial C_H}{\partial \delta_f}\right)_{\alpha=\delta_f=0}$ neglected a very small term due to the dependence of the limits of the integrals in equation (A.42) on δ_f. Equation (A.44) can be evaluated numerically, but for thin airfoils travelling at speeds such that M_∞ is well below the critical Mach number the following approximation will be sufficiently accurate. It can be shown that

$$X\left\{\frac{x}{c} - 1 - E' + \frac{y}{c}\,\text{tam}\,\theta\right\}\left(\frac{q}{U}\cos\theta\right) = 1/2\left(\frac{4a}{Uc}\right)(\cos\lambda'm - \cos y).$$

which results in

$$\left.\frac{\partial C_H}{\partial \alpha}\right|_{\alpha=\delta_f=0} = -\frac{1}{\beta_\infty E^2}\left(\frac{4a^2}{Uc}\right)x\Big(\sin\lambda m(1 + 1/2\cos\lambda m - \cos\lambda' m)\Big)$$

$$+ (\pi - \lambda m)(\cos\lambda' m - 1/2) \quad ,$$

and

$$\left(\frac{\partial C_H}{\partial \alpha}\right)_{\alpha=\delta_f=0} = -\frac{1}{\beta_\infty E^2}\left(\frac{4a}{Uc}\right)^2 \sin\lambda m \times \{(\pi - \lambda m)(1 - \cos\lambda m) - \sin\lambda m (1 + \cos\lambda m - 2\cos\lambda' m)\}.$$

Now

$$C_h = (C_h)_{\alpha=\delta_f=0} + \alpha\left(\frac{\partial C_h}{\partial \alpha}\right)_{\alpha=\delta_f=0} + \delta_f\left(\frac{\partial C_h}{\partial \delta_f}\right)_{\alpha=\delta_f=0},$$

and using equation (B.27) gives

$$C_h = \left\{(C_h)_{\alpha=\delta_f=0} + \alpha_o\left(\frac{\partial C_h}{\partial \delta}\right)_{\alpha=\delta_f=0}\right\} + \alpha'\left(\frac{\partial C_h}{\partial \delta}\right)_{\alpha=\delta_f=0} + \delta_f\left\{\left(1 - \frac{\lambda m}{\pi} + \frac{\sin\lambda m}{\pi}\right)\left(\frac{\partial C_h}{\partial \alpha}\right)_{\alpha=\delta_f=0}\right\} + \left(\frac{\partial C_H}{\partial \delta_f}\right)_{\alpha=\delta_f=0}.$$

comparing the expression $C_h = b_o + b_1\alpha' + b_2\delta_f$, and using the values of the derivatives found above, it can be concluded that

$$\left.\begin{aligned} b_o = (C_h)_{\alpha=\delta_f=0} &= -\frac{\alpha_o}{\beta_\infty E^2}\left(\frac{4a}{Uc}\right)^2 \sin\lambda m(1 + 1/2\cos\lambda m - \cos\lambda' m) \\ &\quad + (\pi - \lambda_m)(\cos\lambda' m - 1/2) \end{aligned}\right\} \quad (A.45)$$

$$b_1 = -\frac{1}{\beta_\infty E_2}\left(\frac{4a}{Uc}\right)^2 \{\sin\lambda m(1 + 1/2\cos\lambda m - \cos\lambda' m) + (\pi - \lambda m)(\cos\lambda' m - 1/2)\}$$

$$b_2 = -\frac{1}{\pi\beta_\infty E^2}\left(\frac{4a}{Uc}\right)^2 \{(\pi - \lambda m)\sin\lambda m + 1/2\sin^2\lambda m - (1/2 - \cos\lambda' m)(\pi - \lambda m)^2\}$$

while from $C_L = a_1\alpha$ and the definition of b can be shown as follows:

$$b = \frac{1}{2\pi\beta_\infty E^2}\left(\frac{4a}{Uc}\right)^2 \sin\lambda m\{(\pi - \lambda m)(1 - \cos\lambda m) - \sin\lambda m(1 + \cos\lambda m - 2\cos\lambda' m)\} \quad (A.46)$$

FIG. A.1

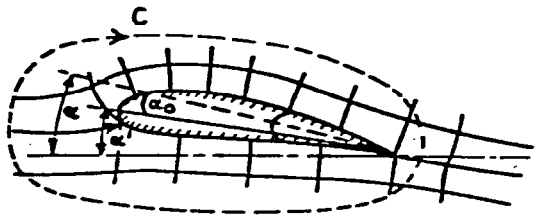

(a) z_α plane

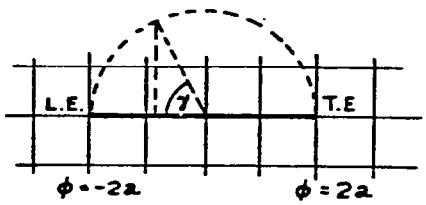

(b) ω plane (zero circulation)

FIG. A.2

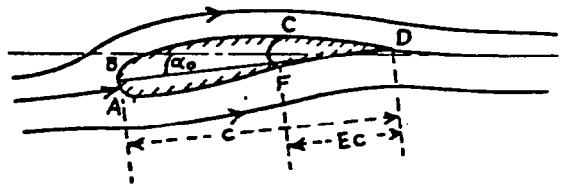

(a) z plane, $\delta_f = 0$

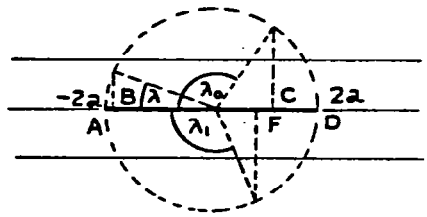

(b) ω plane

(SOURCE: REF. 20)

FIG. A.3

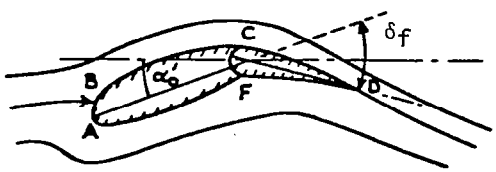

(a) z plane, $\delta_f \neq 0$

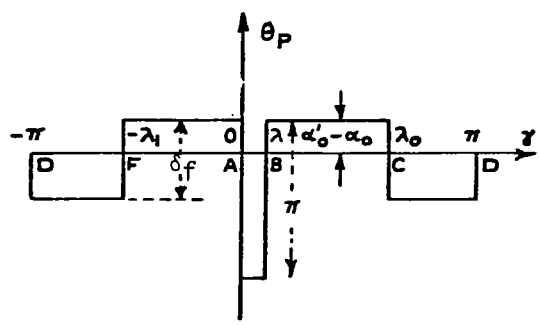

(b) (θ_p, γ)

FIG. A.4

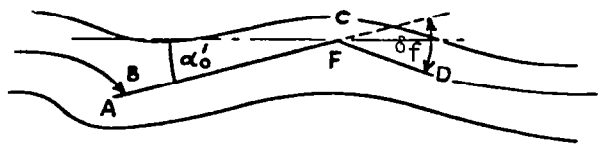

(a) z plane

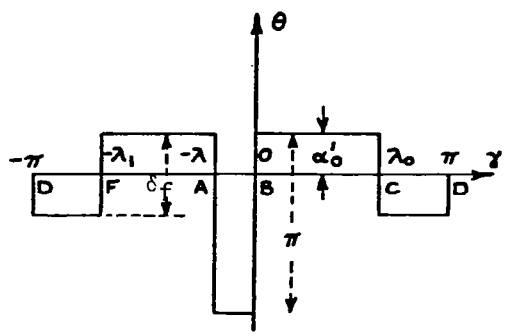

(b) (θ, γ)

Figures 1-4

APPENDIX B

AIRFOIL COORDINATES

AIRFOIL: VR-7 WITH 0° T.E. TAB

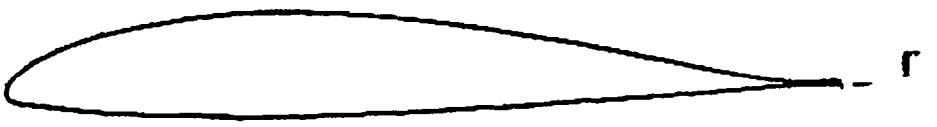

AIRFOIL COORDINATES

x/c	y/c_u	y/c_l
0.	0.	0.
.005	.0165	-.00575
.01	.0218	-.0081
.02	.0298	-.0109
.03	.03625	-.0129
.04	.0415	-.01445
.05	.04605	-.01585
.06	.05025	-.01710
.07	.0541	-.01805
.085	.0593	-.01985
.102	.0645	-.02145
.12	.0691	-.02285
.14	.0737	-.0241
.16	.0775	-.0251
.18	.0808	-.0260
.20	.0838	-.0266
.225	.0867	-.0273
.255	.0892	-.0280
.29	.0909	-.0285
.33	.0914	-.0289
.37	.0905	-.0290
.41	.0887	-.0285
.45	.0856	-.0275
.49	.0816	-.0260
.53	.0767	-.0240
.57	.0710	-.0220
.61	.0646	-.0199
.65	.0580	-.0179
.69	.0514	-.0158
.73	.0447	-.0138
.777	.0374	-.01075
.81	.0301	-.00845
.845	.0235	-.0064
.88	.0167	-.00425
.91	.0105	-.00235
.935	.0062	-.0006
.96	.0050	0.0
1.01	.0050	0.0

CHARACTERISTICS

- Thickness, t/c = 0.12
- Leading Edge Circle
  r/c = .0113

  Center at x/c = .01055
  y/c = .004

- Trailing Edge Tab
  from x/c = .96
  x/c = 1.01
  T.E. Tab Thickness,
  t/c = 0.005

TYPE OF DATA AND METHOD OF TEST

Two-dimensional test in the subsonic insert of the Boeing Supersonic Wind Tunnel in Seattle, Wash.

Lift and pitching moments were measured with a balance.

Drag was determined by a traversing wake probe survey.

Model Chord = 6.38 in
Span = 12 in

SOURCE

Dadone, L., and McMullen, J., "HLH/ATC Rotor System Two-Dimensional Airfoil Test", Boeing Document D301-10071-1, December 1971.

AIRFOIL: VR-8 With 0° T.E. TAB

AIRFOIL COORDINATES

x/c	y/c_{upp}	y/c_{low}
0.	0.	0.
.005	.00850	-.00535
.01	.01175	-.0737
.015	.01425	-.00880
.025	.0183	-.01090
.035	.0217	-.01255
.05	.0261	-.01465
.07	.0309	-.01685
.095	.0357	-.0190
.125	.0402	-.0212
.16	.0444	-.0232
.20	.0480	-.0250
.25	.0510	-.0266
.30	.0530	-.0277
.35	.0535	-.0280
.40	.0525	-.0276
.45	.0502	-.0265
.50	.0467	-.0247
.55	.0426	-.0225
.60	.0380	-.0200
.65	.0333	-.0175
.70	.0285	-.0150
.75	.0237	-.0125
.80	.0190	-.0100
.85	.01428	-.0075
.89	.01048	-.0055
.92	.00761	-.0040
.945	.00524	-.00275
.96	.003404	-.001596
1.01	.003404	-.001596

CHARACTERISTICS

- Thickness, t/x = 0.08
- Leading Edge Circle:

  r/c = 0.00585

  Center at x/c = 0.0058
  y/c = 0.00088
- Trailing Edge Tab:

  from x/c = 0.96
  to x/c = 1.01

  T.E. Tab Thickness, t/c = 0.005

TYPE OF DATA AND METHOD OF TEST

Two-dimensional test in the subsonic insert of the Boeing supersonic wind tunnel in Seattle, Washington.

Lift and Pitching moments were measured with a balance.

Drag was determined by a traversing wake probe survey.

Model Chord = 6.38 in
Span = 12. in

SOURCE

Dadone, L., & McMullen, J., "HLH/ATC Rotor System Two-dimensional Airfoil Test", Boeing Document, D301-10071-1, December, 1971

1. Report No.	2. Government Accession No.	3. Recipient's Catalog No.
NASA CR-3503		

4. Title and Subtitle	5. Report Date
THE INVESTIGATION OF A VARIABLE CAMBER BLADE LIFT CONTROL FOR HELICOPTER ROTOR SYSTEMS	January 1982
	6. Performing Organization Code
7. Author(s)	8. Performing Organization Report No.
Alfred O. Awani	
9. Performing Organization Name and Address	10. Work Unit No.
University of Kansas Center for Research Inc. 2291 Irving Hill Dr. - Campus West Lawrence, KS 66045	532-03-11
	11. Contract or Grant No.
	NCC-292
12. Sponsoring Agency Name and Address	13. Type of Report and Period Covered
National Aeronautics and Space Administration Washington, D.C. 20546	Contractor Report
	14. Sponsoring Agency Code

15. Supplementary Notes

Point of Contact: Robert H. Stroub, Ames Research Center, Mail Stop 247-1, Moffett Field, CA. 94035 415-965-6653, FTS 448-6653

16. Abstract

A new rotor configuration called the variable camber rotor was investigated numerically for its potential to reduce helicopter control loads and improve hover performance. This rotor differs from a conventional rotor in that it incorporates a deflectable 50% chord trailing edge flap to control rotor lift, and a non-feathering (fixed) forward portion. Lift control is achieved by linking the blade flap to a conventional swashplate mechanism; therefore, it is pilot action to the flap deflection that controls rotor lift and tip path plane tilt.

This report presents the aerodynamic characteristics of the flapped and unflapped airfoils, evaluations of aerodynamics techniques to minimize flap hinge moment, comparative hover rotor performance and the physical concepts of the blade motion and rotor control. All the results presented herein are based on numerical analyses.

The assessment of payoff for the total configuration in comparison with a conventional blade, having the same physical characteristics as an H-34 helicopter rotor blade, was examined for hover only. The variable camber rotor configuration is shown to reduce hover power required by at least 2.6% for a flap deflection of 2 degrees. This power improvement was attributed to a change in the spanwise lift distribution decreasing both profile and induced power of the rotor.

17. Key Words (Suggested by Author(s))	18. Distribution Statement
Large trailing edge flaps Variable camber rotor Aerodynamic sections (VR-7, VR-8) Hinge moment balance technique Hovering rotor performance	FEDD Distribution Subject Category 02

19. Security Classif. (of this report)	20. Security Classif. (of this page)	21. No. of Pages	22. Price
Unclassified	Unclassified	130	

Available: NASA's Industrial Applications Centers

NASA-Langley, 1982